Distribution Agreement

In presenting this thesis or dissertation as a partial fulfillment of the requirements for an advanced degree from Emory University, I hereby grant to Emory University and its agents the non-exclusive license to archive, make accessible, and display my thesis or dissertation in whole or in part in all forms of media, now or hereafter known, including display on the world wide web. I understand that I may select some access restrictions as part of the online submission of this thesis or dissertation. I retain all ownership rights to the copyright of the thesis or dissertation. I also retain the right to use in future works (such as articles or books) all or part of this thesis or dissertation.

Signature:

_____ _____

Ziwei Guo Date

Exploring Grain Boundaries and Phase Boundaries Through Monte Carlo Simulation

By

Ziwei Guo
Doctor of Philosophy

Chemistry

_____

James T. Kindt, Ph.D.
Advisor

_____

Joel M. Bowman, Ph.D.
Committee Member

_____

Francesco Evangelista, Ph.D.
Committee Member

Accepted:

_____

Lisa A. Tedesco, Ph.D.
Dean of the James T. Laney School of Graduate Studies

_____

Date

Exploring Grain Boundaries and Phase Boundaries Through Monte Carlo Simulation

By

Ziwei Guo
B.S., Fudan University, 2014

Advisor: James T. Kindt, Ph.D.

An abstract of
A dissertation submitted to the Faculty of the
James T. Laney School of Graduate Studies of Emory University
in partial fulfillment of the requirements for the degree of
Doctor of Philosophy
in Chemistry
2019

Abstract

Exploring Grain Boundaries and Phase Boundaries Through Monte Carlo Simulation

By Ziwei Guo

Monte Carlo simulation methods such as grand canonical Monte Carlo (GCMC) and Gibbs Ensemble Monte Carlo (GEMC) use particle addition, removal, and exchange moves to equilibrate multiphase and/or multicomponent system. This dissertation focuses on the use of a recently developed GCMC variety called Solvent-repacking Monte Carlo (SRMC) and its extensions as applied to the grain boundaries of two-dimensional colloidal solids and the phase coexistences (vapor/liquid and liquid/solid) of size asymmetrical mixtures of Lennard-Jones particles.

Using SRMC to model grain boundaries (GB) of 2-d solids formed from a monolayer of colloids represented as hard spheres, the stiffness of the grain boundary under varying GB angles was determined using the capillary fluctuation method and correlated with the rate of grain coarsening for grains with different misorientations. Further studies, inspired by experiments, show that when surface pressure is increased, the simple dependence of GB shrinking rate on the thermodynamic property of stiffness no longer holds. A complex dependence of GB dynamics on pressure, grain size, and method of preparation of misoriented grains can be traced to the geometries and mobilities of dislocation defects at the GB. Similarly, in hard sphere mixtures with size-asymmetrical impurities, simulated using an extension of SRMC named mixed repacking Monte Carlo (MRMC), affinity of a specific size of impurity for GB of varying misorientation was found to depend on packing details of the GB structure. We also extended our method to the quasi-2D case where spheres are confined to be near a flat surface by gravity, which enables the study of the presence of particles in an overlayer influence the ordering transition and the GB stiffness of the lowest layer. SRMC can also be used to simulate more complex 3D systems including the Lennard-Jones model. Extending the new SRMC approach to the Gibbs ensemble enables us to simulate the liquid-vapor phase coexistence boundaries of certain size-asymmetrical Lennard-Jones mixtures much more efficiently than existing methods. Lastly, we use GCMC and Gibbs-Duhem integration to map the solid-liquid phase coexistence of Lennard-Jones mixtures under conditions where solid-phase vacancies are occupied by multiple smaller impurities.

Exploring Grain Boundaries and Phase Boundaries Through Monte Carlo Simulation

By

Ziwei Guo
B.S., Fudan University, 2014

Advisor: James T. Kindt, Ph.D.

A dissertation submitted to the Faculty of the
James T. Laney School of Graduate Studies of Emory University
in partial fulfillment of the requirements for the degree of
Doctor of Philosophy
in Chemistry
2019

Table of Contents

Acknowledgements

First of all, I would like to express my special thanks to my advisor, Prof. James, T. Kindt, for his patient guidance and continuous supports during my time at graduate school.

I would also like to thank my committee members, Prof. Joel. M. Bowman and Prof. Francesco Evangelista, for their patient guidance and helpful advice.

All past and current members in Kindt group are acknowledged. Especially, I would like to thank Dr. Lewen Yang, Dr. Lara Patel, Keon Reid, Xiaokun Zhang, Dr. Karthik Uppulury, Erdong Lu, Peiyao Wu for their constructive advice and useful discussion.

I would like to express my gratitude to our collaborators in Prof. Eric Weeks group in Department of Physics at Emory University, computational resource support from Emerson Center for Scientific Computation and XSEDE Comet cluster at the San Diego Supercomputer Center, and funding support from Emory University Research Committee and ACS Petroleum Research Fund.

Lastly, I would like to deliver my deepest appreciation to my parents, Li Guo and Chunlan Sun, my wife Mingyi Tan, who always give their support and encouragement.

List of Tables

List of Figures

References to Previously Published Work

1. "Ordering of colloidal hard spheres under gravity: From monolayer to multilayer", Ziwei Guo, Peiyao Wu, and James T. Kindt, *Soft Matter*. **15**, 1027-1037 (2019)

2. "Partitioning of Size-mismatched Impurities to Grain Boundaries in 2-d Solid Hard Sphere Monolayers", Ziwei Guo and J. T. Kindt, *Langmuir*. **34** (43), 12947-12956 (2018)

3. "Simulations of grain boundaries between ordered hard sphere monolayer domains: Orientation-dependent stiffness and its correlation with grain coarsening dynamics", Ziwei Guo and J. T. Kindt*, J. Chem. Phys*. **149**, 044503 (2018)

4. "Size-asymmetrical Lennard-Jones solid solutions: Interstitials and substitutions", Ziwei Guo and J. T. Kindt, *J. Chem. Phys.* **148**, 164504 (2018)

5. "Gibbs Ensemble Monte Carlo with Solvent Repacking: Phase Coexistence of Size-asymmetrical Binary Lennard-Jones Mixtures", Ziwei Guo and J. T. Kindt, *Molecular Simulation*. **44**, 300-308 (2018)

Chapter 1

Introduction

In statistical mechanics, in order to obtain the average of an observable quantity, we can either compute that quantity by time averaging or by ensemble averaging, which is practically conducted by Molecular Dynamics (MD) simulation or Monte Carlo (MC) simulation, respectively.[1] MD simulation is similar to real experiments, where the movement of particles is subject to Newton's equations of motion. Measurements of equilibrium properties are made once the system no longer evolves with time. The involvement of time enables MD to study dynamic properties of the system, like diffusion. In contrast, time does not directly participate in MC simulation. However, for some particular systems or topics of study, MC is preferable since it allows *unphysical* trial moves. These moves may be essential for the equilibration of the system,[1] whether by overcoming energy barriers, establishing a virtual connection to a reservoir of constant chemical potential, or allowing particle exchange between coexisting phases without the need to have an interface present in the simulation box.

We employed several variations of Configurational-Bias Monte Carlo[2] to study the colloidal hard sphere particle, especially the grain boundary properties. We will also demonstrate the generalization of our new MC methods to the 3D soft potential case: size-asymmetrical Lennard-Jones mixtures, to study its phase properties.

1.1 Colloidal particle and Grain boundary

Colloidal particles have been shown to be useful model systems to study many phenomena and understand the underlying physics. The large size (~μm) and slow dynamics (~s) of the colloid, which make the it possible to follow the behavior directly by optical microscopy, facilitate the study by various experiments.[3, 4] In this dissertation, we employed hard sphere model to simulate the colloidal particle, to understand properties of grain boundaries like stiffness and dynamics of grain coarsening.

1.1.1 Phase behavior of hard sphere in 2D

In colloidal solids (ordered assemblies of colloidal particles), colloidal can form grains with different size. Each grain is a region of uniform crystalline order; from grain to grain, the orientation and register of the crystalline lattice will change. It's essential to know the phase behavior of colloidal particle assemblies, to prepare a system in its solid state with grains. In simple cases, colloidal particle can be simulated by hard sphere (HS) model, which is equivalent to hard disk (HD) model if confined in a 2D plane. The phase transition of HD has been studied by canonical simulation.[5, 6] Staring from fluid phase, the HD will form a hexatic phase first as pressure increases, and then finally a long-ranged ordered solid phase. This two-stage ordering has been verified in experiments.[7] The two-phase region between ordered and disordered phase is determined at $0.700<\eta<0.716$, where η is the area fraction of the system. If a size-asymmetrical impurity present, the phase behavior is more complicated. Kindt shows the range of stability of the hexatic phase is suppressed by the impurity, as well as the long range translational order.[8] Russo *et al.* also found the stability window of the hexatic phase is suppressed due to the introduction of small disks.[9]

1.1.2 Grain boundary and Stiffness

Grain boundaries (GBs), the interfaces between neighboring crystal domains that are similar in structure but differ in orientation, are very important in the study of physical properties of polycrystal materials such as metals, ceramics, and semi-conductors[10-12]. Material strength, grain growth, phase transformations, recrystallization and electrical conductivity are highly related to the GB[13-17]. Therefore, controlling the GB plays a vital role in manipulation of the mechanical, optical and electrical properties of polycrystalline materials[18]. One example is the molybdenum disulphide, where van der Zande *et al.* grew highly crystalline islands of monolayer molybdenum disulphide and found that grain boundaries showed distinct, orientation-dependent photoluminescent properties related to the impact of the GB on local composition and bond strain.[19]

A few models have been proposed to describe the GB, including dislocation models, island models, coincidence site models and structural unit model.[20] Each model is based on some assumptions. In this dissertation, we used our new developed Monte Carlo simulation to study the GB in colloidal particle. At a continuum level, the properties of GB can be summarized through two key parameters: the grain-boundary stiffness Γ and the interface mobility M, which govern the structure and dynamics of curvature-driven grain-growth[21]. Stiffness Γ is related to the free energy of GB, as discussed in *Chapter 1*. Various methods have been developed to study the GB stiffness and mobility in experiments[21-24] and simulations[25-28]. Practically, Γ can be quantified through Capillary Fluctuation Method (CFM).[21] The capillary fluctuation method is commonly used to relate the wavelength-dependent fluctuation of the interface to the interfacial free energy or stiffness in a variety of contexts [21, 26, 29, 30]. The spatial fluctuation $\delta h(x)$ is transformed using Eq. (1.1.1) into $\delta h(k)$, which is the intensity of the mode with wave number k in Fourier Spectrum,

where $k = 2\pi m/L$ ($m = 0, \pm1, \pm2, ...$) and L is the length of GB. $\langle|\delta h(k)|^2\rangle$ is calculated as an average over all frames over the simulation trajectory, and is related to the stiffness Γ of the GB by CFM[31] as shown in Eq. (1.1.2):

$$h(k) = \frac{1}{L}\int_0^L \delta h(x)\exp(-ikx)\,dx \tag{1.1.1}$$

$$\log(\langle|\delta h(k)|^2\rangle L) = -2\log(k) + \log(\frac{k_B T}{\Gamma}) \tag{1.1.2}$$

Geometrically, the GB can be characterized by two angles: (i) "misorientation", which is the difference in orientation between the two neighboring crystal grains, and (ii) "inclination", which is the orientation of the GB line.[32] (The inclination is defined as the smaller orientation difference between the GB and the two grain domains it divides.)

1.1.3 Grain boundary segregation

In a polycrystalline alloy, impurities tend to be adsorbed in GB, an effect known as GB segregation,[33-40] for the general reason that GB can provide more free volume than bulk domains. Interactions between impurities and GB can affect the mechanical properties of polycrystalline alloys[41] through impurity drag,[32, 42] or Zener pinning,[32, 43, 44] which also play important roles in grain growth.[45, 46] Understanding of GB segregation is crucial to combating intergranular weakness in the steel industry[35] and improving stability of nanocrystalline alloys.[34, 39] Several techniques like Auger spectroscopy and X-ray absorption can be applied to study GB segregation in experiment.[20] It is discovered that the GB segregation is governed by the interaction forces between the impurity and GB by experiment.[47] Both structure properties (like misorientation) of GB and the property of impurity itself will contribute to interaction forces.

GB segregation in colloidal particle monolayers has been studied by Lavergne *et al.*, where they show the impurity size determines the adaption of either interstitial or substitutional sites, and the

GB segregation can be directly characterized by Langmuir-McLean adsorption model.[40] In our simulation work, we have identified additional factors that affect the GB segregation like the pressure (area fraction) of the system and misorientation.

1.1.4 Dynamics of grain coarsening

Polycrystalline patterns can be widely observed in many systems including crystalline solids,[33] colloidal particles,[48, 49] di-block copolymers[50] and nonequilibrium dissipative structures.[51] The smaller grains are eliminated through coarsening as the system evolves. The grain coarsening has been studied in order to engineer the polycrystalline materials,[52] and to better understand the nonequilibrium ordering phenomenon.[53]

The dynamics of grain coarsening, characterized by the mobility M, can be affected by many factors, like system pressure, misorientation between GBs, and the presence of impurity. In experiment, the dynamics of one special type of boundary, the GB loop, has been studied in several works.[53-56] In the study of GB loop in colloidal particle, Lavergne *et al.* found the formation and kinetics of GB is related to topological constrains in their complex dislocation structure.[54] They also demonstrate the dependence of the mode of deformation (either elastic or plastic) on misorientation angle.

MD simulation has been used in study of GB migration and grain rotation.[55, 56] Z. T. Trautt *et al.* simulated the isolated cylindrical grain in copper, where they found the dynamics of GB motion and grain rotation is affected by initial misorientation angle and temperature. They also employed the dislocation mechanisms to explain the motion of curved GBs.[55] Another MD work by M. Upmanyu *et al.* shows the GB migration and grain rotation can occur simultaneously, where they

observed the grain rotated as a rigid body motion rather than by grain shearing by dislocation passage through the grain interior.[56]

In this dissertation, we used MC to simulate the dynamics of GB. Although Monte Carlo simulation does not produce a trajectory that is directly related to a dynamic algorithm, the evolution of a Monte Carlo trajectory that uses local displacement moves can give qualitative insight into dynamics. This is particularly true for colloidal systems where Brownian dynamics might be a good approximation.[57]

1.2 Lennard-Jones particle

1.2.1 Phase behavior of Lennard-Jones particle

The Lennard-Jones potential is a popular model to represent isotropic or approximately isotropic intermolecular interactions, for instance as seen in the condensed phases of rare gases or methane. Lennard-Jones (LJ) particle interacts with each other via Lennard-Jones potential:

$$\Phi_{ij}(r) = 4\epsilon_{ij}[(\frac{\sigma_{ij}}{r})^{12} - (\frac{\sigma_{ij}}{r})^{6}] \quad (1.2.1)$$

which is a soft potential with an attractive minimum with well depth of ϵ_{ij} and a repulsive core of diameter ~σ_{ij}. For the LJ mixtures, different mixing rules can be used to compute the interaction between different type particles. Phase diagram of one-component LJ system can either be generated by using Gibbs ensemble simulation[58] or Equation of States (EoS).[59] One should notice that the phase diagram of LJ highly depends on the potential truncation method implemented.

Work on generating phase diagrams for mixtures of LJ fluids using various theoretical approaches has spanned several decades.[59-67] Size asymmetrical mixtures are studied by Gibbs Ensemble Monte Carlo (GEMC),[63, 68] Grand Canonical Ensemble Monte Carlo (GCMC) method[69,

[70] or other simulation strategies.[71-74] Complete phase diagrams of binary LJ mixtures were reported by Hall *et al*.[73, 75] through Monte Carlo simulation and the Gibbs–Duhem integration method.[76] The first-order phase transition for binary mixtures has been calculated by the semigrand canonical ensemble method as well.[77] Calculations using the Redlich-Kwong equation of state show the phase diagrams for molecules of unequal sizes are topologically different from similar size molecules.[78] However, most research focuses on the LJ mixtures that have different well depth ϵ but with size ratios σ close to 1. In this dissertation, an efficient method to simulate the LJ mixtures with large size ratio (1.2, 1.5 and 2) will be demonstrated.

1.2.2 Solid Solution

Solid solutions or alloys, mixtures in which one component is distributed in a disordered arrangement throughout an otherwise regular crystal structure, have been widely studied due to their applications in photonics, optics, semiconductors and structure design[79-83]. In a substitutional solid solution (SSS), impurity particles occupy some fraction of lattice sites in place of the majority component particles; the prototypical example is bronze, which contains tin substituted within a copper lattice. In an interstitial solid solution (ISS) the impurity component occupies some fraction of the interstitial positions of the crystalline lattice of the first species; the prototypical example is steel, with carbon atoms occupying interstitial sites in an iron lattice[84]. The presence of the impurities may have important effects on the mechanical behaviors, phase diagrams, and electrical properties of the solids, and the ability to tune the properties by adjusting the amount and nature of the minority components have made solid solutions tremendously important in technology.

Vacancy occupation by one or more impurity particles present interstitially and the equilibrium thermodynamics of vacancy levels has been addressed in the recent metallurgical literature[85], and

appears to have implications for design of advance materials with many thermodynamic and kinetic properties like High Entropy Alloys (HEAs) with much better resistance to radiation damages. To gain some general perspective on whether interstitial and plural substitutional impurities might appear in the same phase we have investigated size-asymmetrical binary LJ solid solutions, with the smaller particle the minority component, at coexistence with the binary liquid mixture.

1.3 The Monte Carlo Method

We will first show the basic concept of the conventional Monte Carlo method including the Metropolis method, then introduce the Configurational-Bias Monte Carlo (CBMC). MC methods in different ensembles will also be discussed. Finally, we will illustrate the general concept of Solvent-Repacking Monte Carlo (SRMC) developed in our lab.

1.3.1 The Metropolis method

MC computes thermal averages by ensemble averaging. The observable quantity A of interest can be measured from the ratio of two integrals:

$$\langle A \rangle = \frac{\int \mathrm{d}\mathbf{p}^{\mathrm{N}}\mathrm{d}\mathbf{r}^{\mathrm{N}}\, A(\mathbf{p}^{\mathrm{N}},\mathbf{r}^{\mathrm{N}}) \exp\left[-\beta\mathcal{H}(\mathbf{p}^{\mathrm{N}},\mathbf{r}^{\mathrm{N}})\right]}{\int \mathrm{d}\mathbf{p}^{\mathrm{N}}\mathrm{d}\mathbf{r}^{\mathrm{N}} \exp\left[-\beta\mathcal{H}(\mathbf{p}^{\mathrm{N}},\mathbf{r}^{\mathrm{N}})\right]} \tag{1.3.1}$$

where $\mathbf{p}^{\mathrm{N}}$ and $\mathbf{r}^{\mathrm{N}}$ is the momenta and coordinate of all N particles, respectively; $\mathcal{H}(\mathbf{p}^{\mathrm{N}}, \mathbf{r}^{\mathrm{N}})$ is the Hamiltonian of the system; and $\beta = 1/k_B T$. If we only are only interested in the static properties, momenta and kinetic energy in (1.3.1) can be factored out of numerator and denominator and cancel out exactly, leaving:

$$\langle A \rangle = \frac{\int \mathrm{d}\mathbf{r}^{\mathrm{N}}\, A(\mathbf{r}^{\mathrm{N}}) \exp\left[-\beta \mathcal{U}(\mathbf{r}^{\mathrm{N}})\right]}{\int \mathrm{d}\mathbf{r}^{\mathrm{N}} \exp\left[-\beta \mathcal{U}(\mathbf{r}^{\mathrm{N}})\right]} \tag{1.3.2}$$

where $\mathcal{U}(\mathbf{r}^{\mathrm{N}})$ is the potential energy of the system. The integral in (1.3.2) cannot be directly evaluated by Monte Carlo importance sampling, but the ratio of integrals is possible to be sampled by Monte Carlo scheme, shown by Metropolis *et al.*[86] One first define the probability density function $\mathcal{N}(\mathbf{r}^{\mathrm{N}})$ denoting the probability of randomly generating points in configuration space:

$$\mathcal{N}(\mathbf{r}^{\mathrm{N}}) \equiv \frac{\exp\left[-\beta \mathcal{U}(\mathbf{r}^{\mathrm{N}})\right]}{Z} \tag{1.3.3}$$

where $Z \equiv \int \mathrm{d}\mathbf{r}^{\mathrm{N}} \exp\left[-\beta \mathcal{U}(\mathbf{r}^{\mathrm{N}})\right]$, the configurational part of the partition function. With this definition, Eq. (1.3.2) can be evaluated as:

$$\langle A \rangle = \int \mathrm{d}\mathbf{r}^{\mathrm{N}}\, A(\mathbf{r}^{\mathrm{N}})\, \mathcal{N}(\mathbf{r}^{\mathrm{N}}) \tag{1.3.4}$$

, which suggests that one can measure *A* by only knowing the relative but not necessarily the absolute probability of visiting different points in configuration space.

The key of MC method is to generate trial moves from old state to new state, sampling the configurational space with a relative probability proportional to the Boltzmann factor. At equilibrium, the number of accepted trial moves from old state to new state should equal to the number of accepted trial move from new state to old state, to maintain a constant distribution. This constraint is described by the detailed balance:

$$\mathcal{N}(\mathrm{o})\pi(\mathrm{o} \to \mathrm{n}) = \mathcal{N}(\mathrm{n})\pi(\mathrm{n} \to \mathrm{o}) \tag{1.3.5}$$

where π is the transition probability between old state (o) and new state (n). In practice, π can be further denoted as the product of the probability (α) of attempting a trial move and the probability (acc) of accepting this trial move. Therefore, the final form of detailed balance can be derived:

$$\mathcal{N}(\mathrm{o})\alpha(\mathrm{o} \to \mathrm{n})\mathrm{acc}(\mathrm{o} \to \mathrm{n}) = \mathcal{N}(\mathrm{n})\alpha(\mathrm{n} \to \mathrm{o})\mathrm{acc}(\mathrm{n} \to \mathrm{o}) \tag{1.3.6}$$

If α is chosen to be symmetrical, as in the original Metropolis scheme, the acceptance probability of accepting a trail move (o → n) is:

$$\mathrm{acc}(\mathrm{o} \to \mathrm{n}) = \min\left[\frac{\exp[-\beta \mathcal{U}(\mathrm{n})]}{\exp[-\beta \mathcal{U}(\mathrm{o})]}, 1\right] \tag{1.3.7}$$

The acc controls the number of accepted trial moves, thus maintaining (or guiding) the system to equilibrium state under pre-determined condition.

1.3.2 Configurational-Bias Monte Carlo

The Configurational-Bias Monte Carlo[2, 87-89] (CBMC) is designed to speed up sampling configuration of chain molecule like polymer[90], through "unphysical" MC trial moves. In contrast to the original Metropolis scheme, where α is chosen to be symmetrical, the $\alpha(\mathrm{o} \to \mathrm{n})$ and $\alpha(\mathrm{n} \to \mathrm{o})$ in CBMC can be different. This asymmetrical transition matrix α can contribute to the speeding up, sometimes by many orders of magnitude.[1] CBMC is implemented by Rosenbluth scheme[91], where the Rosenbluth weight is used to bias the acceptance probability to giving the distribution proportional of Boltzmann weight. In CBMC, the chain molecule is grown stepwise. For each segment, we generate k trial positions randomly and select one with a probability:

$$P_i(\mathrm{n}) = \frac{\exp\left[-\beta u_i(\mathrm{n})\right]}{w_i(n)} \tag{1.3.8}$$

where $u_i(\mathrm{n})$ is the potential energy of the ith segment interacting with other molecules and the previous $i-1$ segments of the molecule under construction; $w_i(\mathrm{n})$ is defined as:

$$w_i(\mathrm{n}) = \sum_{j=1}^{k} \exp\left[-\beta u_i(\mathrm{j})\right] \tag{1.3.9}$$

The Rosenbluth weight can then be calculated as:

$$W(\mathrm{n}) = \prod_{i=1}^{l} w_i(\mathrm{n}) \tag{1.3.10}$$

for a molecule with l segments. Similar scheme is used to regrow the old configuration, with the first trial position ($j = 0$) the same as the position of segment in its old state. The acceptance probability can be then derived as:

$$\mathrm{acc}(\mathrm{o} \to \mathrm{n}) = \min\left[\frac{W(\mathrm{n})}{W(\mathrm{o})}, 1\right] \tag{1.3.11}$$

1.3.3 Monte Carlo Simulation in different ensembles

Monte Carlo simulation can be applied in various ensembles including canonical ensemble, microcanonical ensemble, isobaric-isothermal ensemble, isotension-isothermal ensemble, grand canonical ensemble and Gibbs ensemble.[1] The choice of ensemble depends on the property intended to study. In this dissertation, we mainly conduct our MC simulation in canonical ensemble, grand canonical ensemble and Gibbs ensemble.

In canonical (constant-NVT) ensemble, the probability of finding certain configuration is:

$$\mathcal{N}(\mathbf{r}^{\mathrm{N}}) \propto \exp\left[-\beta \mathcal{U}(\mathbf{r}^{\mathrm{N}})\right] \tag{1.3.12}$$

The acceptance probability of random walk in canonical ensemble is given in Eq. (1.3.7). MC simulation in canonical ensemble is often used to relax the system to equilibrium.

In grand canonical (constant-μVT) ensemble, number of particles in system can change. The system can exchange particles (and energy) with a reservoir at given chemical potential μ. From the partition function in grand canonical ensemble, one can show the probability distribution is:

$$\mathcal{N}(\mathbf{r}^{\mathrm{N}}, \mathrm{N}) \propto \frac{\exp\left(\beta\mu \mathrm{N}\right)\mathbf{V}^{\mathrm{N}}}{\Lambda^{3\mathrm{N}}\mathrm{N!}} \exp\left[-\beta \mathcal{U}(\mathbf{r}^{\mathrm{N}})\right] \tag{1.3.13}$$

where Λ is the thermal de Broglie wavelength ($\Lambda = \sqrt{h^2/2\pi m k_B T}$). In grand canonical Monte Carlo (GCMC) simulation, besides the regular displacement move as shown in canonical ensemble, insertion and removal of particles will also be performed, with the acceptance probability:

$$\mathrm{acc}(\mathrm{N} \to \mathrm{N}+1) = \min\left[\frac{V}{\Lambda^3(\mathrm{N}+1)} \exp[\beta[\mu - \mathcal{U}(\mathrm{N}+1) + \mathcal{U}(\mathrm{N})]], 1\right] \quad (1.3.14)$$

$$\mathrm{acc}(\mathrm{N} \to \mathrm{N}-1) = \min\left[\frac{\Lambda^3 \mathrm{N}}{V} \exp[\beta[\mu + \mathcal{U}(\mathrm{N}-1) - \mathcal{U}(\mathrm{N})]], 1\right] \quad (1.3.15)$$

GCMC simulation can be used to establish phase coexistence if the same chemical potential(s) can produce two distinct system densities or compositions with the same pressure. The Gibbs ensemble method, developed by Panagiotopoulos,[92] is a method that can find the phase coexistence itself in a single simulation. Usually, there are two simulation boxes in Gibbs ensemble, representing the system in different phases. Gibbs ensemble method can establish the equilibrium between these two boxes so that they share the common chemical potential (although we cannot specify the value), pressure and temperature. From the partition function of Gibbs ensemble, the probability distribution of configuration can be derived as:

$$\mathcal{N}\left(\mathrm{n}_1, \mathrm{V}_1, \mathbf{r}_1^{\mathrm{n}_1}, \mathbf{r}_2^{\mathrm{N}-\mathrm{n}_1}\right) \propto \frac{\mathbf{V}_1^{\mathrm{n}_1}(\mathbf{V}-\mathrm{V}_1)^{\mathrm{N}-\mathrm{n}_1}}{\mathrm{n}_1!(\mathrm{N}-\mathrm{n}_1)!} \exp\left[-\beta[\mathcal{U}\left(\mathbf{r}_1^{\mathrm{n}_1}\right) + \mathcal{U}(\mathbf{r}_2^{\mathrm{N}-\mathrm{n}_1})]\right] \quad (1.3.16)$$

where the quantity with subscript denotes its value in the first box or the second box. In Gibbs ensemble MC simulation, there are three types of trial move. The first one is particle displacement, identical to Eq. (1.3.7). The second trial move type is volume change, under the constraint that the total volume of the two boxes is fixed and with the positions of particles within each box scaled uniformly according to the ratio of new and old box dimensions. The acceptance of the volume change can be derived as:

$$\mathrm{acc}(\mathrm{o} \to \mathrm{n}) = \min\left[\left(\frac{\mathrm{V}_1^{\mathrm{n}}}{\mathrm{V}_1^{\mathrm{o}}}\right)^{\mathrm{n}_1+1} \left(\frac{\mathrm{V}-\mathrm{V}_1^{\mathrm{n}}}{\mathrm{V}-\mathrm{V}_1^{\mathrm{o}}}\right)^{\mathrm{N}-\mathrm{n}_1+1} \exp\left[-\beta[\mathcal{U}(\mathbf{r}_{\mathrm{n}}^{\mathrm{N}}) - \mathcal{U}(\mathbf{r}_{\mathrm{o}}^{\mathrm{N}})]\right], 1\right] \quad (1.3.17)$$

The third type of trial move is the particle exchange between the two boxes, under the constraint that the total particle number in the two boxes is fixed. The acceptance of the particle exchange can be derived as:

$$\mathrm{acc}(\mathrm{o} \to \mathrm{n}) = \min\left[\frac{\mathrm{n}_1(\mathrm{V}-\mathrm{V}_1)}{(\mathrm{N}-\mathrm{n}_1+1)\mathrm{V}_1} \exp\left[-\beta[\mathcal{U}(\mathbf{r}_{\mathrm{n}}^{\mathrm{N}}) - \mathcal{U}(\mathbf{r}_{\mathrm{o}}^{\mathrm{N}})]\right], 1\right] \quad (1.3.18)$$

The Gibbs ensemble method has been shown to improve the efficiency of simulating phase equilibria significantly. However, its use is limited if one phase is very dense, since this method rely on the particle exchange to find the coexistence.

1.3.4 Solvent Repacking Monte Carlo

In a very dense system, the acceptance probability (even for CBMC) is usually very low when the space is all occupied by solvent, leaving no room for insertion without removing solvent, or removing solute puts a big empty space in the system which is a high-energy, low probability structure. Some algorithms are developed to tackle on this type problem. One famous method is semi-grand Monte Carlo, where the randomly selected particle can switch its identity to increase (or decrease) the particle size in place. The performance can be improved significantly by using semi-grand MC. However, the size ratio of different species cannot be too large, or the identity swap move will easily fail. In case of simulating highly size-asymmetrical system, a method developed by Ashton *et,al.*[69] can be used, where they can insert a particle with larger size by increasing the size of "ghost" particle gradually. They have shown this method can successfully simulate the LJ binary mixture with size ratio 10:1. But it becomes more expensive with increasing small-particle volume fraction, as it relies for its efficiency on rapid grand-canonical sampling of the small particles, and could face bottlenecks associated with cavity wetting/dewetting transitions of strongly attractive small particles as repulsions from the large particle are gradually turned off or on. A Monte Carlo cluster algorithm is also developed to improve the efficiency for simulating size-asymmetrical system,[93] through restricted GEMC simulation coupled with the highly efficient, rejection-free geometric cluster algorithm (GCA).[94] The effectiveness of the GCA algorithm is limited, however, to a maximum small-particle volume fractions of about 0.34.[95]

A new approach named solvent repacking Monte Carlo (SRMC) is introduced by Kindt,[8] which is a variation of CBMC, offers the possibility of interchanging states with different numbers of solvents in a selected cavity in solvent phases. In general, after removing the solute, trial positions for the first solvent particles are randomly generated and one is accepted with the probability of Boltzmann weights, while the trial positions that overlap with other solvent particles are rejected. After a position is successfully determined, the trial insertion is continued in a similar manner, keep adding the solvent particles until no allowed trial position can be found. SRMC has shown a good capability for repacking the hard disk model,[8] which has the potential to create a new structure while assessing its probability in the ensemble of possible structure. By using the auxiliary potential that can mimic the behavior of the particles inserted later, better configurations are generated as well as the improvement of acceptance probabilities.

Various SRMC methods have been developed to simulate the hard sphere colloids and Lennard-Jones particle. More details of the algorithm will be given in the following chapters. Generally, SRMC can perform well for colloidal HS monolayers, since the HS in 2D is equivalent to HD, and we can still apply the radial distribution function based biased potential (more details about bias potential can be found in the following chapters.). However, when move to soft potential LJ system in 3D, the performance of SRMC is not as good as HD. In some cases it is no better than the semi-grand Monte Carlo method. We also noticed the use of bias potential does not improve the acceptance probability in LJ system. Reasoning for this phenomenon requires further exploration. It could be caused by the nature of the soft potential, and the complexity in the high dimension.

1.4 Outline of Dissertation

SRMC has been shown to simulate the phase transition of dense HD system very efficiently.[8] Here we first extended the original SRMC method to simulate colloidal particle either confined in a 2D plane (with and without size-asymmetric impurities) or in a quasi-2D system where colloidal particle is subjected to gravity. In the simulation of GB properties of colloidal HS in 2D (*Chapter 2*), we used the same SRMC algorithm as in ref [8]. In aim of simulating HS mixtures with size-asymmetrical impurity for studying GB segregation (*Chapter 3*), a new variation of SRMC named mixed repacking Monte Carlo (MRMC) was developed, which facilitates sampling the mixture where impurity is not sparse. *Chapter 4* deals with dynamical aspects of grain coarsening, and uses only local translational moves to mimic the diffusive motion characteristic of colloids in experiments. We also extended our method to quasi-2D case with the presence of gravity, which enables the simulation of sedimentation of colloidal HS multilayer (*Chapter 5*). *Chapter 6* shows our effort on extending the SRMC to more complex soft potential Lennard-Jones model in 3D. The new SRMC algorithm in Gibbs ensemble can simulate the liquid-vapor phase coexistence of size-asymmetrical LJ mixtures more efficiently under certain condition. We also explored the possibility of extending the SRMC to simulate LJ particle in the denser solid phase. However, original GCMC is more efficient to simulate the distribution of impurity in LJ solid with manually created vacancy. We thus showed our findings of LJ solid solutions with vacancy occupied by multiple impurities by using GCMC in *Chapter 7*.

Chapter 2

Simulations of grain boundaries between ordered hard sphere monolayer domains: orientation-dependent stiffness and its correlation with grain coarsening dynamics[1]

The properties of grain boundaries (GBs) between ordered 2-d domains of a hard-sphere monolayer have been investigated using grand canonical Monte Carlo simulations. The capillary fluctuation method was used to determine the GB stiffness over a range of pressures, misorientations and inclinations. Stiffness was found to be sensitive to misorientation (mismatch in the orientation angle of neighboring grains), but not to depend on inclination (angle between the boundary and the grain orientation). Excess area per GB length was observed to follow the same trend as stiffness with respect to grain misorientation and GB inclination angles. Dynamical studies of the evolution of bicrystalline or multicrystalline monolayers with simple geometries show that the calculated angle-dependent stiffnesses correlate well with the rate at which the evolving grain structure decreases the lengths of various GB, in agreement with recent experimental results on monolayers of colloidal microspheres.

2.1 Introduction

Grain boundaries (GBs), the interfaces between neighboring crystal domains that are similar in structure but differ in orientation, are very important in the study of physical properties of

1. Adapted with permission from Guo, Z. and Kindt, J. T., ***J. Chem. Phys.*** 149, 044503 (2018) with the permission of AIP Publishing.

polycrystal materials such as metals, ceramics, semi-conductors[10-12]. Material strength, grain growth, phase transformations, recrystallization and electrical conductivity are highly related to the GB[13-17]. Therefore, controlling the GB plays a vital role in manipulation of the mechanical, optical and electrical properties of polycrystalline materials[18]. GB can be characterized by two key parameters: the grain-boundary stiffness Γ and the interface mobility M, which govern the structure and dynamics of curvature-driven grain-growth[21]. Geometrically, the GB can be characterized by two angles: (i) "misorientation", which is the difference in orientation between the two neighboring crystal grains, and (ii) "inclination", which is the orientation of the GB line.[32] (The inclination is defined as the smaller orientation difference between the GB and the two grain domains it divides.) Various methods have been developed to study the GB stiffness and mobility in experiments[21-24] and simulations[25-28].

Colloidal polycrystalline monolayers have been shown to be useful model systems to study GB and grain growth[96]. Various experiments take advantage of the large size ($\sim\mu m$) and slow dynamics ($\sim s$), which make it possible to follow the behavior directly by optical microscopy[3, 4]. Hexagonal polycrystalline monolayers can be prepared by confining spherical colloidal particles through gravity onto a liquid[97] or solid surface[24] or confined to a gap between surfaces[98]. Under appropriate conditions, the interactions between particles will be dominated by short-ranged repulsions so that the colloids can be modeled as hard spheres.[7] In the limit where fluctuations normal to the plane can be neglected, monodisperse hard spheres become isomorphic to the two-dimensional system of hard disks (HD).[99]

In the present study we will assume that this fully 2-d limit is reached, as is appropriate for sufficiently large and heavy colloidal particles.[7] While we will continue to refer to "spheres" to emphasize the relevance to experimental colloidal systems, we will take also advantage of the

extensive simulation literature on HD phase behavior. It has been shown[5, 6] that the HD phase diagram features a first-order phase coexistence between a fluid phase at area fraction $\eta = 0.700$ and hexatic phase at $\eta = 0.716$. The hexatic phase is stable over a narrow range of area fractions, and undergoes a continuous transition to a 2-d solid phase upon further compression to $\eta \approx 0.720$.[6] The grains modeled here fall in the range of area fractions from $\eta = 0.727$ to 0.782 and so can be considered 2-d solids.

Although stiffness of GB in colloidal monolayers has been addressed through several experiments,[21, 24, 98] no systematic study has been done to show the dependence of stiffness on misorientation, inclination and pressure. By engineering the grain domains in our simulations, we are able to study the GB systematically with controllable parameters. In this study, stiffness dependence on these variables will be reported for monolayers of uniform hard sphere, and compared with experimental observations[21, 24]. Simulations are performed in the grand canonical ensemble, implemented here using the solvent-repacking Monte Carlo (SRMC)[8] algorithm to aid in particle exchange in the dense system. Setting a common chemical potential facilitates comparison across systems under varying geometries at the same pressure. Local particle insertion and removal moves, distributed across many processors in parallel through domain decomposition, allow the local density at the boundary and within the grains to reach equilibrium and undergo fluctuations independently, rather than relying on uniform expansion and compression of the whole system to achieve constant pressure. Fluctuations of the GB shape are interpreted via the capillary fluctuation method (CFM)[31] to yield the stiffness.

This chapter will first report calculations of the stiffness of boundaries between adjacent domains of hard spheres in the 2-d solid phase, with attention to effects of pressure, grain misorientation, and GB inclination. In the second section of this chapter, the pre-melting behaviors

of GB at pressures approaching the melting transition, and a non-equilibrium faceting behavior observed at high pressures, will be discussed qualitatively. Finally, dynamic Monte Carlo studies of simple 2- and 4-grain systems are used to show how the evolution of grain sizes and shapes are influenced by grain misorientation in manner that is qualitatively consistent with the trends in GB stiffness.

2.2 Methods

2.2.1 System Construction and initialization

In the study of stiffness, ordered grains of spheres are set up in a pair of parallel stripes making two parallel GBs align with the x direction. Initial ordered structures were taken from equilibrated 2-d ordered phases generated in previous studies[8]. For simulations at the highest chemical potential/pressure conditions, the starting structure was a perfect hexagonal lattice with density close to the expected equilibrium density. The use of parallel stripe grains with boundaries that are continuous via periodic boundaries provide a well-defined misorientation between the grains, a fixed mean inclination between the boundary and the grains, and a fixed GB length. The two domains have the same area in the initial configuration, and are separated by a distance of σ in the y direction to remove particle overlaps. This gap between the grains is filled quickly by the SRMC algorithm.

In the dynamic study, the two (or four) domains with different orientations are engineered to the desired domain shapes. A distance of σ between domains is applied for the same reason to prevent overlapping. The output configuration after 1000 MC cycles in grand canonical ensemble is used as the initial configuration for the dynamic study in NVT ensemble, in which the gaps are already filled while the areas of domains do not change significantly.

2.2.2 Solvent-Repacking Monte Carlo

To sample over the grand canonical ensemble at some particle fugacity $f = \exp(\beta\mu)$ at high packing density, the solvent-repacking Monte Carlo (SRMC) algorithm was used and is described here briefly. The SRMC method uses configurational bias Monte Carlo[2] (CBMC) strategy to generate a set of positions for a set of particles to replace the particles present in a circular cavity randomly selected within the simulation box. After defining the cavity and selecting its radius (as a random value between 1 and 1.4 σ in the present case), a number k of insertion moves will be performed to randomly and uniformly sample the cavity region in each cycle i. The j'th particle will then be selected with a probability:

$$P_{i,j'} = \frac{\exp\left(-\beta u'_{i,j'}\right)}{\sum_{j=1}^{k} \exp\left(-\beta u'_{i,j'}\right)} = \frac{\exp\left(-\beta u'_{i,j'}\right)}{W'_i} \tag{2.2.1}$$

where $u'_{i,j'}$ is the auxiliary potential (the logarithm of the radial distribution function (RDF) for hard spheres with an area fraction 0.69 is used in this work; this and choices for k were consistent with previous work[8]) for the interaction of the j'th particle with particles inserted in previous cycle and the solvent shell around the cavity. The insertion cycle will be repeated until some predetermined conditions are met: either particle number in cavity reach a maximum (20 in this work) or none of the k trial positions are successful. We thus can get a maximum number of particles n_{max} that can be inserted in this cavity region (which is independent of the current number.)

The probability for selecting a configuration with number of particles i' is:

$$P(i') = \frac{\omega_{i'}}{\sum_{i=0}^{n_{max}} \omega_i} \tag{2.2.2}$$

where the weight $\omega_{i'}$ associating the configurations with different numbers of particles can be calculated as:

$$\omega_i = \frac{f^i}{\Lambda^{di}} \frac{{v_{cav}}^i}{i! \prod_{i'=1}^{i} k_{i'}} W_i' \frac{\exp(-\beta U_i)}{\exp(-\beta U_i')} \tag{2.2.3}$$

where Λ is the de Broglie thermal wavelength (set to 1 in all simulations); d is the dimension of the system; U_i and U_i' are the true potential energy (always equal to zero) and the auxiliary bias potential energy, respectively. Calculation of weights associated with the current configuration of particles involves the generating of alternative "dummy" trial positions, as is standard in CBMC. The overall acceptance probability for transition from current state with n_{cav} particles in cavity to the new state with $n_{cav'}$ particles can be written as:

$$acc_{n_{cav} \to n_{cav'}} = min\left[1, \frac{\sum_{i=0}^{n_{max,new}} \omega_{i,new}}{\sum_{i=0}^{n_{max,current}} \omega_{i,current}}\right] \tag{2.2.4}$$

2.2.3 Order parameter and GB detection

Bond-orientational order parameter[100] Ψ_6 is used to characterize the local crystalline order of particle j:

$$\Psi_6(\vec{r_j}) = \frac{1}{N_j} \sum_{k=1}^{N_j} e^{i6\Delta\theta_{jk}} \tag{2.2.5}$$

where $\Delta\theta_{jk}$ is defined as the angle between the x direction with the vector connecting the central particle j and one of its N_j nearest neighbor k within a cutoff 1.5σ. The orientation of the hexagon formed by six neighbors of particle j can then be calculated by $\theta_6 = \arg(\Psi_6)/6$, which is a value varied from 0 to 60° due to the symmetry of hexagon. The orientation of the grain domain can be quantified by averaging all the θ_6 of particles belonging to the domain. In the rest of this report, θ_6 refers to the orientation of the domain instead of single particle for simplicity.

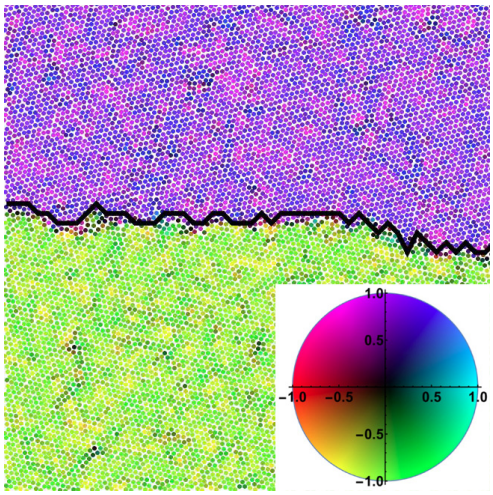

Fig. 2.1 Snapshot of a hard-sphere monolayer at fugacity 1×10^7 with the GBs presented in a $200\sigma\times200\sigma$ box (only one GB in a region $100\sigma\times100\sigma$ is shown here for clarity). The spheres are color-coded by order parameter Ψ_6 represented by the color shown in the inset. The x and y axis represent the real and imaginary part of Ψ_6, respectively.

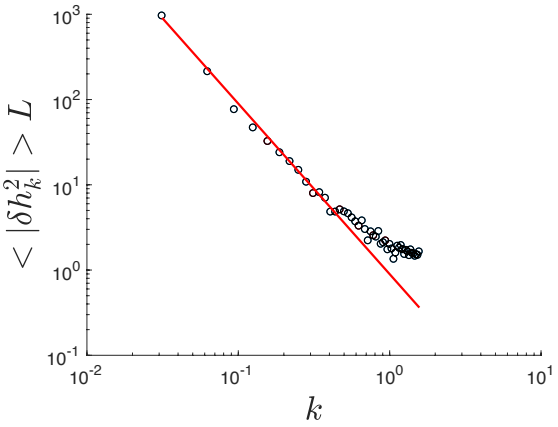

Fig. 2.2 F.T. spectrum of the fluctuation of GB at fugacity f=1.0×10^7 in a $200\sigma\times200\sigma$ box. Red line is the linear fit of the spectrum data (circle points) with slope fixed at -2.

To detect the variation in the position of the two GB's along the x dimension, we divide the simulation box into a 100×100 grid. Multiple tests showed this granularity is fine enough, and that the use of smaller grid squares does not affect the stiffness calculated. The average of the θ_6 for particles in each grid and the four nearest grid squares of the same x coordinate is measured to represent the orientation of each grid square. (Averaging over several grid squares in the y direction serves to smooth over noise associated with local pockets of disorder, whether at the boundary or elsewhere, which otherwise lead to false indications of the GB location.) The height h of the grain

boundary is taken as the *y* coordinate of the "edge point" grid square, defined as the grid square with θ_6 closest to the mean of the θ_6 values of the two grains. The GB is represented by connecting "edge points" all together (Fig. 2.1).

2.2.4 Capillary Fluctuation Method

The capillary fluctuation method is commonly used to relate the wavelength-dependent fluctuation of the interface to the interfacial free energy or stiffness in a variety of contexts.[21, 26, 29, 30] GBs in each frame during the simulation are represented by the method discussed above, which can be described by a function of the distance along the x direction and frame t: $h(x,t)$. To correct for drift or diffusion of the GB over the course of the simulation we use fluctuations relative to the current mean position of the GB: $\delta h(x,t) = h(x,t) - \langle h(t)\rangle_x$. For each frame, the following Fourier Transform (F.T.) can be written:

$$\delta h(k) = \frac{1}{L}\int_0^L \delta h(x)\exp(-ikx)\,dx \tag{2.2.6}$$

Each frame's spatial fluctuation $\delta h(x)$ is transformed using Eq. (2.2.6) into $\delta h(k)$, which is the intensity of the mode with wave number k in Fourier Spectrum, where $k = 2\pi m/L$ ($m = 0, \pm1, \pm2, ...$) and L is the length of GB. $\langle|\delta h(k)|^2\rangle$ is calculated as an average over all frames, and is related to the stiffness Γ of the GB by CFM[31]:

$$\log(\langle|\delta h(k)|^2\rangle L) = -2\log(k) + \log\left(\frac{k_B T}{\Gamma}\right) \tag{2.2.7}$$

In practice, a linear fitting of Eq. (2.2.7) with a fixed slope –2 is performed to fit the F.T. spectrum to find stiffness Γ from the *y*-intercept (Fig. 2.2). We found in general that the power spectrum of fluctuations deviated upward from the low-*k* trend at high *k* (i.e. short wavelength). The CFM is derived from continuum theory and so is not expected to fit fluctuations with high *k*. The apparent crossover to a different high-*k* regime was dependent on the system, but for a general

rule points with $|m|$ higher than 15 (corresponding to $k > 0.5\ \sigma^{-1}$, or the wavelengths < 12 σ) are excluded from the linear fitting. The enhanced local fluctuations of the interface on wavelengths significantly longer than a single particle diameter may be related to local melting and/or to uncertainty in defining the precise boundary positions.

2.2.5 Implementation details

A domain-decomposition scheme is used to parallelize the simulations. The system (with a box size $200\sigma \times 200\sigma$ or $300\sigma \times 300\sigma$ in stiffness calculation, $200\sigma \times 200\sigma$ or $250\sigma \times 250\sigma$ in dynamic study) was divided into an 8×8 or 12×12 grid with a randomly selected origin. In each MC cycle, a predetermined number of MC move attempts were performed independently within each grid square on separate processors, with no addition, removal, or translation of particles within a zone of distance of 0.5σ from domain borders. For GCMC simulation of GB fluctuations, each MC cycle contains 1000 SRMC move attempts followed by 2000 regular translation move attempts (max. displacement of 0.05σ) performed in each grid square. After every MC cycle, a new origin for the grid was chosen and particles are redistributed among processors so that the border regions are constantly changing. To sample GB fluctuations $\delta h(x)$, the equilibration and production periods consisted of at least 5000 and 20000 MC cycles, respectively, within the grand canonical ensemble.

In studies of the evolution of 2- and 4-grain systems, an equilibration period of 1000 MC cycles as defined above was used to allow the GB to relax from their initial straight arrangements and to allow the ordered grains to reach a steady density.

Dynamic MC studies were performed under canonical ensemble conditions (at constant N and A). At least 3000 MC cycles are run, with 20000 regular translation moves per domain in each cycle.

Reduced units, scaled to the particle diameter σ and the thermal energy $k_B T$ are used throughout. The pressure P^* (in units of $k_B T/\sigma^2$) was calculated using the radial distribution at contact[101]:

$$P^* = \rho + \frac{\pi}{2}\rho^2 g(1_+) \tag{2.2.8}$$

with $\rho = N/A$. The radial distribution at contact is obtained by fitting the pair distance histograms to a third-order polynomial out to 1.05 times the contact length. Area fraction η is calculated as to $\pi\rho/4$, corresponding to the projected area of non-overlapping spheres on a flat surface or the area coverage of discs of unit area. The bulk area fraction is measured using the average number density within the grains' interiors.

2.3 Results and Discussion

The first part of this section demonstrates the systematic measurement of stiffness under various conditions including box size, pressure (varied through changing particle chemical potential), misorientation and inclination. Enthalpic and entropic contributions to the stiffness will be discussed. The second part focuses on a phenomenon we noticed from our simulation: GB buckling or faceting during a gradual increase in the system pressure. The apparent origins of this phenomenon and implications for simulation approaches and the behavior of experimental systems under compression will be discussed. The last section presents the results of dynamic studies that test how the stiffness of GB correlate with the dependence of grain growth rates on orientational factors.

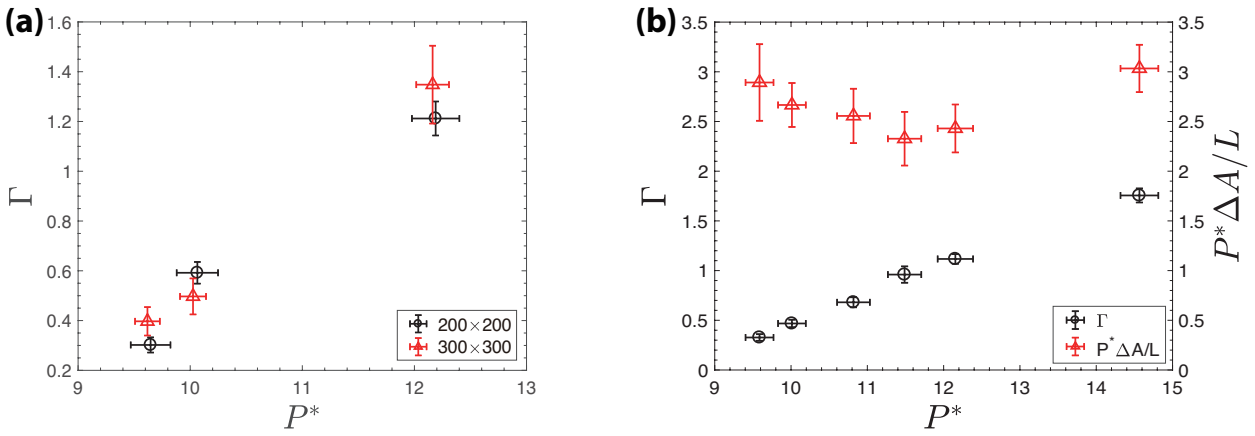

Fig. 2.3 Stiffness dependence on (a) system size with fixed GB misorientation 27.4° and inclination 11.1°; (b) pressure with fixed system size $200\sigma\times200\sigma$, misorientation 30° and inclination 15°. The product of pressure with excess surface area per unit length of GB ($P\Delta A/L$) is also shown in (b).

2.3.1 Stiffness and line tension

We first studied the stiffness dependence on system size. In principle, system size should not affect the GB. Practically, GB may suffer from the finite size effect in simulations. Simulations at $100\sigma\times100\sigma$ were tested but were not pursued because the drift in GB positions would sometimes bring them close enough together for a grain to fuse with its periodic image. We compared results of simulations under three pressures with different system size ($200\sigma\times200\sigma$ or $300\sigma\times300\sigma$), keeping misorientation and inclination the same (Fig. 2.3(a)). No significant difference is observed. The increase in computational expense to equilibrate the fluctuations with increasing box length L is expected to scale as L^3, as the number of particles scales with L^2 while the relaxation time of the longest-wavelength mode scales with L.[26] Therefore, for efficiency and to allow better convergence, all following simulations are performed with a box size $200\sigma\times200\sigma$ (except one case in the section *2.3.3* which required a larger box size). Although this range of box sizes is not wide enough to rule out the possibility of finite-size effects, the general agreement at these system sizes, the absence of a systematic size-dependent trend in the calculated stiffness, and considerations of

efficiency and statistical sampling led us to adopt a box size $200\sigma \times 200\sigma$ for all further stiffness calculations. The stiffness dependence on pressure is studied with a fixed misorientation and inclination (Fig. 2.3(b) and Table 2.1). A linear relation is observed. A GB stiffness has been evaluated as 1.7×10^{-15} J m^{-1} from experimental images of a fluctuating GB in a system of 2.7 μm colloidal particles[21] at a number density of 0.11 μm^{-2}. Upon conversion to reduced units ($k_B T/\sigma$) this corresponds to Γ= 1.1, in good qualitative agreement with the present simulation results. We hesitate to examine the agreement in stiffness values between experiment and simulation more closely, because of the difficulty in calibrating the state of the experimental system onto the simulation conditions with sufficient precision.

Fig. 2.4(a) and (b) shows the stiffness dependence on misorientation and inclination. A higher stiffness is observed as the misorientation increases. Stiffness and enthalpy show the same dependence on misorientation. No significant dependence on inclination is seen in either the stiffness or the enthalpy of the grain boundary. These results are consistent with a recent experimental study of the dynamics of 2-d colloidal grain growth,[24] which showed boundaries between neighboring grains with large misorientations disappeared faster than low-misorientation boundaries, but that the probability distribution of GB was uniform and unchanging with respect to inclination angle. From this we may conclude that the second derivative of GB free energy with respect to angle of inclination must be small, and that therefore the line tension can be assumed equal to the stiffness to a very good approximation.

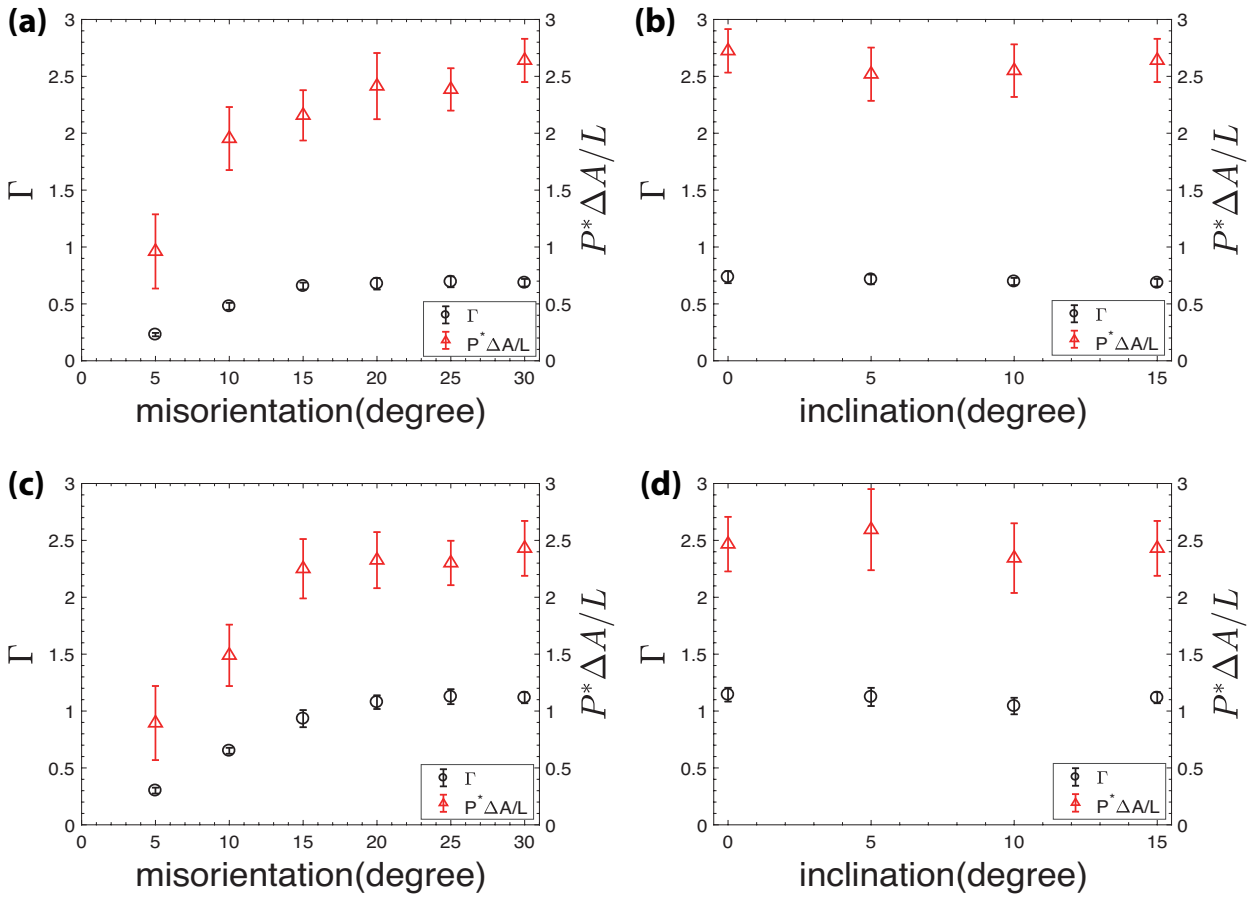

Fig. 2.4 Stiffness and excess interfacial enthalpy per unit length of GB ($P^*\Delta A/L$) from simulations at system size $200\,\sigma \times 200\,\sigma$ on (a) misorientation with and inclination 15° at fugacity 2.0×10^6; (b) inclination with fixed misorientation 30° at fugacity 2.0×10^6; (c) misorientation with inclination 15° at fugacity 1.0×10^7; (d) inclination with misorientation 30° at fugacity 1.0×10^7.

Given that the stiffness extracted from simulation can be treated as a line tension (excess free energy per unit length), it is instructive to analyze the components of that free energy. Since the potential energy of the HS system is zero for all allowable configurations and the kinetic energy per particle is only a function of temperature, the excess internal energy of the GB is zero. The excess enthalpy ΔH for this 2-d system in reduced units is therefore $P^*\Delta A$, with ΔA the excess area (the area difference in area between a uniform system and a system with the same number of particles having a GB). The excess entropy associated with the GB at constant surface pressure is therefore $T\Delta S = P^*\Delta A - \Delta G$, and so the excess entropy per unit length of the GB is $\Delta S/L = (P^*\Delta A/L$

- Γ). The red symbols in Fig. 2.3(b) and Fig. 2.4 show the product of pressure P^* with excess surface area ΔA per unit length L of the GB. The difference between the red symbols and Γ reflects the excess interfacial entropy per unit length, which decreases with increasing pressure to about P^*=12 and then levels off. The dependences of enthalpy on GB misorientation and inclination at constant fugacity (Fig. 2.4(c) and (d)) track the corresponding dependences of stiffness on these properties.

As pressure is decreased toward the melting pressure, the excess area per unit length associated with the boundary increases significantly (from about 0.2 σ to about 0.3 σ.) This is caused by the interface widening as it turns into a locally liquid region, an example of pre-melting as has been observed at grain boundaries in a variety of polycrystalline systems[102-104]. In fact, the presence of a wide and fluctuating pre-melted zone made it impossible to evaluate the position of the interface at pressures below 9.5 $k_B T/\sigma^2$.

Pre-melting to a fluid layer of width w is expected to be spontaneous when the line tension between the two solid grains is greater than the combination of the combined fluid-solid interfacial tensions of the two solid-fluid interfaces formed[102], plus a bulk contribution (which vanishes at the transition pressure) that is proportional to w. The fluid-solid interfacial tension is not easily obtained since the 2-d solid and fluid phases do not coexist at equilibrium. Instead we consider the experimentally derived interfacial stiffness values reported by Thorneywork *et al.*[7] for the fluid-hexatic interface at coexistence at an inclination 15°. Converted into reduced units, this gives an estimate for the fluid-solid interfacial tension of Γ = 0.085. When we use the data in Fig. 2.3(b) to extrapolate our stiffness dependence to the transition pressure (P^*=9.18), we find the corresponding stiffness (Γ = 0.235) to be higher than twice this estimate, consistent with the observed pre-melting at the GB.

Table 2.1 Physical properties of systems at different pressures, with misorientation 30° and inclination 15° in a $200\sigma \times 200\sigma$ simulation box. Area fraction listed is taken from grain interiors.

fugacity	P^*	area fraction η	Γ
6×10^5	9.58±0.18	0.7269±2E-4	0.327±0.033
1×10^6	10.01±0.18	0.7341±3E-4	0.468±0.038
2×10^6	10.82±0.21	0.7456±1E-4	0.681±0.050
5×10^6	11.49±0.22	0.7539±2E-4	0.960±0.082
1×10^7	12.15±0.23	0.7611±2E-4	1.117±0.049
1×10^8	14.56±0.25	0.7825±9E-5	1.756±0.071

2.3.2 GB buckling during dynamical pressure compression

When we investigated the stiffness dependence on pressure, we noticed that equilibration of systems at high pressure $P^* = 14.56$ (corresponding to fugacity of 1.0×10^8) when starting from a lower area fraction (η=0.740) configuration tended to produce structures with buckled or faceted GB. An example is shown in Fig. 2.5. Upon extending the trajectory, this buckled structure might evolve but would not relax to a flat boundary within a reasonable time for simulation. The CFM analysis in such cases produced an amplitude spectrum that did not fit the k^{-2} model well at all, because the assumption of sampling over amplitudes at all wavelengths was not met. The spontaneous adoption of facets could be the result of a strong dependence of interfacial free energy on the angle of inclination, in apparent contradiction to our findings above. In this case, however, the buckling occurred no matter the angle of inclination; setting up the ribbon with inclination at 0° still produced facets.

The buckling occurred during equilibration under GCMC conditions while the total number of particles in the simulation was increasing. To determine whether buckling was a by-product of this non-equilibrium process, we constructed an ideal, defect-free hexagonal domain with an area fraction close to the value at the desired pressure (P^* =14.56). In this case, the buckling was not observed, and the CFM method yielded well-behaved results that were consistent in trends from lower pressure (shown in Fig. 2.3(b)). Starting with an ideal, defect-free domain at a lower area fraction, and allowing the density to increase via particle exchange at the higher fugacity, produced buckling. It can then be concluded that the GB buckling is related to the non-equilibrium process of increased densification of the grains at constant area through particle addition, which (through a mechanism that is unclear – not observably related to the creation or annihilation of specific dislocations) caused uneven stresses in the system that were relaxed through deformation of the GB. A recent experimental study by Cash *et al.*[98] showed that formation of a locally melted region near a GB following a laser "blast" produced a deformation of the grain boundary in what may be a related phenomenon. It is conceivable that other experimental cases where particles continue to add to a polycrystalline ordered surface could produce a similar buckling effect on GB.

We have noticed that, compared with GCMC simulations in a square, monocrystalline, periodically repeating system, systems containing GB are much faster at the relaxation of total particle numbers and increasing local packing density in the 2-d ordered state. The apparent reason is that the GB can act as both a source and a sink of dislocations, allowing the lattice constant to shrink at constant box dimension via the addition of rows to the domain stripes. This is perhaps

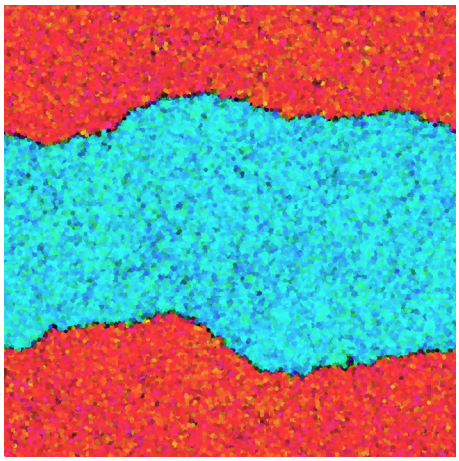

Fig. 2.5 Snapshots of the buckled configuration with GB misorientation at 30° and inclination 0° after 23000 MC moves in grand-canonical ensemble at fugacity $f = 1 \times 10^8$, initiated from a lower-density structure. This snapshot is color-coded by order parameter Ψ_6 as shown in Fig. 2.1.

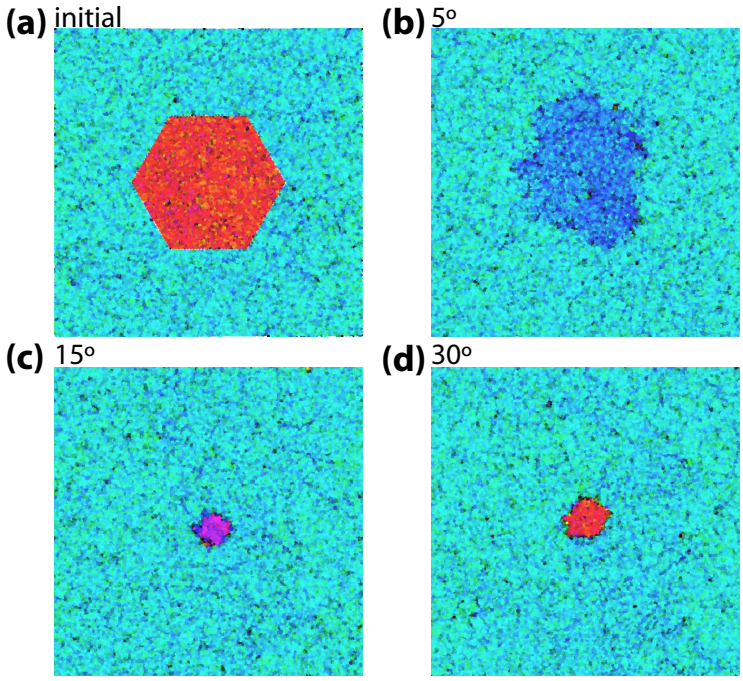

Fig. 2.6 (a) Starting arrangement shape of 2-grain system showing to indicate initial size and shape of misoriented domain; 30° misorientation shown. (b)-(d) Snapshots of the configuration after 7000 MC moves in grand-canonical ensembles for GB misorientation 5°, 15° and 30°. All snapshots are color-coded by order parameter Ψ_6 as shown in Fig. 2.1.

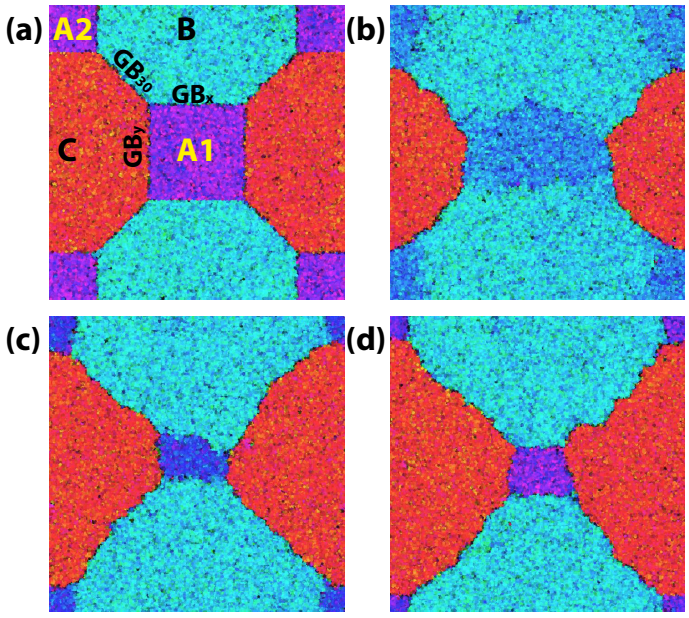

Fig. 2.7 (a) Snapshot of an initial configuration in a 4-grain system with misorientation 15° for both GB_x and GB_y; Snapshots of the configuration after 40000 MC moves in constant-N ensemble in a 4-grain system with GB_x misorientation (b) 5°; (c) 10° and (d) 15°. All snapshots are color-coded by order parameter Ψ_6 as shown in Fig. 2.1.

the flip side of an experimental observation by Deutschländer *et al.*[105], that polycrystalline 2-d systems quenched rapidly into melting conditions will generate defects preferentially near grain boundaries, which proceed inward to melt the ordered domains.

2.3.3 Dynamics of grain coarsening

Although Monte Carlo simulation does not produce a trajectory that is directly related to a dynamic algorithm, the evolution of a MC trajectory that uses local displacement moves (as opposed to the unphysical SRMC moves that can incorporate changes in particle number and collective rearrangements) can give qualitative insight into dynamics. This is particularly true for colloidal systems where Brownian dynamics might be a good approximation.[57] To determine how the MC dynamics of grain coarsening are influenced by grain and GB orientations, we first modeled an isolated hexagonal domain at misorientations of 30°, 15°, and 5°. The system containing a hexagonal domain (with an edge length 50σ) is constructed within a $200\sigma \times 200\sigma$ box

(Fig. 2.6 (a)). The six GBs in each system have the same inclination as well, due to the symmetry of the hexagon. After 1000 MC cycles under grand canonical simulation, the shapes of the original hexagon shape cannot be recognized due to the fluctuation of the GB. Fig. 2.6 shows the snapshots after 7000 MC cycles. The shrinking rate for the domain with misorientation 5° is much slower than other two systems, which shrink on similar timescales. Taken together with the results of Fig. 4(c), these observations suggest that the GB shrinking rate is correlated with stiffness, as $\Gamma(5°) < \Gamma(15°) \approx \Gamma(30°)$. Results obtained under constant-N ensemble simulation (not shown) are qualitatively similar. We also constructed the system containing a square domain (not shown) with the same area as the hexagonal domain, where GB at different direction will have different inclination. The result shows no apparent difference between the rates of shrinking in X and Y dimensions, confirming that the shrinking rates depend negligibly on inclination.

A more complex system containing tiled octagonal and square grains with three different orientations was constructed as shown in Fig. 2.7(a), to further study how misorientation affects the domain coarsening when triple junctions (TJ) are present. Varying the orientation of the square domain (A1, A2) enables us to compare the shrinking rates of GB with different misorientations (GB_x, GB_y) in the same domain. The octagonal grains B and C have fixed θ_6 (0° and 30°, respectively) which fix the misorientation of GB_{30} at 30°. A larger simulation box ($250\sigma \times 250\sigma$) is used so that GB_{30} is not too short. Three cases are shown where the misorientation for GB_x is 5°, 10° and 15° (denoted as MisX5, MisX10 and MisX15, respectively); the corresponding misorientation for GB_y is then 25°, 20° and 15°, respectively.

The shrinking rates are much slower compared to the two-domain systems. One reason is that if the square domains maintain their shape as they shrink, the reduction in GB length of the square will be counterbalanced by the increase in the octagon/octagon GB length, so the driving force (if

all line tensions are equal) is lower by a factor of $(1\text{-}2^{-1/2})$. Friction associated with the TJ motion may also contribute. The order of overall shrinking rate is MisX5 < MisX10 ≈ MisX15 (Fig. 2.7), which can still be explained by the sum of the stiffness of GB_x and GB_y. After 40000 MC cycles, the central domain (A1) becomes roughly rectangular (Fig. 2.7(b) and (c)), with the more-misoriented GB shrinking faster, consistent with the increase in stiffness with misorientation angle. In the case of MisX5, the 5° GB_x actually expands as domain C (along with the BC grain boundary) shrinks, again consistent with the stiffness predictions. The general behavior is in full agreement with the experimental results and explanations given by Lavergne *et al*.[24], who found that low-misorientation GB tended to grow at the expense of high-misorientation GB in polycrystalline systems, and observed isotropic distributions of GB inclination angles at all misorientations. In concert with the CFM results presented earlier, these findings illustrate the influence of the thermodynamic property (line tension) on the dynamics.

2.4 Conclusions

The stiffness of grain boundaries in a two-dimensional hard-sphere system at packing fractions above the freezing transition has been analyzed using the capillary fluctuation method and grand canonical Monte Carlo. Stiffness was found to increase linearly with pressure, to be sensitive to misorientation of the grains (increasing steadily up to ~15° and changing slightly at higher angles) and to be nearly insensitive to the inclination of the GB with respect to the domains. The insensitivity to inclination indicates that in this system, it is a good approximation to equate the observed stiffness with the thermodynamic line tension. The enthalpic contribution to the line tension arising from the excess area decreases at low pressures, reaches a minimum, and increases as the excess area of the GB apparently approaches its minimum. Dynamic simulations of 2- and

4-grain systems arranged in simple geometries demonstrate the relevance of these findings to misorientation effects on grain coarsening rates, and are fully consistent with recently published experiments of 2-d colloidal grain coarsening dynamics.[24] The current results could be useful in providing input parameters for mesoscale modeling of grain growth in these systems,[106-108] as well a foundation for further studies of impurity segregation at GB in bidisperse hard-sphere monolayers.[40]

Chapter 3

Partitioning of Size-mismatched Impurities to Grain Boundaries in 2-d Solid Hard Sphere Monolayers[2]

Computational studies have been carried out to investigate the equilibrium partitioning of size-mismatched impurities between the bulk solid and grain boundary (GB) environments in 2-d hard-sphere monolayers. The Solvent Repacking Monte Carlo method and a new variation were used to exchange varying numbers and types of particles under conditions of fixed particle fugacities, allowing efficient sampling of impurity particle distributions even within the bulk solid. Measurements of GB stiffness depression arising from the impurities were made via the capillary fluctuation method, and found to agree with calculations based on the Gibbs adsorption isotherm, providing a test of the internal consistency of the results. The dependence of the excess concentration at the GB on factors including impurity size (diameter ratios λ=0.5 to 4 times the majority host particle diameter), impurity concentration, grain misorientation angle, and packing pressure were studied. In general, the affinity of impurity particles for GB increased with the difference between their size and the host particles, and varied with grain misorientation angle with a dependence reflecting the excess free area at the GB. Impurities with λ=4 were exceptions to both these trends, due to their ability to substitute efficiently for 6-coordinate host particles within the bulk and for 5-coordinate host particles at dislocations in the grain boundaries. Comparison with results from an experimental study of mixed colloidal monolayers raises

2. Adapted with permission from Guo, Z. and Kindt, J. T., ***Langmuir***. 34(43), 12947 (2018). Copyright 2018 American Chemical Society.

questions about how kinetic effects during grain coarsening might produce less impurity segregation to the GB than equilibrium exchange.

3.1 Introduction

The grain boundary (GB), the interface between two ordered domains, is very important in the study of polycrystalline materials.[10, 41, 109] In a polycrystalline alloy, impurities tend to be adsorbed in GB, an effect known as GB segregation,[33-40] for the general reason that GB can provide more free volume than bulk domains. Interactions between impurities and GB can affect the mechanical properties of polycrystalline alloys[41] through impurity drag,[32, 42] or Zener pinning,[32, 43, 44] which also play important roles on the grain growth.[45, 46] Understanding of GB segregation is crucial to combating intergranular weakness in the steel industry[35] and improving stability of nanocrystalline alloys.[34, 39]

Colloidal polycrystalline monolayers with impurities are useful model systems to study GB segregation and grain growth.[96, 110, 111] The large size (~μm) and slow dynamics (~s) of colloidal particles allow direct observation of their behavior by optical microscopy in experiments.[3, 4] Quasi-2d colloidal monolayers can be prepared by confining spherical colloidal particles between surfaces[98] or depositing them onto a liquid[97] or solid surface.[24] When interactions between particles are dominated by short-ranged repulsions, the colloids can be modeled as hard spheres (HS).[7] A mixture of hard spheres resting on a common plane (with thermal fluctuations in the vertical dimension suppressed by gravity) maps onto a non-additive HD mixture, with the distance of closest approach in the plane between spheres of different size given by the geometric mean, not the arithmetic mean, of the particle diameters.[40] Here we will assume the majority component (host particles) will have diameter 1; an isolated impurity sphere of diameter λ (which also represent

the diameter ratio in this work), embedded among host spheres, will behave equivalently to a disc of diameter $2\sqrt{\lambda} - 1$ interacting with host disks of diameter 1. The set of configurations available to a system of monodisperse HS confined to a planar surface is congruent to those of hard discs (HD), and so is expected to follow the two-stage ordering transition seen in simulations of HD systems.[5, 6] Low concentrations of added impurities in simulations of HD systems have been shown to suppress the stability of the intermediate hexatic phase in favor of a broader liquid-solid coexistence region.[9] The results presented here, as in our previous study of GB,[112] will be under conditions where the host particles are in a 2-d solid state.

The presence of impurities will tend to influence both thermodynamic and dynamic properties of the GB. The thermodynamic stability of a GB is encapsulated in its stiffness Γ. A measure of the GB resistance to curvature fluctuations, stiffness is the sum of the interfacial line tension γ (excess free energy per unit length of the GB) and its second derivative with respect to GB orientation, γ''. In our previous simulation study of monodisperse HS monolayers we were able to quantify how misorientation (the difference in orientation between the two neighboring crystal grains) and inclination (the orientation of the GB line) affect Γ.[112] The observation that stiffness depends very little on GB inclination in this system leads to $\gamma'' \approx 0$ and the useful simplifying approximation $\Gamma = \gamma$. Here we use the solvent repacking Monte Carlo (SRMC[8]) method, along with a new extension called mixed repacking Monte Carlo (MRMC), to study how segregation of impurities towards GB depends on impurity size, impurity concentration, and GB orientation. Where possible, results are compared with experimental observations reported by Lavergne *et al*.[40] Impurity-dependent lowering of GB line tension was also calculated from the degree of segregation using the Gibbs adsorption isotherm, and checked against calculations of stiffness in GB systems containing impurities using the capillary fluctuation method (CFM).[31] The agreement

between these calculations is further evidence that in these particular systems, the stiffness can be treated as equivalent to the line tension.

A general trend that impurity segregation increases with increased mismatch between impurity and host size was observed, with an exception for spheres of diameter λ=4. As discussed in previous reports,[40] this size impurity sphere has a nearest neighbor distance of 2 host diameters, and so (like impurity disks of diameter 3 in additive HD systems[8]) can efficiently pack in a hexagonal lattice by occupying a lattice site and its six nearest neighbors. An impurity sphere of size 2.25, on the other hand, which Lavergne *et al.*[40] highlighted for its ability to fit within a hexagonal lattice while centered at an interstitial site, did not show distinctive behavior. Quantitative comparison with the degree of segregation observed in experimental colloidal monolayer showed much higher segregation in the initial simulations than in experiment. Subsequent tests pointed to two plausible explanations for this discrepancy: that simulation conditions corresponded to a higher surface pressure than experiment, or that the slow motion of impurities combined with the non-equilibrium dynamics of grain coarsening could inflate levels of impurities left in the bulk. The degree of impurity GB segregation at different grain misorientation angles was investigated for several impurity sizes. This dependence, for impurity sizes 1.4 and 3, was similar to the dependence of excess area on GB misorientation as previously measured.[112] Impurities of size 4 again behaved exceptionally, showing a much stronger increase in affinity for the GB with misorientation angle. We propose an explanation for this difference that is based on the substitution of these impurities at 5-coordinate sites present at the GB.

3.2 Methods

3.2.1 System Construction and initialization

To systematically study the GB stiffness and their dependence on system composition under controllable conditions, ordered grains of spheres are set up in a pair of parallel stripes making two parallel GBs aligned with the x direction as in previous work[112] in a square simulation box with periodic boundary conditions. The use of parallel stripe grains provides a controlled misorientation between the grains and a fixed inclination between the boundary and the grains; furthermore, the lengths of the boundaries are fixed (apart from fluctuations) by the box length, so fluctuations in the overall sizes of the grains are decoupled from changes in the interfacial energy.

3.2.2 Mixed Repacking Monte Carlo

In the "solvent repacking Monte Carlo" method for mixtures, a single large particle is added or removed in exchange for a variable number of small particles without moving any other large particles.[8] This is effective when small particles occupy a majority of the system area, but if large particles are densely packed then the probability of finding a position to insert a large particle that does not overlap other large particles becomes vanishingly low. To facilitate fluctuations in structure and composition in such a system we allow for rearrangement of both large and small particles within a local cavity to accompany the addition or removal of large particles using a "mixed repacking Monte Carlo" move.

As in the SRMC algorithm, after choosing a point at random in the system, a trial move is generated with a new packing for particles in a circular cavity centered at that point. In this study the range of repacking for large particles was set equal to the large particle diameter, while the range for small particles was extended to 1.5 times the large particle diameter. The volume of corresponding repacking region is denoted as $v_{cav,S}$ and $v_{cav,L}$, respectively. One of three types of move attempts (with large particle number change $\Delta N_L = -1,0,+1$) is chosen with equal

probability. In each case, repacking of large particles in the cavity is attempted first, up to the new number of large particles, and then the change in number of small particles is determined by the weightings of the states generated by successive addition of small particles. For large particle addition, a number k of trial positions are generated that randomly and uniformly sample the cavity region in each cycle i to generate the ith large particle in cavity. The j'th position will then be selected with a probability:

$$P_{i,j'} = \frac{\exp\left(-\beta u'_{i,j'}\right)}{\sum_{j=1}^{k} \exp\left(-\beta u'_{i,j}\right)} \tag{3.2.1}$$

where $u'_{i,j'}$ is the auxiliary potential for the interaction of the j'th particle with particles inserted in previous cycle and the solvent shell around the cavity. The logarithm of the radial distribution function (RDF) for hard spheres with an area fraction 0.69 is used for the auxiliary potential in this work; this and choices for *k* were consistent with previous work.[8] $P_{i,j}$ is zero if the particle overlaps particles in the surrounding shell or particles already selected for insertion into the cavity; if there are no positions with non-zero *P*, the move fails.

Once $n_{cav,L}$ large particles have been inserted, this process will be repeated to insert small particles into the cavity, until some predetermined conditions are met: either small particle number in cavity reach a maximum (20 in this work) or none of the *k* trial positions are successful. The probability for selecting a configuration with a number of $n \in \{0, i\}$ small particles is:

$$P(n) = \frac{\omega_n}{\sum_{i=0}^{n_{max}} \omega_i} \tag{3.2.2}$$

where the weight ω_i associating the configurations with a number of i particles can be calculated as:

$$\omega_i = \frac{f^i}{{\Lambda_S}^{di}} \frac{{v_{cav,S}}^i}{i!K} W'_i \frac{\exp\left(-\beta U_i\right)}{\exp\left(-\beta U'_i\right)} \tag{3.2.3}$$

where Λ_S is the de Broglie thermal wavelength (set to 1 in all simulations) of the small particle; d is the dimension of the system; $K = \prod_{i'=1}^{i} k_{i'}$, which is the product of number of trial positions k for all the previous cycles; U_i and U_i' are the true potential energy (always equal to zero) and the auxiliary bias potential energy, respectively; W_i (or W_i' when applying auxiliary potential) is the Rosenbluth weight defined as:

$$W_i = \prod_{i=1}^{n_{cav}} \sum_{j=1}^{k} \exp\left(-\beta u_{i,j}\right) \tag{3.2.4}$$

Weights ω_i associated with the current configuration of particles also need to be calculated, which requires the current cavity configuration to be reconstructed in the same manner. The overall acceptance probability for transition from current state with $n_{cav,S}$ small particles in cavity to the new state with $n_{cav',S}$ small particles and the same number of large particles N_L can be written as:

$$acc_{n_{cav,S},n_{cav,L}\to n_{cav',S},n_{cav,L}} = \min\left[1, \frac{W_{L,new}}{W_{L,current}} \frac{\sum_{i=0}^{n_{max,new}} \omega_{i,new}}{\sum_{i=0}^{n_{max,current}} \omega_{i,current}}\right] \tag{3.2.5}$$

For attempt moves with $\Delta N_L = \pm 1$, the same strategy is used except the different point for switching over to small particle insertion. The corresponding acceptance probability for $\Delta N_L = +1$ is:

$$acc_{n_{cav,S},n_{cav,L}\to n_{cav',S},n_{cav,L}+1} = \min\left[1, \frac{n_{cav,L} v_{cav,L}}{(n_{cav,L}+1) k_{n_{cav,L}+1}} \frac{f_L}{\Lambda_L^d} \frac{W_{L,new}}{W_{L,current}} \frac{\sum_{i=0}^{n_{max,new}} \omega_{i,new}}{\sum_{i=0}^{n_{max,current}} \omega_{i,current}}\right] \tag{3.2.6}$$

f_L is the fugacity of large particle; Λ_L is the de Broglie thermal wavelength (set to 1 in all simulations) of large particle. The acceptance probability for $\Delta N_L = -1$ can be similarly derived as:

$$acc_{n_{cav,S},n_{cav,L}\to n_{cav',S},n_{cav,L}-1} = \min\left[1, \frac{n_{cav,L} k_{n_{cav,L}}}{(n_{cav,L}-1) v_{cav,L}} \frac{\Lambda_L^d}{f_L} \frac{W_{L,new}}{W_{L,current}} \frac{\sum_{i=0}^{n_{max,new}} \omega_{i,new}}{\sum_{i=0}^{n_{max,current}} \omega_{i,current}}\right] \tag{3.2.7}$$

3.2.3 Order parameter and GB detection

The local crystalline order of particle j, containing N_j neighbors within a cutoff $1.5\sigma_h$, is characterized by bond-orientational order parameter[100] Ψ_6:

$$\Psi_6(\vec{r}_j) = \frac{1}{N_j}\sum_{k=1}^{N_j} e^{i6\Delta\theta_{jk}} \tag{3.2.8}$$

where $\Delta\theta_{jk}$ is defined as the angle between the x direction and the vector connecting particle j and its neighbor indexed k. The orientation of the hexagon formed by six neighbors of particle j can then be calculated by $\theta_6 = \arg(\Psi_6)/6$, which lies in the range 0 - 60° due to the symmetry of hexagon. The orientation of the grain domain can be quantified by averaging all the θ_6 of host particles belonging to the domain.

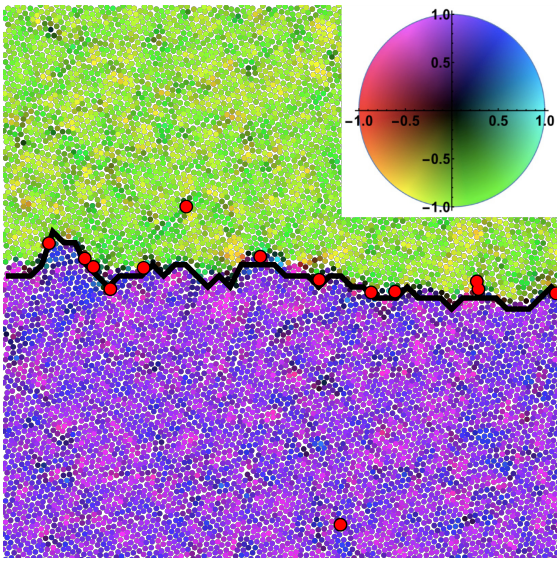

Fig. 3.1 Snapshot of a hard-sphere monolayer mixture with a 1.4 size ratio at host particle fugacity 1×10^7 and impurity fugacity 5×10^9. Only one GB in a region $100\sigma_h\times100\sigma_h$ is shown here for clarity. Impurities are shown in red, at greater than actual size to aid visualization. The host particles are color-coded by order parameter Ψ_6 represented by the color map shown in the inset; the x and y axis represent the real and imaginary part of Ψ_6, respectively.

To identify the positions of the two GB's along the x dimension, we divide the simulation box into a 100×100 grid, which has been confirmed to be fine enough for calculating interfacial stiffness in our previous study.[112] Smoothing over local pockets of disorder is achieved by taking

the average of θ_6 in each grid and the four nearest grid squares of the same x coordinate to represent the orientation of each grid square. The height h of the grain boundary is then the y coordinate the grid square with θ_6 closest to the mean of the θ_6 values of the two grains, defined as the "edge point", and the GB is represented as a sequence of segments connecting "edge points" (Fig. 3.1).

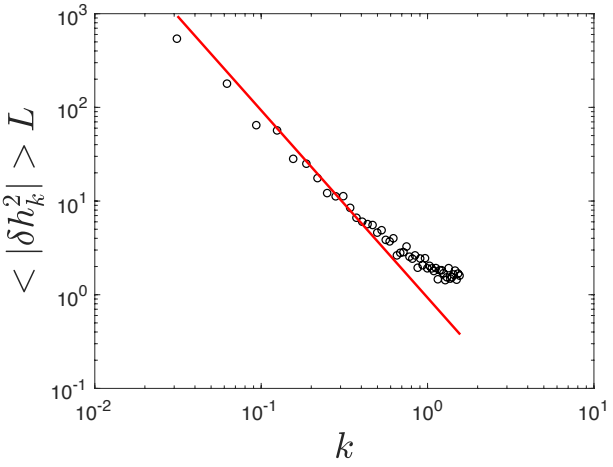

Fig. 3.2 F.T. spectrum of the fluctuation of GB for the system with a 1.4 size ratio at host particle fugacity 1×10^7 and impurity fugacity 5×10^9 in a $200\sigma_h \times 200\sigma_h$ box. Red line is the linear fit of the spectrum data (circle points) with slope fixed at -2.

3.2.4 Capillary Fluctuation Method

The CFM is applied here in the same way as in previous work to calculate GB stiffness.[112] The GB positions along the y direction determined as described in the section "Order parameter and GB detection" are treated as a function of position along the x direction and frame t: $h(x,t)$. The mean value of $h(x,t)$ at each t is subtracted off to yield the fluctuation at that frame: $\delta h(x,t) = h(x,t) - \langle h(t) \rangle_x$. At each frame analyzed, the Fourier Transform (F.T.) of the fluctuation function is calculated:

$$\delta h(k) = \frac{1}{L}\int_0^L \delta h(x) \exp(-ikx)\, dx \tag{3.2.9}$$

to yield $\delta h(k,t)$, which is the intensity of the mode with wave number k in Fourier Spectrum, where $k = 2\pi m/L$ ($m = 0, \pm1, \pm2, \ldots$) and L is the length of GB. The trajectory-averaged square of intensities $\langle|\delta h(k)|^2\rangle_t$ are related to the stiffness Γ according to the CFM as:[31]

$$\log(\langle|\delta h(k)|^2\rangle L) = -2\log(k) + \log\left(\frac{k_B T}{\Gamma}\right) \tag{3.2.10}$$

In practice, a linear fit of Eq. (3.2.10) with a fixed slope –2 is used to find stiffness Γ from the *y*-intercept (Fig. 3.2). The CFM is derived from continuum theory and so is not expected to fit fluctuations with high *k*. In this study we found excluding points with $|m|$ higher than 15 produced satisfactory results in all cases.

3.2.5 Gibbs adsorption isotherm

The depression of stiffness due to the presence of impurity can be predicted from segregation data using the Gibbs adsorption isotherm:

$$-d\gamma = \sum_{i=1}^{I} \Delta N_i d\mu_i \tag{3.2.11}$$

where γ is the line tension, ΔN_i is the interface excess of component i, and μ_i is the chemical potential. We are performing simulations at fixed chemical potential of the host particle, so the only component contributing to the summation in Eq. (3.2.11) as impurities are introduced is from the increasing chemical potential of the impurity. Since line tension γ is approximately equal to stiffness Γ in these systems,[112] with ΔN_i the excess number of large particle per boundary length in our case (ρ_{gb}, in units of ${\sigma_h}^{-1}$), Eq. (3.2.11) can thus be rewritten as:

$$-d\Gamma = \rho_{gb} d\mu_{gb} \tag{3.2.12}$$

ρ_{gb} can be related to the impurity fugacity f_{imp} empirically by the function (Figure 3b and d):

$$\rho_{gb} = \frac{A f_{imp}}{1 + B f_{imp}} \tag{3.2.13}$$

where A and B are two constants. In conjunction with $f = \exp(\beta\mu)$, Eq. (3.2.12) can be written as:

$$-d\Gamma = \frac{A}{\beta(A-B)\rho_{gb}} d\rho_{gb} \tag{3.2.14}$$

Integrating Eq. (3.2.14):

$$\Delta\Gamma = \frac{A}{\beta B} \ln\left(1 - \frac{B}{A}\rho_{gb}\right) \tag{3.2.15}$$

When the impurities at the grain boundary are dilute enough to be effectively non-interacting, the B term of Eq. (3.2.13) can be neglected and the GB excess ρ_{gb} scales linearly with f_{imp}:

$$\rho_{gb} = A f_{imp} \tag{3.2.16}$$

Therefore:

$$-d\Gamma = \rho_{gb} d\mu_{imp} = d\rho_{gb} \tag{3.2.17}$$

$$\Delta\Gamma = -\rho_{gb} \tag{3.2.18}$$

Note the stiffness depression is only related to ρ_{gb} in this limit.

3.2.6 Implementation details

Reduced units, scaled to the host particle diameter σ_h and the thermal energy $k_B T$ are used throughout. The Gibbs excess number per unit length of the GB (ρ_{gb}) is obtained by subtracting the expected total mean content of a bulk simulation box ($\rho_{bulk} \times A$) from the actual mean number of particles in the box containing the grain boundaries and dividing by the total length of the grain boundaries. We use this definition (which would be impractical to implement in a polycrystalline system) rather than a local area concentration within some defined zone near the interface (as was used in recent experiments[40]) because it provides an un-biased basis for comparing adsorbates of

different size without having to define the width of the interfacial zone. Furthermore it is directly related to interface thermodynamics via the Gibbs adsorption isotherm.

Mixtures with size ratio $\lambda = 0.5$, 0.75, 1.2, 1.4, 2.0, 2.25, 3.0 and 4.0 are investigated. In comparing with additive HD mixtures, the corresponding effective in-plane size ratios ($\lambda' = 2\sqrt{\lambda} - 1$) are then 0.41, 0.73, 1.19, 1.37, 1.83, 2.0, 2.46 and 3.0, respectively. In the following, the size ratio λ refers to the real size ratio, not the effective one (λ'). MRMC was used for λ = 0.5, 0.75, 1.2 and 1.4 cases, while regular SRMC for larger size ratios.

Sampling was performed in parallel using a standard domain decomposition scheme. The system (with a box size $200\sigma_h \times 200\sigma_h$) was divided into an 8×8 or 12×12 grid with a randomly selected origin. A cycle of 2000 SRMC/MRMC move attempts (1000 each for small particle only SRMC and either small-big particle exchange or MRMC) followed by 2000 regular translation move attempts (max. displacement of $0.05\sigma_h$) is carried out on separate processor in each grid square, freezing a zone of width $\lambda\sigma_h$ between borders during the cycle. After each MC cycle, the grid is displaced to a new randomly chosen center. Equilibration and production periods consisted of at least 5000 and 20000 MC cycles, respectively. At sufficiently high f_{imp}, the region of disorder and enrichment of impurities were observed to expand to dimensions comparable to the box size, indicating that a melting transition had been either approached closely or crossed. Such systems were not included in the present data analysis.

In the study of grain coarsening in comparison with experimental results, we first randomly insert 40 (30) impurities with λ=2.25 (4.0) in an empty simulation box with a size $200\sigma_h \times 200\sigma_h$, and then run SRMC on small particles only at fugacity $f_h = 1.0 \times 10^7$ to insert host particles. After 2000 MC cycles, a polycrystalline phase can be obtained. Then the simulation is switched to regular translational MC moves (on both host and impurity particles) in NVT ensemble to resemble

the dynamical process of grain coarsening. The frames after at least 50000 MC cycles are used for partitioning analysis.

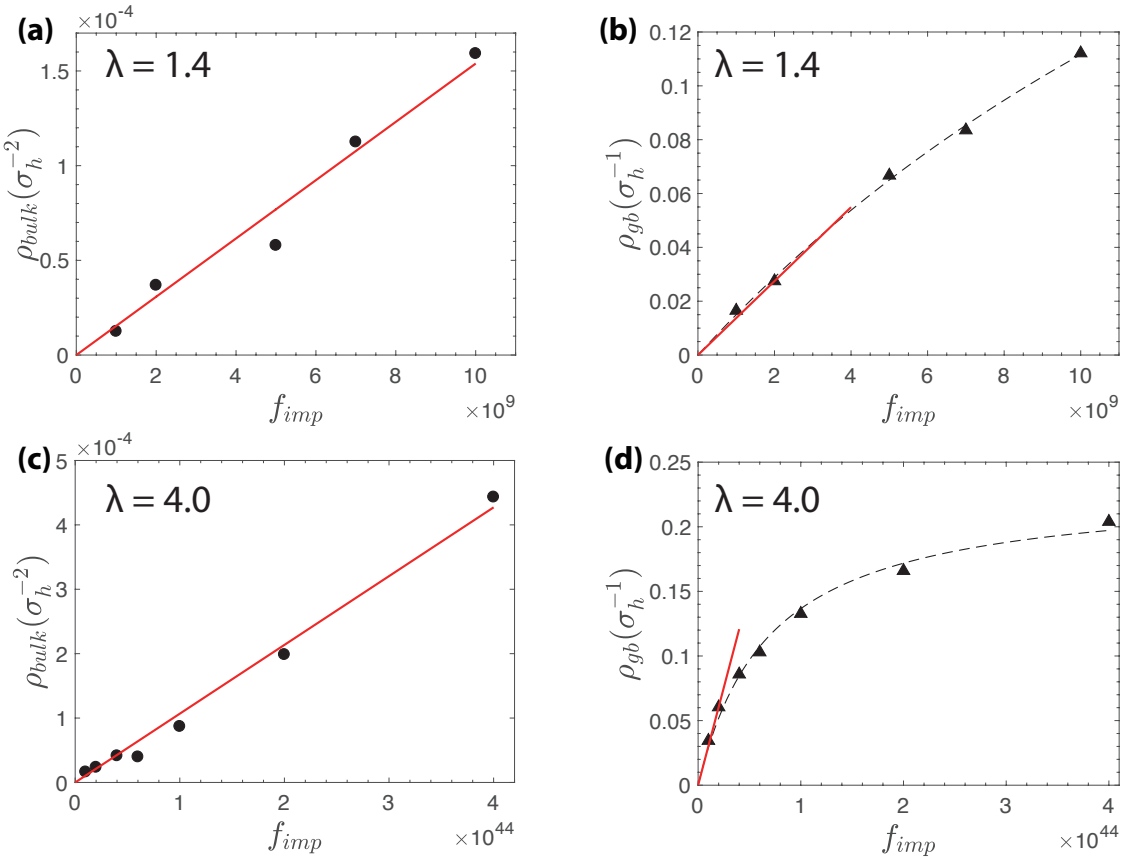

Fig. 3.3 Dependence of impurity concentration on its fugacity for system (a) $\lambda = 1.4$, in bulk; (b) $\lambda = 1.4$, in GB; (c) $\lambda = 4.0$, in bulk; (d) $\lambda = 4.0$, in GB. The misorientation and inclination for all systems are fixed at 30° and 15°, respectively. The fugacity of host particles is fixed at 1.0×10^7 (corresponding to area fraction 0.734). Red solid lines are linear fits to the data (only fitting dilute regime for ρ_{gb}). Black solid lines are non-linear fitting of ρ_{gb} by Eq. (3.2.13).

3.3 Results and Discussion

We will first demonstrate GB segregation of impurities of different size in grand canonical simulations of mixed hard spheres, and will illustrate the reduction in GB stiffness due to this segregation. The second section of this chapter will discuss comparisons between the current results and the experimental findings of Lavergne *et al.*[40] Discussion of the dependence of segregation on grain misorientation and GB inclination will also be presented.

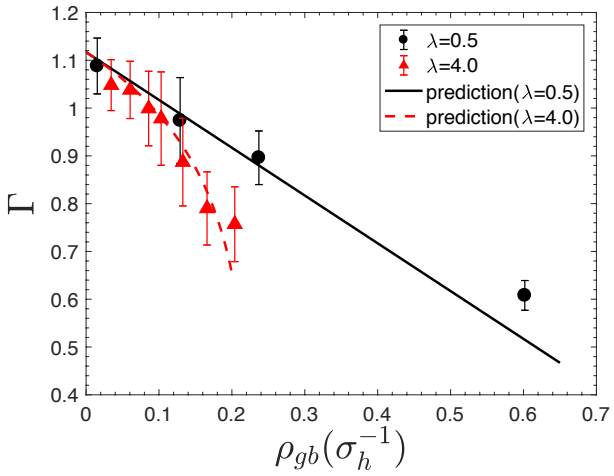

Fig. 3.4 Comparison between stiffness Γ obtained from simulations for $\lambda = 0.5$ (black circle) and $\lambda = 4.0$ (red triangle) with Γ calculated from the Gibbs adsorption isotherm for $\lambda = 0.5$ (black solid line with slope -1) and $\lambda = 4.0$ (red dash line). Simulations are performed in systems with a fixed GB misorientation of 30° and inclination of 15°.

3.3.1 GB segregation and Stiffness depression

We first studied the GB segregation of impurity particles with different sizes in domains with a fixed host particle fugacity f_h (1.0×10^7), misorientation (30°) and inclination (15°). The area fraction of the host particles in the pure bulk solid[112] at this fugacity is 0.761. The qualitative tendency of impurity particles to segregate towards the GB was apparent from viewing trajectories. The number density of impurity particles under dilute conditions can be fitted by a linear relation:

$$\rho_{gb} = k_{gb} f_{imp} \tag{3.3.1}$$

$$\rho_{bulk} = k_{bulk} f_{imp} \tag{3.3.2}$$

where k_{gb} and k_{bulk} are two constants; f_{imp} is the fugacity of impurity; ρ_{gb} is the excess number of interfacial impurity particles per unit length of GB (in units of ${\sigma_h}^{-1}$, which can be directly applied to Gibbs adsorption isotherm discussed in Eq. (3.2.15) and (3.2.18)) and ρ_{bulk} is the impurity particle number in bulk per unit area (in units of ${\sigma_h}^{-2}$). The k_{bulk} is fitted by using all the data obtained at various f_{imp}. Impurity concentrations in the bulk remain below 1×10^{-3},

where interactions between impurities can be assumed to be minor. Within this range, surface pressure is expected to vary only slightly with impurity concentration at fixed host particle fugacity. Specifically, the presence of the impurities should add ρ_{bulk} (in reduced units) to the pressure of the pure host solid at this fugacity. We confirmed in several cases that surface pressure of all systems was within the uncertainty range 12.15±0.23 determined previously[112] for the pure host solid at f_h=1.0 × 10^7. In contrast, the non-linear dependence of ρ_{gb} on f_{imp} (Fig. 3.3) (reflecting direct or indirect interactions among impurities at the GB) is an important consideration in the systems studied, becoming more significant as impurity size increases. This is because the large size impurities will occupy more area in the GB, leading to excluded-volume interactions at lower number densities. Eq. (3.2.13) was used to fit this non-linear dependence.

The level of impurities, and the extent of inter-impurity interactions, both have a significant effect on the GB stiffness. The effects of the smallest (λ=0.5) and largest (λ=4.0) impurities on the line tension assessed using CFM are shown in Fig. 3.4. Evidence from previous simulations[112] has shown that for these HS monolayer systems, stiffness is insensitive to GB inclination, which allows us to equate stiffness with line tension. Under this assumption, knowing the dependence of ρ_{gb} on impurity fugacity f_{imp} allows use of the Gibbs adsorption isotherm to predict how stiffness will be lowered in the presence of impurities by using Eq. (3.2.15) or Eq. (3.2.18). Here we check these predictions against stiffness calculated from GB fluctuations via the CFM.

The impurities can stabilize the GB, which decreases the GB stiffness significantly compared to the pure system with a stiffness Γ= 1.12 (Fig. 3.4). For smaller size impurities, in the density regime where impurities at the GB do not interact significantly, a simple line with slope -1 and *y*-intercept at the pure system stiffness (Fig. 3.4, black line; derived from Eq. (3.2.18)) gives a good fit to the stiffness depression. The physical origin of the linear "ideal" contribution to the reduced

line tension is that a decrease in GB length reduces the translational entropy available to each impurity from moving along the GB. Therefore, a kind of 1-dimensional osmotic line pressure works against the intrinsic line tension. For the largest particles, the non-ideality needs to be considered in the prediction by employing Eq. (3.2.15), which incorporates the fitting parameters to the non-linear dependence of ρ_{gb} on impurity fugacity f_{imp} (Fig. 3.4, red curve). Curves obtained at other impurity sizes (not shown) were distributed between these limits, with larger impurities showing greater deviation from linearity. The deviation from linearity for large impurities at high ρ_{gb} comes from an additional line pressure due to crowding. The agreement between the calculated and predicted stiffnesses serves as evidence for the overall thermodynamic self-consistency of these calculations.

It bears noting that the fluctuations sampled by SRMC and MRMC algorithms include changes to the total number of particles and so in principle may sample over a greater ensemble of structures, and with different dynamics, than would simulations involving local moves only. Along these same lines, the topology of the defect structure within the host lattice upon addition of impurities can relax here in ways that may not be accessible when an impurity is introduced to an existing structure when the number of host particles is fixed.

Table 3.1 Segregation of impurity with different sizes. In all cases, the fugacity of host particles is fixed at 1.0×10^7 while misorientation and inclination of GB are fixed at 30° and 15°, respectively.

λ	k_{bulk} (σ_h^{-2})	k_{gb} (σ_h^{-1})	k_{gb}/k_{bulk} (σ_h)
0.5	3.154×10^{-4}	3.198×10^{-2}	1.014×10^{2}
0.75	3.996×10^{-6}	2.087×10^{-4}	5.223×10^{1}
1.2	1.476×10^{-10}	1.894×10^{-9}	1.283×10^{1}

1.4	1.539×10^{-14}	1.373×10^{-11}	8.923×10^{2}
2.0	1.187×10^{-22}	3.410×10^{-19}	2.872×10^{3}
2.25	5.384×10^{-26}	1.819×10^{-22}	3.379×10^{3}
3.0	6.084×10^{-36}	2.639×10^{-32}	4.338×10^{3}
4.0	1.185×10^{-48}	3.019×10^{-45}	2.551×10^{3}

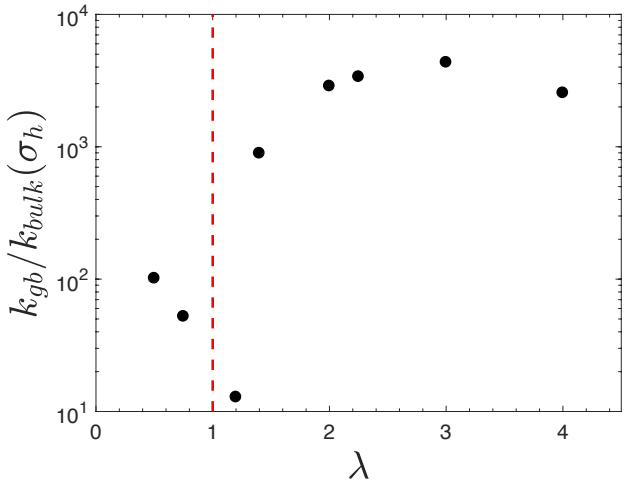

Fig. 3.5 Affinity for grain boundary k_{gb}/k_{bulk} for different impurity: host size ratio λ. Red dash line marks the one-component system ($\lambda = 1$). The misorientation and inclination for all systems are fixed at 30° and 15°, respectively. The fugacity of host particles is fixed at 1.0×10^{7}.

For a measure of the tendency towards segregation for impurity particles interacting only with host particles and not with each other, we calculated the ratio k_{gb}/k_{bulk}, with k_{gb} derived only using data in the dilute regime ($\rho_{gb} < 0.05$). The two factors k_{gb} and k_{bulk} for systems with different size impurities are listed in Table 3.1. Their ratio k_{gb}/k_{bulk}, a measure of the tendency of impurities to segregate towards GB, is plotted against impurity size λ in Fig. 3.5. As λ increases from 1 to 3.0 (or decreases from 1 to 0.5), the k_{gb}/k_{bulk} increases since the larger size mismatch

will cause more distortion of neighboring host particles in the bulk, which encourages the impurity to stay in the GB. One special case is size ratio 4.0, where k_{gb}/k_{bulk} is lower compared to λ=3.0.

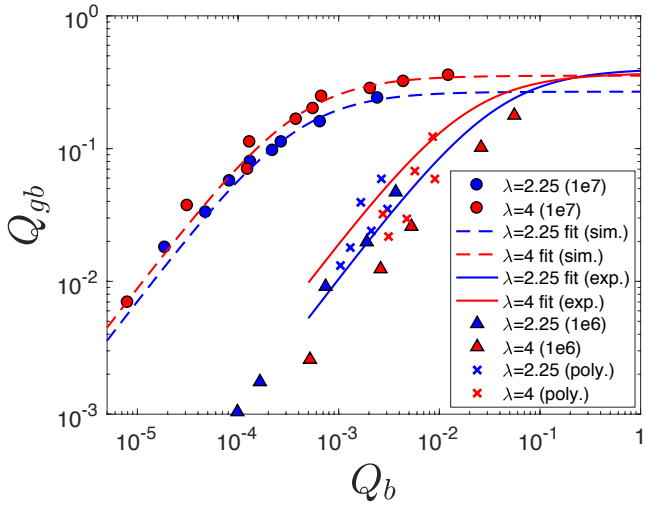

Fig. 3.6 Composition variables Q_b and Q_{gb} for size ratio $\lambda = 2.25$ and $\lambda = 4.0$ in simulation at fugacity f_h=1.0 × 10^7 (corresponding area fraction 0.761) and 1.0 × 10^6 (corresponding area fraction 0.734). Dash lines and solid lines indicate the fit to the Langmuir-McLean isotherm in simulation and experiment (reference [40]), respectively.

The special nature of this size ratio was discussed in a recent experimental study by Lavergne *et al.*[40], who pointed out that the impurity with λ=4.0 can perfectly replace seven small host particles in a "substitutional" position within a hexagonal lattice without producing long-ranged stress in the lattice. The same effect was invoked in a simulation study of the fluid/ordered phase segregation of impurities in hard disc mixtures, where impurities with diameter d=3.0 were more soluble in the ordered phase of d=1 host discs than were impurities of diameter d=1.4 or d=2.5.[8]

Table 3.2 Fitting parameters of Langmuir-McLean isotherm in simulation (fugacity f_h=1.0 × 10^7) and experiment (reference [40]). The free energy of adsorption is determined from the isotherm via $e_a/k_BT = \ln(K)$.

λ	Q_{gb}^{sat}	K	e_a/k_BT
2.26 (experiment)	0.40	26.76	3.29
2.25 (simulation)	0.27	2701	7.90

4.0 (experiment)	0.37	54.33	4.00
4.0 (simulation)	0.35	2595	7.86

3.3.2 Comparison with experimental results

Lavergne *et al.*[40] performed experiments on binary colloidal mixtures at λ=2.26 and 4.0, monitoring the distribution of large particles in bulk and GB environments of a polycrystalline sample. Over time their systems reached a stable partitioning, which over many experiments could be represented using the equilibrium Langmuir-McLean isotherm. To compare our results with this experimental study, we first re-analyzed the simulated segregation behavior in terms of the area fractions Q_b and Q_{gb} of impurity particles in bulk and GB environments.

$$Q_b = \frac{\lambda'^2 N_{imp}^b}{N_h^b + \lambda'^2 N_{imp}^b} \tag{3.3.3}$$

$$Q_{gb} = \frac{\lambda'^2 N_{imp}^{gb}}{N_h^{gb} + \lambda'^2 N_{imp}^{gb}} \tag{3.3.4}$$

where $\lambda'$is the effective in-plane size ratio; $N_h^b(N_h^{gb})$ is the number of host particles in the bulk (GB) and $N_{imp}^b(N_{imp}^{gb})$ is the number of impurities in the bulk (GB). Identification of bulk and GB environments followed the definitions in reference [[40]]. Q_b and Q_{gb} obtained in our simulations are shown in Fig. 3.6, along with the fit to the Langmuir-McLean isotherm rewritten in terms of Q_b and Q_{gb}:

$$Q_{gb} = Q_{gb}^{sat} \frac{KQ_b}{1+KQ_b} \tag{3.3.5}$$

where GB composition at saturation, Q_{gb}^{sat}, and the equilibrium constant, K, are two fitting parameters. The values of Q_{gb}^{sat} and K in simulation and experiment[40] are given in Table 3.2.

The impurity segregation data presented above, when recast in terms of partitioning between areas rather than partitioning from a 2-d environment to a 1-d interface, could be fit with the same Langmuir-McLean form as the experimental data (Fig. 3.6, circles and dashed curves). There are several interesting discrepancies. First, for a given Q_b, the Q_{gb} in our initial set of simulations is at least an order of magnitude higher than experiment (Fig. 3.6), when Q_b is smaller than the saturation point. Some portion of this difference can be explained by the use of GB with the highest possible (30°) misorientation in the simulations used to calculate Q_{gb}, which (as discussed below) yields greater partitioning of impurities to GB than low-misorientation GB. The polycrystalline structures in experiment will have a range of misorientation angles which, in the absence of impurities at least, is skewed towards low misorientations at long times[24], and in any case will average lower than the maximum misorientation of 30°. As discussed below, however, with the exception of $\lambda = 4$ impurities at low concentrations, reducing misorientation angle would not produce a 10-fold variation in degree of segregation.

The second possibility considered was that the effective pressure of the system was different in simulation and experiment, and that at lower pressures the drive toward segregation is not expected to be as strong. Simulations were repeated at a lower fugacity f_h=1.0×10^6 (corresponding to area fraction 0.734), where the lateral pressure was previously measured at 10.01 ±0.18 and the GB stiffness at Γ= 0.47 is less than half its value at f_h=1.0×10^7.[112] The tendency of impurities to segregate to GB is much reduced at this lower pressure condition (Fig. 3.6, triangles), giving general agreement with experiment (Fig. 3.6, solid curves). It is therefore very plausible that the experiments show weaker segregation because the lateral pressure was weaker than in the original simulations; unfortunately, as discussed in previous work,[112] direct comparison of system conditions between these simulations and experiments is complicated.

We lastly considered the possibility that the Q_{gb}/Q_b ratio observed in experiment does not reflect equilibrium statistics. The experimental evidence in support of the impurities' equilibrium partitioning is that the observed stable distribution is consistent with the equilibrium Langmuir-McLean isotherm model. The large impurity particles, embedded in a dense matrix of host particles, are very limited in their mobility as evident from Movie S1 in reference [40], so the system evolves to a state with a given Q_{gb}/Q_b ratio primarily through motion of the grain boundaries themselves. The free energy change associated with a GB moving toward or away from an impurity (the latter phenomenon called "depinning") is a combination of the free energy of exchanging the impurity between bulk and GB environments and the change in interfacial free energy from changing the GB length. As grains coarsen, it is possible that the free energy benefit from reducing GB lengths associated with depinning could drive the impurity partitioning away from equilibrium. To test this possibility, we set up polycrystalline systems with fixed number of host and impurity particles and performed regular translational MC moves only to resemble the experimental conditions. We observed the smaller domains with different orientations eventually merging to several bigger domains, behavior similar to Movie S1 in reference [40], leaving many impurity particles in the bulk (not shown). The corresponding Q_b and Q_{gb} in these NVT ensemble simulations are indicated as cross markers in Fig. 3.6 and lie within the scatter of experimental points presented in reference [40]. Therefore, the discrepancy between the simulation and experiment could also come from non-equilibrium effects in the experimental system (which does not benefit from an infinite virtual reservoir that can exchange impurities for host particles anywhere in the system). Whether it is possible for non-equilibrium dynamics to produce an apparent equilibrium result (the Langmuir-McLean isotherm) in this type of system is an interesting question for future study.

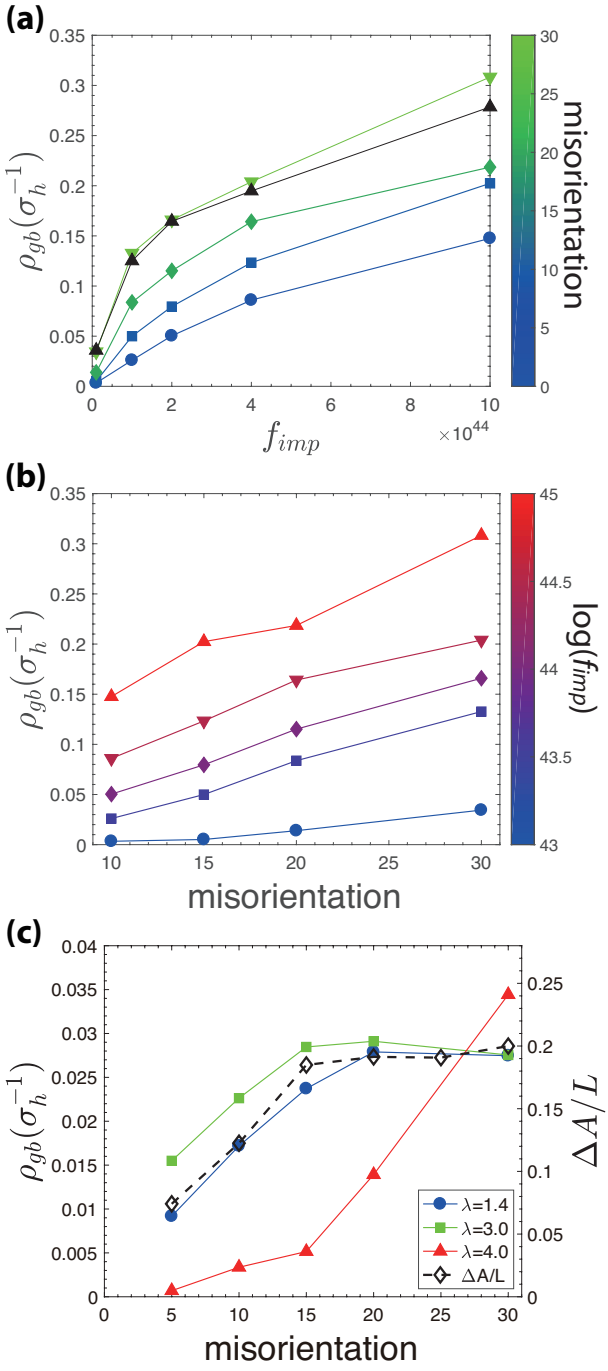

Fig. 3.7 (a) ρ_{gb}- f_{imp} plot for different misorientations and inclinations at different fugacity for $\lambda = 4.0$: (blue-green color bar represents different misorientation with fixed inclination 15°; the black up-triangular label represents the inclination 0° with misorientation 30°); (b) ρ_{gb}-misorientation plot on the same dataset as in (a); (c) Dependence of ρ_{gb} on misorientation for $\lambda = 1.4$ with $f_{imp} = 2.0 \times 10^{9}$, $\lambda = 3.0$ with $f_{imp} = 1.0 \times 10^{30}$ and $\lambda = 4.0$ with $f_{imp} = 1.0 \times 10^{43}$, in dilute regime. Black diamond points show the free area change for one-component system (reprint from reference [112]). The fugacity of host particles is fixed at 1.0×10^{7} for all cases. Lines are drawn only to guide the eyes.

In the previous section the distinctive behavior of λ =4.0 impurities was noted and attributed to their ability to pack into a hexagonal lattice substitutionally. The size λ =2.25 impurities were similarly identified as special case that can substitute interstitially for 3 host particles in the lattice;[40] experiments showed lower propensity for GB segregation by these interstitial particles than by the substitutional particles. In the simulations, the data do not provide a clear, consistent answer to which size impurity has greater affinity for the GB. Under the higher pressure conditions, k_{gb}/k_{bulk} is higher for λ =2.25 but Q_{gb}/Q_b is higher for λ =4. At lower pressure, the different metrics are still in disagreement, but each favors a different size than at high pressure. It may be more instructive, rather than to focus on the comparison between these two particular sizes, instead to look back at the trends in Fig. 3.5. These suggest that the GB segregation tendencies at the two sizes are similar, but that λ =2.25 follows the general trend of increase in degree of segregation with increasing impurity size while λ =4 is an exception to that trend. The simulation results therefore suggest that unlike the case of λ =4, the possibility of perfect matching for interstitial substitution at λ =2.25 does not produce any remarkable effect on the tendency to segregate to the GB in comparison with larger and smaller size impurities.

3.3.3 Dependence of segregation on GB orientation

In a previous study,[112] we have shown that GB stiffness and excess area per unit length ($\Delta A/L$) are sensitive to misorientation of grains, but insensitive to GB inclination, a result supported (indirectly) by experimental observations of the evolution of the distribution of GB angles.[24] Fig. 3.7(a) and (b) show the dependence of GB segregation on the orientation of GB for impurities with size ratio λ = 4. The general trends in impurity segregation follow the trends observed for stiffness and excess area: the degree of segregation increases with greater misorientation but, in the cases

tested, shows little dependence on inclination. A closer look at the dependence of degree of segregation on GB orientation at different size ratios in the dilute regime shows some unexpected behavior. In Fig. 3.7(c), the misorientation dependence of the degree of segregation for λ=1.4 and λ=3.0 appears to correlate with the misorientation-dependent excess area of the GB ($\Delta A/L$) obtained in the absence of impurities (which also correlated strongly with the stiffness, not shown).[112] However, GB segregation for λ=4.0 shows a much more dramatic decrease with decreasing misorientation than does the excess area: GB with misorientation of 10° contain a factor of 10 lower levels of λ=4.0 impurities than do GB with misorientation 30° at the same fugacity (*i.e.,* at equilibrium with the same bulk composition). One implication is that, if GB with misorientation < 30° had been used to generate Fig. 3.5, the λ=4.0 point would have been even more strongly anomalous.

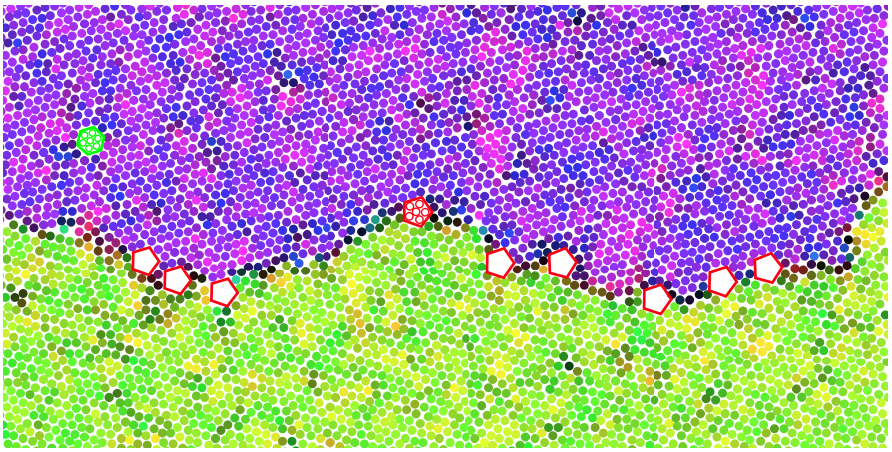

Fig. 3.8 Snapshot of GB in a system for $\lambda = 4$ with $f_h = 1.0 \times 10^7$and $f_{imp} = 1.0 \times 10^{43}$. The orientation of host particle is color-coded as shown in Fig. 3.1. The impurity particles are omitted for clarity, but their locations can be seen as large voids. The green hexagon indicates an impurity site in the bulk that could be substituted for 7 host particles, while the red pentagons indicate impurity sites that could be substituted for 6 host particles.

An explanation for this qualitative difference in behavior can be found by considering both the special substitutional nature of λ=4.0 impurities in the bulk and the misorientation-dependent structure of the interface. Moving an isolated impurity to the GB influences system free energy in two ways: removing local stress in the bulk associated with the impurity, and allowing the host

particles in less-efficiently packed GB sites to move to sites in the bulk where they will occupy less area. The λ=4.0 impurity can substitute efficiently within a defect-free hexagonal lattice, displacing 7 host particles, so the first contribution is small for this size impurity. Therefore, to first order (neglecting more complex rearrangements and relaxation), we expect migration to the GB for a λ=4.0 impurity to be favorable only if it can be inserted in exchange for a set of fewer than 7 host particles. (The effect on the free energy will be approximately neutral if the impurity moves from the bulk to a site of similar size and symmetry near the GB.) If the impurity can occupy a position at the GB where otherwise only 6 host particles could fit, the process of making this exchange (and filling in the 7th site in the bulk vacancy left by the impurity) would reduce the system's area at constant pressure by the area of lattice site. A λ=4.0 impurity can readily substitute for an array of 6 host particles composed of a central particle and five near neighbors, *e.g.* part of the pentagon-heptagon structure that is the endpoint of a dislocation defect. Fig. 3.8 shows a snapshot from an actual simulated GB where the approximate pentagonal symmetry of the cavities occupied by λ=4.0 impurities at the GB can be noted, along with the hexagonal symmetry of one bulk impurity site.

Can the affinity of λ=4.0 impurities for GB with different misorientations be correlated with their occurrence of such sites, which in various models of GB structure[113] might be associated with dislocation origins, coincidence lattice sites, or steps? According to the Read-Shockley model of GB[114] (which is applicable only up to misorientations of $\theta \approx 15°$) the linear density of dislocations at misorientation θ and inclination $\theta/2$ is proportional to $\sin^2(\theta/2) + \sin(\theta/2)\cos(\theta/2)$, a function that increases roughly linearly with θ and so does not describe the observed nonlinear dependence of partitioning on θ seen in Fig. 3.7(c). A step model[113] for such a GB will have points of close contact with density ~tan (θ/2), which is also almost linear in θ. To visualize how

the spacing and nature of potential 5-coordinate substitution sites depends on θ, we generated unreconstructed GB separating hexagonal arrays at three misorientations by overlaying perfect arrays and deleting overlapping host particles. The translational offset for each bicrystal was chosen so that the two lattices would coincide on at least one host particle position that could be the center of a 5-coordinate site for substitution by a λ=4.0 impurities. These structures are shown in Fig. 3.9. At 30° misorientation, a dense and efficient packing is achieved in this idealized structure. At θ = 20° and 10°, not only are there fewer 5-coordinate sites, but the overall packing efficiency in the presence of the impurities is increasingly worse at lower angles; the area that is empty, because it is excluded to both host and impurity particles, is greater. The combination of falling 5-coordinate site density at the GB and the lower efficiency of the packing arrangements produced by impurity substitution could account for the non-linear drop in segregation with decreasing misorientation angle. The excess free area that is not directly associated with the 5-coordinate sites promotes segregation of impurities with λ=3.0 and λ=1.4, because segregation of the smaller impurities can relieve local packing inefficiencies wherever they may occur within the disordered structure at the GB while relieving stress in the bulk. In contrast, the λ=4.0 impurity can improve the global packing primarily by substituting for an entire 5-coordinate site.

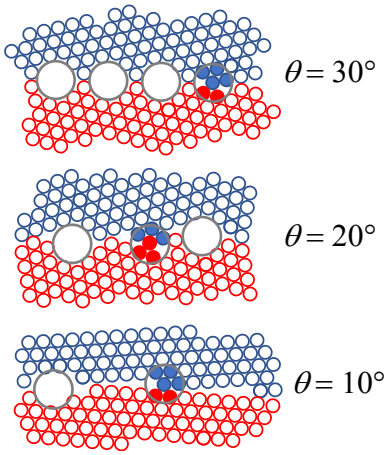

Fig. 3.9 Examples of unreconstructed hexagonal bicrystals with grain boundaries of varying misorientation θ. Large circles represent sites where λ =4 impurities can substitute for 6 host particles (examples shown as filled circles) with approximate pentagonal symmetry.

3.4 Conclusions

Grain boundaries in 2-d hard sphere or hard disc systems are zones of excess area and disorder, and so tend to draw impurities that might pack more efficiently in these disordered environments than in the bulk. It has been appreciated[8, 40] that impurities of just the right size (with effective diameter 3 times that of the host particles, here meaning λ =4) are accommodated more efficiently in the bulk than others of greater or lesser size. We have seen here that impurities of this size are distinctive not only for partitioning less strongly to the GB than smaller impurities, but also for their misorientation angle dependence. The apparent reason is that these impurities can reduce the overall free area of the system by migrating from the bulk to sites with approximate 5-fold symmetry associated with dislocations at the GB. Free area associated with other structures, therefore, does not enhance the affinity of λ =4 impurities for the GB, leading to a qualitatively different distribution across GB of different misorientations than observed at other impurity sizes.

The solvent repacking Monte Carlo algorithm enabled the exchange of impurities between bulk and GB to equilibrate even though the impurities were effectively unable to move through the bulk. Further investigations, using sampling methods that approximate realistic dynamics, will be

useful to determine under what conditions equilibrium segregation can be achieved and whether non-equilibrium distributions arising during grain coarsening dynamics can produce the Langmuir-McLean distribution reported in experiments on mixed colloids.[40]

Chapter 4

Dynamics of Grain Boundary Loops in 2-d Solid Hard Sphere Monolayers

In this chapter, we investigated the dynamics of a special geometry of Grain Boundaries (GBs): the GB loop. We systematically studied how pressure, size, original misorientation and method of preparation affects the relaxation of the GB loop in a 2-d solid Hard Sphere (HS) monolayer. We found that at low pressure, the rate of shrinkage is controlled by the driving force (line tension) that will bias the very mobile GB towards reducing the overall perimeter of the included. At higher pressure, however, the dynamics of GB shrinkage depends more on the details of defect arrangement. Our simulation results are broadly consistent with the experimental observations of Lavergne *et al*. at high pressure with small loop size, but do not show the same common dependence on $R_0\ \theta_0$ reported in experiment at higher loop size R=10.

4.1 Introduction

Polycrystalline patterns can be widely observed in many systems including crystalline solids,[33] colloidal particles,[48, 49] di-block copolymers[50] and nonequilibrium dissipative structures.[51] The smaller grains are eliminated through coarsening as the system evolves. The grain coarsening has been studied in order to engineer the polycrystalline materials,[52] and to better understand the nonequilibrium ordering phenomenon.[53]

The dynamics of grain coarsening, characterized by the mobility M, can be affected by many factors, like system pressure, misorientation between GBs, and the presence of impurity. In

experiment, the dynamics of one special type of boundary, the GB loop, has been studied in several works.[53-56] In the study of GB loop in colloidal particle, Lavergne *et al.* found the formation and kinetics of GB is related to topological constrains in their complex dislocation structure.[54] They also demonstrate the dependence of deformation (either elastic or plastic) on misorientation angle.

MD simulation has been used in study of GB migration and grain rotation.[55, 56] Z. T. Trautt *et al.* simulated the isolated cylindrical grain in copper, where they found the dynamics of GB motion and grain rotation is affected by initial misorientation angle and temperature. They also employed the dislocation mechanisms to explain the motion of curved GBs.[55] Another MD work by M. Upmanyu *et al.* shows the GB migration and grain rotation can occur simultaneously, where they observed the grain rotated as a rigid body motion rather than by grain shearing by dislocation passage through the grain interior.[56]

In this work, we used MC to simulate the dynamics of GB. Although Monte Carlo simulation does not produce a trajectory that is directly related to a dynamic algorithm, the evolution of a Monte Carlo trajectory that uses local displacement moves can give qualitative insight into dynamics. This is particularly true for colloidal systems where Brownian dynamics might be a good approximation.[57] Separate dynamic studies in canonical ensemble are used to show how impurity size, concentration and orientations of grains affect the grain growth, through the combined effects of impurities on GB thermodynamics (reduction of line tension) and dynamics (pinning effects).

4.2 Methods

4.2.1 Construction of GB loops by cut-and-paste method

In accordance with our previous simulation of GB loops,[112] the round shape domain (with a radius R_0 and certain orientation angle respected to the x axis) is inserted into the center of the big square domain with a box length L (50σ or 100σ in this work) and a fixed orientation (aligned to the x axis). Any contact particle in the border between the two domains is removed.

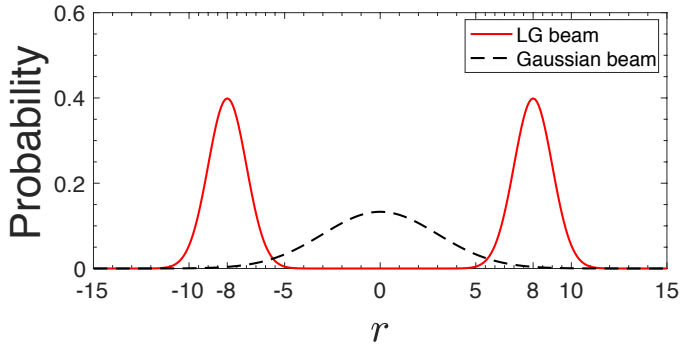

Fig. 4.1 Probability distribution of bias moves mimicking LG beam and Gaussian beam in simulations with $R_0 = 8\sigma$.

4.2.2 Construction of GB loops by tweezer-mimic method

A uniform square domain (with box length L and average 0 orientation respect to the x axis) is used as the initial configuration in the tweezer construction method. Similar to the experiment[54], we aim to transfer a rotational momentum on 2-d HS system. In Monte Carlo simulation, however, we cannot directly apply a force on the particle. Instead, we introduce bias when selecting the directions of random walk. Given a uniformly random selected particle in system, we consider performing a bias move towards the tangent of GB loop with probability P_{bias}, or a regular translational move with equal probability in any direction. The P_{bias} is set to 0.2 in this work, which is tuned for providing relaxation between particles during domain rotation. If the particle is considered for bias move, then the probability of actually making a bias move is P_{mix}, which is a mixed probability of two probability density function P_{LG} and P_G (Fig. 4.1) depending on the distance from the selected particle to the box center r:

$$P_{LG} = \frac{1}{\sqrt{2\pi\sigma_{LG}^2}} \exp\left[-\frac{(|r|-R_0)^2}{2\sigma_{LG}^2}\right] \quad \text{(Xa)}$$

$$P_G = \frac{1}{\sqrt{2\pi\sigma_G^2}} \exp\left(-\frac{r^2}{2\sigma_G^2}\right) \quad \text{(Xb)}$$

The bias probability P_{LG} and P_G resemble the Laguerre-Gaussian (LG) beam and Gaussian beam in experiment, respectively,[54] where the LG beam is the main motivation to drive the particle while Gaussian beam can maintain the round domain intact during rotation. In contrast to the experiment, we found the domain can be intact under various combinations of standard deviation terms σ_{LG} and σ_G (which tune the strength and width of the probability distribution), even there is no Gaussian beam at the center. For the best generalization to most systems, we set σ_{LG}=1.0 and σ_G=3.0 in all our simulations. The overall probability of making a bias move is $P_{bias}P_{mix}$. If selected, the biased move will be an attempt to translate the selected particle to a position along circular path. The random move (bias or regular translational) is rejected if it produces an overlap with another particle.

4.2.3 Order parameter

Bond-orientational order parameter[100] Ψ_6 is used to characterize the local crystalline order of particle j:

$$\Psi_6(\vec{r}_j) = \frac{1}{N_j}\sum_{k=1}^{N_j} e^{i6\Delta\theta_{jk}} \quad (4.2.1)$$

where $\Delta\theta_{jk}$ is defined as the angle between the x direction with the vector connecting the central particle j and one of its N_j nearest neighbor k within a cutoff 1.5σ. The orientation of the hexagon formed by six neighbors of particle j can then be calculated by $\theta_6 = \arg(\Psi_6)/6$, which is a value varied from 0 to 60° due to the symmetry of hexagon. The orientation of the grain domain

can be quantified by averaging all the θ_6 of particles belonging to the domain. In the rest of this report, θ_6 refers to the orientation of the domain instead of single particle for simplicity.

4.2.4 Mobility measurement from Monte Carlo simulation

The shrinking rate of GB loop has a big variance in our simulation. For all mobility measurements, 16 shrinking curves starting from different initial structures constructed under same condition but different random number seeds were averaged to represent the mean shrinking rate (Fig. 4.2). A linear fit was then applied on these mean shrinking rates to extract the expected total shrinkage time t_f (represented by number of MC moves in simulation). The reduced mobility can be calculated as $M^* = A_0/(2\pi t_f)$, where A_0 is the area of the initial round domain with radius R. The outer grain has a fixed orientation θ_6 at 0 degree (aligned with the x axis), the grain inside the GB loop will have a θ_6 ranging from 0 to 30 degree. A particle is classified as one inside GB loop if its orientation angle θ_6 is within $\theta_0 \pm 5°$, where θ_0 is the average orientation angle of the inner grain in the initial configuration. The particle number inside GB loop can then be used to calculate the A_0. It should be aware that the mobility measured from our simulation (in unit of σ^2, the shrinking area per MC move) cannot directly compared with the number in experiment (in unit of σ^2/s), but we can still compare the relative mobility under different construction methods and conditions.

4.2.5 Implementation details

A domain-decomposition scheme is used to parallelize the simulations for system has a big size ($200\sigma_h \times 200\sigma_h$ or $250\sigma_h \times 250\sigma_h$ in dynamic study under the presence of impurity). The simulation box was divided into an 8×8 or 12×12 grid with a randomly selected origin. MC cycles were

performed within each grid square on separate processors, with no addition, removal, or translation particles within a zone of distance of $0.5\sigma_h$ from domain borders. After every MC cycle, a new origin for the grid was chosen and particles are redistributed among processors so that the border regions are constantly changing. Each MC cycle contains 2000 regular translation move attempts (max. displacement of $0.05\sigma_h$) performed in each domain.

4.3 Results and Discussion

4.3.1 Dynamics of GB loop

We first studied if there is any finite size effect in our simulation. We compared results of simulations under three pressures with different system size ($50\,\sigma \times 50\,\sigma$ or $100\,\sigma \times 100\,\sigma$), constructed by two methods (cut-and-paste or tweezer-mimic). Though some variance presented in the mobility in different box size, the general trend between different misorientations remain the same. Therefore, for computational efficiency, all following simulations of GB loop are performed with a box size of $50\sigma \times 50\sigma$, except the case with large round domain ($R_0 = 20\sigma$) constructed by insertion method that require a larger box size ($100\sigma \times 100\sigma$) to prevent any potential finite size effect.

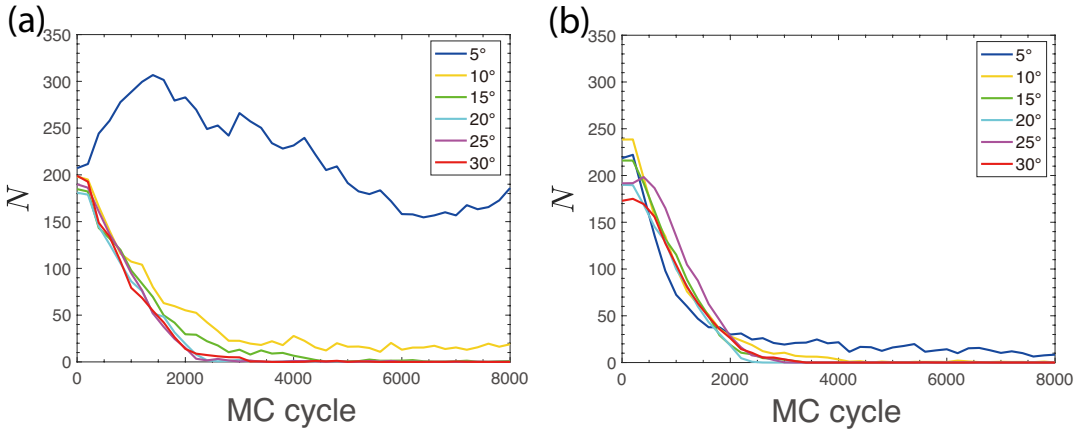

Fig. 4.2 Averaged shrinking curves of system with $R_0 = 8\sigma$ prepared by (a) cut-and-paste method; (b) tweezer-mimic method. All simulations in this plot are performed at bulk area fraction 0.7825. N is the particle number inside GB loop calculated as discussed in *4.2.4*.

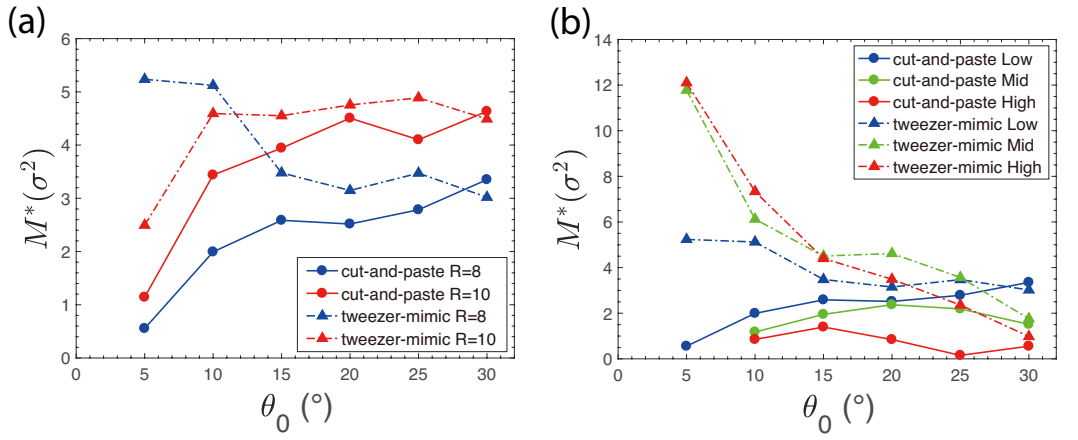

Fig. 4.3 Mobility at different misorientations (a) in systems with a fixed bulk area fraction at 0.7825; (b) in systems with different bulk area fraction 0.7825 (Low), 0.7973 (Mid) and 0.8209 (High), but a fixed R_0 at 8σ.

To make sense of the 25 series of conditions in which we have looked at the misorientation-dependent shrinking of GB loops, we start with the lowest of the three pressure conditions studied here (with a bulk area fraction of 0.7825) which is most similar to the systems whose behavior we reported previously[112] (at a bulk area fraction of 0.7611), where the rate of domain closure appeared to be proportional to the interfacial stiffness. Fig. 4.2 and Fig. 4.3(a) show average results from simulations of GB loops of two sizes prepared according to two protocols: the cut-and-paste method featured in our previous work and the protocol (described above in Methods section *4.2.1*) designed to mimic the torque by the experimental laser tweezer. With one exception, the rate of

loop closure in this regime correlates to the stiffness, and does not depend strongly on the method of preparation. We can explain this regime through a model in which random fluctuations of the GB are relatively facile but are biased in the direction of shrinking the GB loop to reduce its perimeter. The strength of this bias, which is proportional to the line tension, determines the net rate of motion of the interface in the direction of shrinking the loop. The driving force for 5° misorientation is low enough that shrinking is relatively slow. The one exception is that at low misorientation for the smaller loop, preparing the system by rotating a domain rather than by cut-and-paste method allows for faster shrinking of the GB loop. The initial structures that result from these two protocols are distinct, as shown in Fig. 4.4 (a and b). Under these conditions, the rate of GB loop closure for the cut-and-paste structures varied strongly from trajectory to trajectory. Even for a trajectory whose rate of closure was relatively fast, like the one portrayed in Fig. 4.4 (a and c), the mechanism depends on the mode of preparation. Fig. 4.5 (a) shows that the process of domain shrinking for the twisted domain preserves local neighbor identities, consistent with an elastic rotation of the central domain back to its original orientation. In contrast, Fig. 4.5 (b) shows that shrinkage of the cut-and-pasted domain involves plastic rearrangement of the spheres through rearrangements that involve changes to the local neighborhoods of a majority of particles in the domain.

Focusing on the smaller loop size studied, we see from Fig. 4.3 (b) that the sensitivity to the preparation of the misoriented domain is even greater at higher surface pressure, which can be considered analogous to decreased temperature for a thermal system. At the two higher pressures, the simulation matches the experimental trend of diminishing mobility at higher misorientation when the domain is created using the tweezer-mimic method. In contrast, when the domain is created using the cut-and-paste method, the mobility at 5° misorientation and higher pressure is

too low to measure in the current simulations as the loop remains locked in its original configuration.

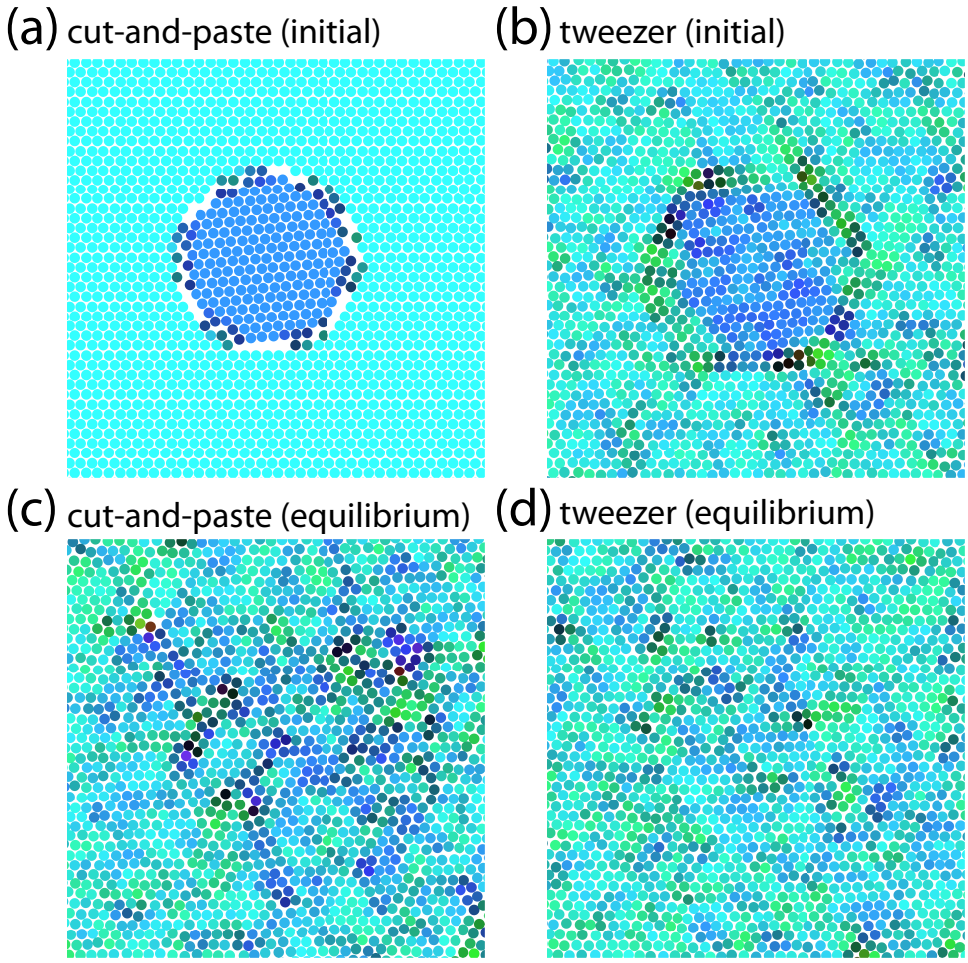

Fig. 4.4 Snapshots of (a) initial configuration prepared by cut-and-paste method; (b) initial configuration prepared by tweezer-mimic method; (c) configuration after 37000 MC cycles of cut-and-paste structure; (d) configuration after 4000 MC cycles of tweezer-mimic method. They all have an initial misorientation $\theta_0 = 5°$, $R_0 = 8\sigma$ and bulk area fraction $\eta = 0.7825$.

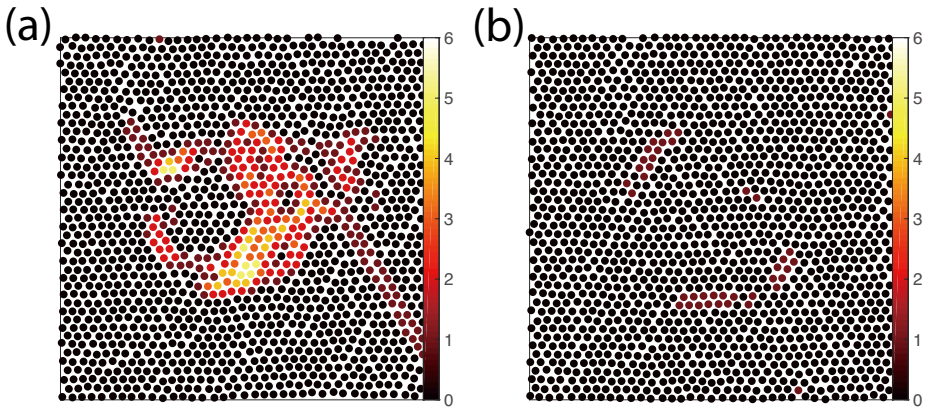

Fig. 4.5 Number of different neighbors between initial and the last configuration for the system (a) prepared by cut-and-paste method; (b) prepared by tweezer-mimic method. They all have an initial misorientation $\theta_0 = 5°$, $R_0 = 8\sigma$ and bulk area fraction $\eta = 0.7825$.

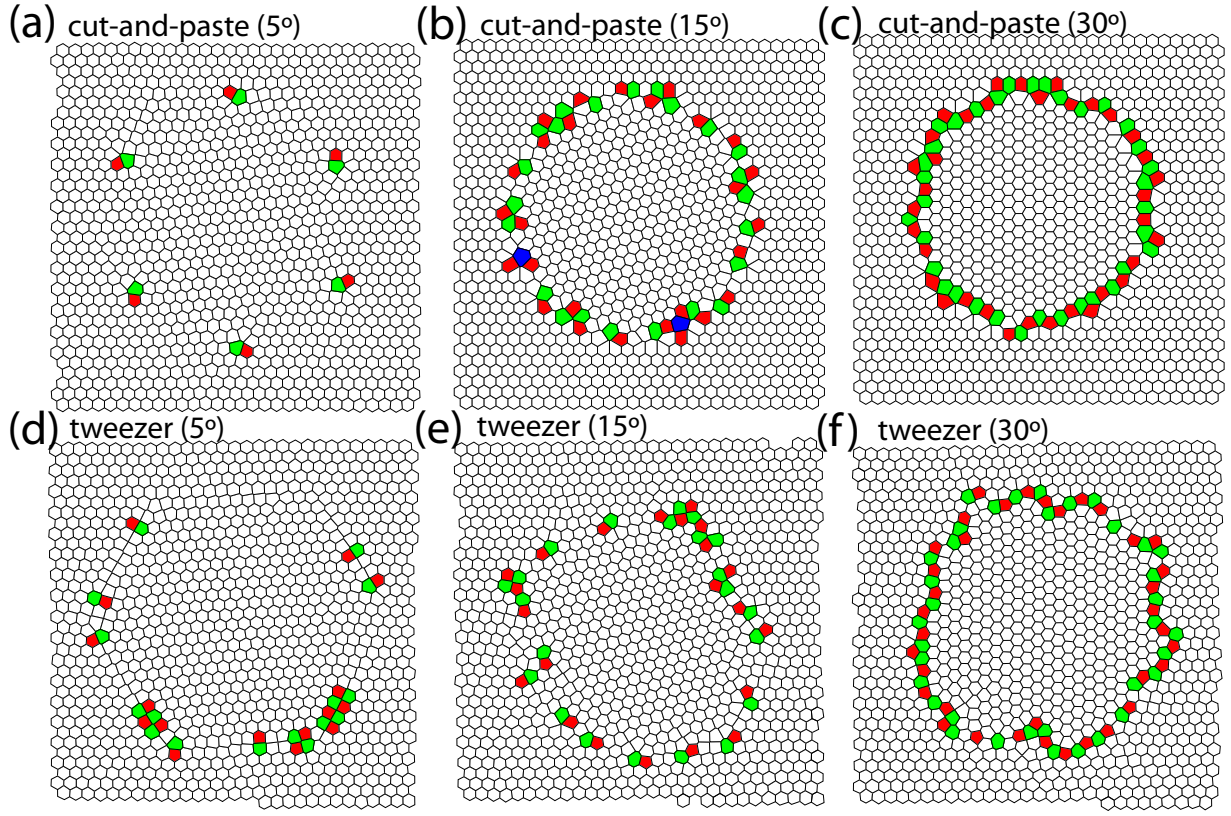

Fig. 4.6 Voronoi graphs of system (a) prepared by cut-and-paste method with misorientation $\theta_0 = 5°$; (b) prepared by cut-and-paste method with misorientation $\theta_0 = 15°$; (c) prepared by cut-and-paste method with misorientation $\theta_0 = 30°$; (d) prepared by tweezer-mimic method with misorientation $\theta_0 = 5°$; (e) prepared by tweezer-mimic method with misorientation $\theta_0 = 15°$; (f) prepared by tweezer-mimic method with misorientation $\theta_0 = 30°$. They all have an $R_0 = 10\sigma$ and bulk area fraction $\eta = 0.8209$. Pentagon cell (green), heptagon (red) and octagon (blue) are color coded, while the remaining cells are hexagon.

4.3.2 Comparison with experimental results

Lavergne *et al.* performed experiments on 2-d colloidal particles constructed by optical tweezer technique.[54] They observed that below a critical misorientation given by $\theta^c \approx \frac{3}{\pi}\frac{\sigma}{R}$, the GB loop will relax via "elastic deformation" through which the domain can rotate as a whole to 0° misorientation instead of shrinking. At higher θ, the loops were found to shrink through combinations of dislocations. The dynamic crossover was shown to originate in a structural transition; at the critical misorientation, the GB loop supports an arrangement of 6 dislocations known as a "flower defect"[115] with a spacing ($\frac{\pi R}{3} = \frac{\sigma}{\theta^c}$) that matches the preferred spacing of dislocations for a GB of that misorientation, and Burgers vectors aligned perpendicular to the GB. At lower misorientation, dislocations may also appear at the GB but they will be oriented with Burgers vectors along the GB, as for a simple sliding offset of a pair rows in a hexagonal array. The contrast between these two cases is illustrated nicely in structures shown in Fig. 6a (generated through the cut-and-paste method and resembling the "flower defect") and 6d (generated through the "tweezer-mimic" method and showing displaced rows at the GB). As both structures were formed with the same original dimension of GB loop (R_0=10.0) and misorientation $\theta_0 = 5°$, slightly below the nominal $\theta^c = 5.47°$, the "flower defect" structure stands in apparent contradiction to the line of reasoning presented above. The misorientation should be too small or the loop should too large to support the "flower defect" structure.

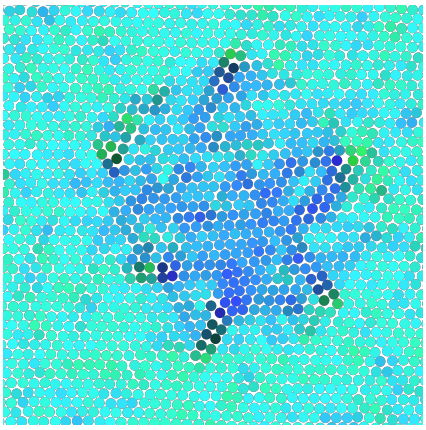

Fig. 4.7 Snapshot of the GB loop with $\theta_0 = 5°$, $R_0 = 10\sigma$ at high pressure (bulk area fraction 0.8209).

What is the "loophole" that permits this loop to exist? Inspection shows that it is qualitatively different from the "flower defect" structure presented by Lavergne *et al*., (Ref. [54] Fig. 3B) in that the dislocations found in our simulations have Burgers vectors that are not directed into the center of the loop but are rotated by 30°. The result is a grain that somewhat resembles a 6-sided star (Fig. 4.7) rather than a compact hexagon. The GB between the defects is not the simple straight boundary on which the preferred spacing of $\frac{\sigma}{\theta}$ is based, and so the structure supports an arrangement of six dislocations even when they are closer to each other than would be stable for a regular hexagon.

The dynamic behavior of the star-shaped loop is very different from that of the flower defect described previously. In contrast to the hexagonal "flower defect" structure, which is reported in experiment to show the most rapid shrinkage, the star-shaped structure does not change. Even though the dislocations in the star-shaped structure can still translate in the direction of their Burgers vectors, the shrinkage pathway through coupled translation and rotation to higher misorientation (preserving $R\theta$) described by Cahn and Taylor[116] is closed to this structure.

Even using the tweezer-mimic model of preparation, the trends in mobilities seen in simulations are not generally consistent with the experimental observations of Lavergne *et al.,* who found a general relationship over varying initial size R_0 and misorientation θ_0:

$$1/M^* = K(R_0\theta_0 - [R\theta]^c) \quad (4.3.1)$$

The approximately linear trend is followed only for the smaller loops at the higher pressures (Fig. 4.8, panels b and c, dashed blue curves). The larger loops show little dependence of mobility on misorientation.

Adland *et al*. originally proposed the universal scaling of the inverse mobility with $R\theta$ as a consequence of two factors:[53] the rotation of the grain during shrinking, required to preserve dislocation structure until the final stage of shrinking, and a dissipative contribution from this rotation that scales with the area of the grain. Phase-field-crystal simulations showed an increasing misorientation with shrinking grain size, maintaining fixed $R\theta$, for initial misorientation angles up to 15° (in a square-lattice system). At higher misorientation, a faster, alternative pathway that relied on dislocation reactions rather than grain rotation was observed. They focused primarily on the regime where rotation was seen and showed that reducing the friction associated with collective rotation of the grain (using a "minimized bulk dissipation" model) removed the strong dependence of mobility on misorientation.

Rotation of the grain to higher misorientation is almost never observed in the current simulations, and so based on that model a data collapse according to $R\theta$ would not be expected. Curiously, the experimental data for the plastic deformation regime do show scaling with $R\theta$ (shown in Eq. 4.3.1) even though the shrinkage mechanism (as shown in Movie S1) is not characterized by bulk rotation of the grain.[54] The theoretical underpinning for the behavior described by Eq. 4.3.1 is therefore unresolved.

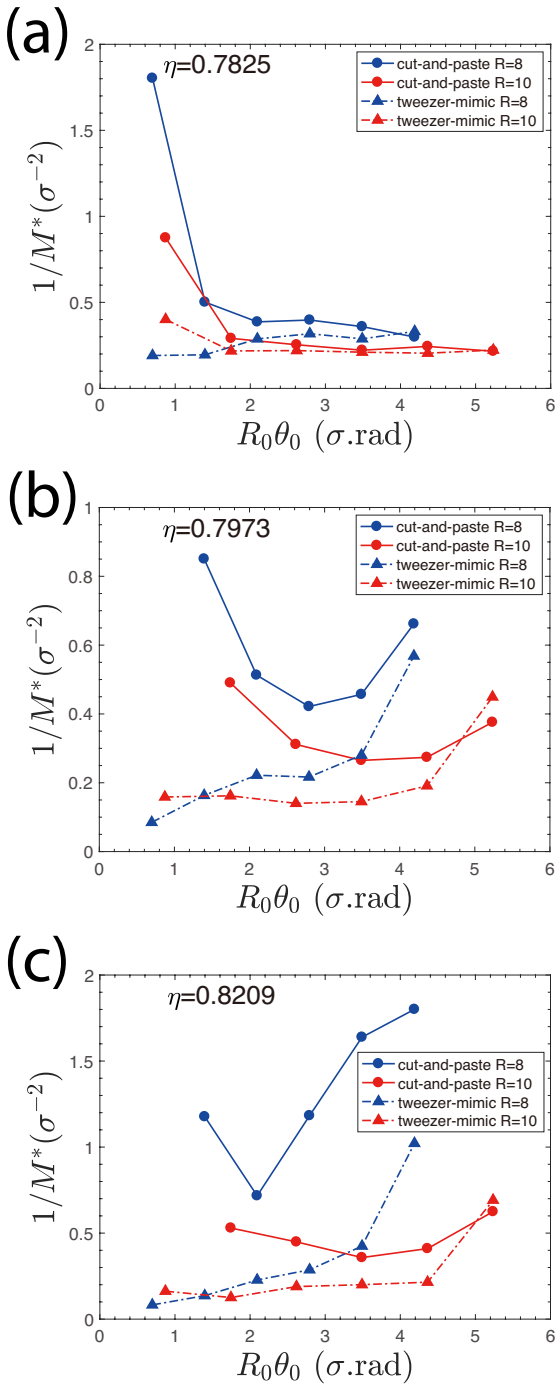

Fig. 4.8 Relation between $1/M^*$ and $R_0\theta_0$ for system (a) at bulk area fraction 0.7825; (b) at bulk area fraction 0.7973; (c) at bulk area fraction 0.8209.

4.4 Conclusions

To summarize, the relaxation of an isolated misoriented grain bounded by a GB loop in a 2d HS passes through several regimes depending on pressure, size, θ, and method of preparation. At low pressure, where fluctuations in the GB and formation of dislocations are facile, the rate of shrinkage is controlled by the driving force (line tension) that will bias the very mobile GB towards reducing the overall perimeter of the included grain, as we have reported previously[112]. At higher pressure, dynamics of GB shrinkage becomes more sensitive to the details of defect arrangement, and hence will depend on all three factors. In the limit of high pressure and small loop size the simulation results are broadly consistent with the experimental observations of Lavergne *et al*. First, small enough domains created by twisting may relax elastically if the rotation is not sufficient to allow for a stable arrangement of dislocations. (A GB loop of similar size and misorientation created by a "cut and paste" approach may, however, remain locked in place due to its dislocation patterns preventing grain shrinkage.) At higher misorientation, our GB loops of radius 8σ display the reverse of the low-pressure trend, shrinking more rapidly at lower misorientation as reported in experiment. The data do not, however, show the same common dependence on $R_0\ \theta_0$ as reported by Lavergne *et al*.; at higher R=10, the misorientation dependence is weaker.

Chapter 5

Ordering of colloidal hard spheres under gravity: From monolayer to multilayer[3]

The phase behaviour of hard spheres confined by a gravitational potential to a thin layer (up to several monolayers) near a hard, flat surface is investigated using grand canonical Monte Carlo simulation. Depending on the strength of the gravitational field, the bottom monolayer of spheres may adopt uniform hexagonal order before, during, or after the growth of the second layer of particles. The crossover from ordering with a sparsely populated overlay to ordering with almost one-third of the system's particles forming a second layer is observed upon decreasing the dimensionless Péclet number Pe = $mg\sigma/k_BT$ from 18 to 16. The particular sensitivity of the nature of the transition to particle size in this range is interpreted in terms of competing influences on the base layer structure by particles in the overlayer: promotion of order through increased pressure, versus stabilization of defects through occupation of low-lying sites on top of them. Simulations of grain boundaries between 2-d ordered domains of different orientation are used to correlate the degree of overlayer coverage to its effects on grain boundary stiffness as an indicator of defect free energy. Finally, we examine the structure of the ordered phases at coexistence over a range of gravitational strengths and find that orientational ordering of the second monolayer occurs along with first-order transition of the base layer at Pe=8 but not at Pe=10.

3. Reproduced from Ref. 195 with permission from the Royal Society of Chemistry.

5.1 Introduction

When packed at high enough lateral densities, hard spheres confined to a plane undergo a transition to a hexagonally ordered state, in a process that has been studied for decades through theory and computation.[117] Only recently have computer simulations on large systems been able to describe this transition unambiguously as a two-stage process: a discontinuous transition from a fluid to a hexatic liquid crystalline structure followed by a continuous transition to a 2-d solid.[118] Even more recently, this two-stage process has been observed in experiments on monolayers of confined spherical colloidal particles.[119] Ordered arrays of colloidal particles in two and three dimensions may be prepared via a variety of routes[120] and find applications in optics, electronics, and sensing.[120] Surface tension effects frequently drive colloids to adsorb strongly to interfaces between immiscible fluids, forming Pickering emulsions.[121-123] Although colloidal monolayers at hard surfaces or fluid interfaces may interact via a wide range of direct and interfacially-mediated (e.g. capillary) forces, at high enough lateral densities simple steric effects are likely to dominate these interactions and hard-sphere (HS) models become relevant.

This work builds on the now well-understood behaviour of the ordering transition of HS in a purely 2-d environment to address questions about this ordering under a gravitational field for sedimented particles. The ordering of sedimented HS in the multilayer limit under mild gravitational confinement has been studied in depth,[124-132] as has the quasi-2d phase behaviour of HS under confinement between hard walls.[99, 133-135] In systems of sedimenting particles, the Péclet number (Pe $= mg\sigma/k_BT$, equivalent to g^* or $1/l_g$) is equivalent to the gravitational potential energy in units of k_BT required to raise the particle by a distance of its diameter σ. Using the buoyant density of silica spheres in water at 300 K as an example, the conversion from Pe to diameter is Pe = 2.06 $\mu m^{-4}\sigma^4$. (It has been noted[125] that an alternate definition of the Péclet

number at Pe $= (\Delta\rho)gR^4/k_BT$ also appears in the literature[131, 132] and gives a value 8 times less.) A recent computational and experimental study[136] has been made of structure and dynamics of colloidal monolayers under a moderate Pe (=6.3), but like earlier simulation work on the subject[137] it stopped short of any ordering transitions. Marechal and Dijkstra have used grand canonical Monte Carlo simulation to study ordering in HS multilayers under gravity, showing among other things that simultaneous freezing of the lowest two layers is a first-order transition in the range Pe=1-4, but that at Pe=10 the ordering of the second layer proceeds continuously after the freezing of the base layer,[129] a result that was corroborated through experiment.[138]

As spheres are added to the system they may either (roughly speaking) increase the density of the lowest level at a cost in packing entropy or occupy positions on top of this lowest level at a cost in gravitational energy. At high Pe, we do not expect significant population above the base layer until the base layer is densely packed and in the 2-d solid state. Thorneywork *et al*. demonstrated this behaviour in showing that monolayers of colloidal spheres with Pe=41 undergo two-stage melting at densities close to the transitions derived from simulations of of hard disc (HD) systems.[119] For more weakly confined particles, the lateral pressure in the base layer may be high enough to push particles to the second level before the hard disk (HD) ordering transition is reached. Using results from our previous work,[139] we can estimate the critical value of Pe at which the crossover takes place. The cost in gravitational energy to add to a second layer above a close-packed monolayer is $\sqrt{2/3}$ (=0.816) Pe k_BT. The entropic cost to add a particle to a densely packed, ordered monolayer can be estimated from 2-d HD simulations[139] where the ordering transition occurred at a chemical potential of 12.8 k_BT/molecule. These are equal when Pe=15.6; we may estimate that above this value (which corresponds to 1.66 μm diameter spherical silica beads in water at 300 K), ordering of the base layer will precede population of the overlayer. For

particles with Pe below this threshold, as increasing numbers of particles accumulate in one or more upper layers, their weight will eventually produce enough pressure to drive an ordering transition in the base layer (or layers). A main goal of this work is to test this prediction through simulation.

The phase behaviour of HS confined to a slit pore with hard walls has been studied extensively through simulation[99, 134, 135, 140] and experiment[133, 141, 142] and bears some similarity to the gravitationally confined systems to be modelled here. Particles held in soft confinement near a plane through a harmonic potential[143] have also been studied. At high packing density, these systems may adopt ordered structures with integer numbers of planar hexagonal (triangular) or square arrays; more complex intermediates (e.g. buckled structures) are also observed under hard wall confinement, while re-entrant melting or phase coexistence is seen under soft confinement. The non-hexagonal packing modes are driven by a trade-off between packing efficiently within a plane while accommodating multiple layers. In the present system, the broken symmetry between layers makes optimization of the packing efficiency in the base layer the most important factor, so we expect to see only hexagonally symmetric ordered structures.

In this work, we explore gravitationally confined HS monolayers and bilayers with a relatively high range of Pe from 6 to 24. Here we use the solvent repacking Monte Carlo (SRMC) method,[139] along with a new extension adapting the simulation under a gravitational potential, to study the equilibrium phase diagrams and properties of gravitationally confined HS. The effects of overlayer on the thermodynamics of disordering are then singled out using studies of grain boundary (GB) stiffness. Finally, we address the structural nature of ordering in the ordered phase at coexistence in different limits.

5.2 Methods

5.2.1 Algorithms for grand canonical Monte Carlo under a gravitational potential

We treat a monodisperse system of HS whose minimum centre-of-mass position along z is limited to $z = 0$ by a hard, flat surface in the *x*-*y* plane ("floor") and whose maximum position along z is influenced by a gravitational potential $U = \mathrm{Pe}\, k_B T z$ and limited to z_{max} by a second hard wall ("ceiling"). We wish to establish an equilibrium between this system and a reference system of fugacity f, which can be characterized as a hypothetical non-interacting system of particles in a field-free 3-d space ($U = 0$) at a number density f in units of σ^{-3}.

5.2.2 Single particle addition/removal moves

The standard Grand Canonical Monte Carlo algorithm for such a system would be inefficient at high Pe and high z_{max} because most insertion move attempts would be at heights with low thermal population. Biasing the distribution of insertion attempts by the gravitational potential is a natural solution. Given the normalized probability distribution $P(z) = \mathrm{Pe}\, e^{-\mathrm{Pe}\, z}/(1 - e^{-\mathrm{Pe}\, z_{max}})$, acceptance probabilities that would appropriately account for the bias can be easily constructed:

$$acc_{N\to N+1} = \min\left(1, \frac{f\frac{V}{N+1}e^{-\mathrm{Pe}\, z}}{P(z)}\right) = \min\left(1, f\frac{V}{N+1}\frac{(1-e^{-\mathrm{Pe}\, z_{max}})}{\mathrm{Pe}}\right) \tag{5.2.1}$$

$$acc_{N+1\to N} = \min\left(1, f^{-1}\frac{N+1}{V}\frac{\mathrm{Pe}}{(1-e^{-\mathrm{Pe}\, z_{max}})}\right) \tag{5.2.2}$$

For a system that is densely packed near $z = 0$ at high Pe, this will again produce inefficiencies because the insertion moves will be concentrated at the most densely packed region. To increase the rate of exchange for the uppermost layer at least, while retaining the possibility of inserting

into cavities that open up near $z = 0$, we instead bias insertions according to the gravitational potential but over a range determined by a "local floor" using the following steps:

1) A point within the *x*-*y* plane is selected at random.

2) The positions of all particles whose *x*, *y* coordinates are in a cylinder of radius σ centered at that point are used to calculate the height z at which a particle falling from z_{max} would first collide with the existing particles; this is denoted z_{floor}. If there are no particles within that cylinder, $z_{floor} = 0$. If a particle at z_{max} would overlap with an existing particle, the move fails.

3) The trial z coordinate is selected from the range $[z_{floor}, z_{max}]$, with probability weighted by $e^{-\mathrm{Pe}\, z}$.

The acceptance probability for insertion moves is then

$$acc_{N \to N+1} = \min\left(1, f \frac{V}{N+1} \frac{\left(e^{-\mathrm{Pe}\, z_{floor}} - e^{-\mathrm{Pe}\, z_{max}}\right)}{\mathrm{Pe}}\right) \tag{5.2.3}$$

We note that this move can never insert a particle underneath another particle.

For the removal move,

1) One of $N + 1$ particles is selected at random. The positions of all particles whose *x*, *y* coordinates are in a cylinder of radius σ centered at that particle's projection on the *x*, *y* plane are used to calculate both z_{floor} and $z_{ceiling}$: the positions at which the particle would make contact (with walls or other particles) if it were to fall or rise without changing lateral position.

2) If $z_{ceiling}$ is less than z_{max}, there is another particle above our trial particle, and the move fails because it could not be reversed by an on-top addition and so would violate detailed balance.

3) The acceptance probability for removing the selected particle is

$$acc_{N+1 \to N} = \min\left(1, f^{-1} \frac{N+1}{V} \frac{\mathrm{Pe}}{\left(e^{-\mathrm{Pe}\, z_{floor}} - e^{-\mathrm{Pe}\, z_{max}}\right)}\right) \tag{5.2.4}$$

If the removal move fails for either reason (either because the particle has another one above it, or because the acceptance probability is less than 1), knowing z_{floor} and $z_{ceiling}$ allows us to make a rejection-free move along z, translating the particle to a position between these two values with a probability weighted by $e^{-\mathrm{Pe}\,z}$. This move is appealing in that the effective step size adapts automatically both to the local packing environment and the gravitational confinement, removing the need to re-optimize the step size to sample height distributions efficiently. The thermal distribution for an ideal (non-interacting) system under the gravitational potential with fugacity defined in this way would be:

$$\rho_{3d}(x, y, z) = f \exp(-\beta U) = f \exp(-\mathrm{Pe}\, z) \tag{5.2.5}$$

Integrating $\rho_{3d}(x, y, z)$ over z then yields a number per unit area of $f(1 - e^{-\mathrm{Pe}\, z_{max}})/\mathrm{Pe}$. The single-particle on-top insertion and removal moves are in principle valid at any value of Pe, although for multilayer systems their ability to converge to the correct ensemble of particle numbers and configurations at a given fugacity relies on the efficient exchange of particles within and between layers below the top layer, through local moves.

5.2.3 Solvent Repacking MC Moves under gravitational potential

The SRMC algorithm has been detailed in several publications.[139, 144] In the present system, the goal of the algorithm is to allow a local region of the system to adopt a new packing that might be kinetically inaccessible through single-particle moves. Disorder in the base layer can be stabilized by the presence of overlayer particles, and so in principle trial configurations that allow both layers to be altered simultaneously could overcome barriers to structural transitions.

Like in previous work on 2-d systems, a position is randomly selected within the system and a set of trial configurations is generated in which all particles within a lateral distance r_{cut} are

replaced with varying numbers of particles, whose positions are chosen using the configurational bias MC (CBMC) strategy.[145] In the present case, we wish to build a configuration of particles that may extend to a second layer (or beyond) with guidance from the gravitational potential energy. As before, for the *i*'th particle added to the new trial configuration, a number *k* of positions in *x* and *y* are generated randomly within the circle of area πr_{cut}^2. For each position, the local floor z_{floor} is calculated as defined above, except that only interactions with the previous *i*-1 particles in the new configuration (not with the surrounding "shell" particles that may overlap with trial positions) are used for this calculation. The new particle's *z* coordinate is selected with an exponentially biased distribution ($\propto e^{-Pe\,z}$) between z_{floor} and z_{max}. Trial positions that overlap shell particles are rejected, and one of the remaining positions is selected with a probability weighting

$$P_{i,j} = \frac{e^{-\beta u'_{i,j}}\left(e^{-Pe\,z_{floor,i,j}} - e^{-Pe\,z_{max}}\right)}{\sum_{j'=1}^{k} e^{-\beta u'_{i,j'}}\left(e^{-Pe\,z_{floor,i,j'}} - e^{-Pe\,z_{max}}\right)}$$

$$= \frac{e^{-\beta u'_{i,j}}\left(e^{-Pe\,z_{floor,i,j}} - e^{-Pe\,z_{max}}\right)}{w_i} \qquad (5.2.6)$$

where $u'_{i,j}$ is an auxiliary potential, derived from a radial distribution function, that favours closely packed positions, and a Rosenbluth weight w_i associated with the placement of the *i*th particle is introduced. (The same auxiliary potential was used here as in previous work.[144, 146]) Particle addition is continued until either a predetermined maximum is reached or all positions generated are invalid ($z_{floor} > z_{max}$).

A complication arises as we need to account for the probability of generating a given set of *i* particle positions in this manner, including permutations to the order in which they may be generated. If no particle is above any other particle (in the sense that $z_{floor} = 0$ for all), then the number of permutations equals *i* factorial. In the event that some particles are on top of others, some of these permutations violate the ordering requirement for particles to be inserted earlier than

those that are on top of them. To sample and count the allowed permutations for a given arrangement of i particles, we first count the number $n_{top,i}$ of particles that have no particles below them, randomly select one to remove, and continue recounting until a single particle is left. The product of $n_{top,i}$:

$$N_{perm,i} = \prod_{i'=1}^{i} n_{top,i'} \tag{5.2.7}$$

will equal the number of permutations, and so is used in place of $i!$ in expressions for the acceptance probability. The probability weighting associated with the configuration r^i of i particles within the grand canonical ensemble is

$$P(\mathrm{r}^i) \propto \frac{f^i}{\Lambda^i} \exp\left(-Pe \sum_{i'=0}^{i} z_{i'}\right) \tag{5.2.8}$$

The probability of generating that given configuration (including selecting lateral positions for i particles from an area $a_{cav} = \pi r_{\mathrm{cut}}^2$, generating z coordinates from the gravitationally biased distribution between z_{floor} and z_{max}, and selecting one of k positions according to Eq. (5.2.7)) is:

$$\alpha(\mathrm{r}^i) = N_{perm,i} \prod_{i'=1}^{i} \left(\frac{k_{i'}}{a_{cav}}\right) \left(\frac{Pe\ e^{-Pe\, z_{i'}}}{e^{-Pe\, z_{floor,i'}} - e^{-Pe\, z_{max}}}\right) \frac{e^{-\beta u'_{i'} - Pe\, z_{floor,i'}}}{w_{i'}} \tag{5.2.9}$$

Acceptance probability weightings for moves in biased Monte Carlo algorithms should be proportional to the desired weighting within the ensemble and inversely proportional to the generation probability; dividing Eq. (5.2.8) by Eq. (5.2.5) yields the acceptance probability weighting of the new configuration with i particles:

$$\omega_i = \frac{f^i}{\Lambda^i} \frac{{a_{cav}}^i}{N_{perm,i} \prod_{i'=1}^{i} k_{i'}} \frac{\prod_{i'=1}^{i} w_{i'}}{\exp\left(-\beta U'_i\right)} \tag{5.2.10}$$

As in conventional CBMC, all factors in Eq. (5.2.9) for the original (old) configuration must also be generated, using k-1 "dummy" alternate positions for each particle positioned to generate $w_{i,\mathrm{old}}$ according to Eq. (5.2.7) and adding new additional "dummy" particles up to the same

stopping criterion as for the new structure. The acceptance probability for choosing one of the new structures is then:

$$acc = \min\left(\frac{\sum_{i=0}^{i_{max}} \omega_i}{\sum_{i'=0}^{i_{max}} \omega_{old,i'}}, 1\right) \tag{5.2.11}$$

If the move is accepted, the choice of how many of the particles to include in the new filling of the cavity (including the vacant cavity, i=0, with weight 1) is made through a random selection with probability:

$$P(i) = \frac{\omega_i}{\sum_{i'=0}^{i_{max}} \omega_{i'}} \tag{5.2.12}$$

5.2.4 Implementation of grand canonical Monte Carlo (GCMC) simulations

GCMC simulations with varying fugacities f and Péclet numbers Pe were carried out through the moves described above using a grid-based domain decomposition scheme in which the system (a square box with periodic boundary conditions in two dimensions, whose size depended on the type of simulation as detailed below) is divided into $n \times n$ sectors. During each cycle, a new origin for the first sector of the grid is selected at random and a series of Monte Carlo moves attempts is performed independently on a different processor on each sector, with boundary zones of width 1σ between the sectors kept unchanged (with no particles allowed to enter, leave, or change position). A single cycle consisted of 1000 SRMC repack attempts on each sector, each of which was followed by 600 single-particle move attempts. The type of single-particle move was randomly selected with equal chances of a simple lateral translational move attempt at constant z, a single-particle (on-top) insertion attempt, or a single particle removal/rejection-free vertical translation move as described above.

To determine the boundaries between ordered and disordered phases in systems with Pe numbers ranging from 6 to 24, a simulation box of lateral dimensions $100\,\sigma \times 100\,\sigma$ was used, divided laterally into 16 sectors for parallel sampling. At each value of Pe, we use an estimation and trial strategy to find the transition point. Starting from an empty box, simulations were performed at widely spaced trial fugacities, and the total particle number was monitored until it reached a stable level. This typically was achieved within 5,000-10,000 MC cycles (with each MC cycle including a total over all sectors of 16,000 repacking moves attempts and 9.6×10^6 single-particle move or insertion/removal attempts). The base layer (defined as particles with $z < 0.5\,\sigma$, where $z = 0$ represents the particle in contact with the hard surface) was visualized using VMD[147] to determine whether it had reached a state of uniform hexagonal order. The structure at the lowest fugacity to yield an ordered state was then used as input for a series of simulations at gradually decreasing fugacity, until a system was observed in which the uniform order of the base layer was lost (melted). Simulations initiated with disordered structures were then performed at smaller increases of fugacity (increments of 5-10%) until ordering was resumed. In this way we zeroed in on a transition fugacity value –where the same fugacity will result in the ordered structures remaining ordered and the disordered structures remaining disordered over a 10,000 MC cycle trajectory. Although there is some imprecision in this procedure, as the range of the bistable regions is finite for a finite equilibration time, the outer limits of this range (which we could place by the fugacities at which spontaneous transitions were observed) were far narrower than the shifts in the transitions from varying Pe. The properties of the two phases at coexistence are then approximated from the configurations observed at that transition fugacity obtained using different starting structures. To represent the density of the system with a measure that reduces to the 2-dimensional area fraction in the limit of a monolayer at infinite Pe, the total area fraction $\eta_{tot} =$

$\frac{\pi}{4}\frac{<N>}{A}$ is used, representing the mean sum of all projected areas of all spheres in the system as fraction of the area of the surface. (This measure can exceed 1 because of the possibility of multiple layers). The area fractions η_{base} and η_{over} of the base layer (particles with $z < 0.5\sigma$) and the first overlayer (particles with $0.5\sigma < z < 1.5\sigma$) are similarly defined.

With one exception, the ceiling height was set to $z_{max} = 5\sigma$; the choice of this maximum is large enough that the density of particles at or above this height is close to zero and should have negligible effects on the results presented. In one case, at Pe=8, an additional series of simulations was performed using ceiling height z_{max} = 0.5σ to confine the particles in the system to the first layer, and the transition fugacity of such a system (where overlayer formation is effectively curtailed) was determined in the same manner as above.

To systematically study the GB stiffness and its dependence on system composition and Pe under controllable conditions, ordered grains of spheres are set up in a pair of parallel stripes making two parallel GBs aligned with the x direction in a square simulation box (side length 200 σ) as in previous work.[144, 146] Equilibration and production periods consisted of at least 5000 and 20000 MC cycles, respectively.

5.2.5 Analysis of orientational and translational order

At each value of Pe, the complex hexagonal bond orientation order parameter Ψ_6 was determined for all particles in the base layer ($z < 0.5\sigma$); for systems with Pe=6, 8, and 10 the order parameter was also determined separately for particles in the first overlayer ($0.5\sigma < z < 1.5\sigma$).

$$\Psi_6(\vec{r_j}) = \frac{1}{N_j}\sum_{k=1}^{N_j} e^{i6\theta_{jk}} \tag{5.2.13}$$

Here the number of neighbours N_j is defined as the number of particles within the same layer (base layer or first overlayer) with projected distance from particle j in the x-y plane less than 1.5 σ,

and θ_{jk} is the angle between the *y* axis and the *x*-*y* projection of the bond vector between particle j and its k^{th} neighbour.

Selected systems were prepared in the ordered phase and equilibrated at the transition fugacity in a larger simulation box ($350\sigma \times 350\sigma$) to reduce finite size effects calculation of translational order correlation function following a procedure given in a previous study.[139] The direction of translational correlation vector is chosen based on the orientation of the domain, to obtain the longest possible correlation length.

5.2.6 Grain Boundary detection and calculation of grain boundary stiffness

To detect the two GB's positions along the *x* dimension from simulations of bicrystals, we divide the simulation box into a 100×100 grid, which has been confirmed to be fine enough for calculating interfacial stiffness in our previous study.[144, 146] The orientation of the hexagon formed by six neighbours of particle j can be calculated by $\theta_6 = \arg(\Psi_6)/6$, which is a value varied from 0 to 60° due to the symmetry of hexagon, using only particles in the base layer. The orientation of the grain domain can be quantified by averaging all the θ_6 of particles belonging to the domain. Here in all cases GB were constructed with grain misorientation (difference between the two grains' orientation angles) of 30° and inclination (angle between the GB and grain orientations) of 15°. Smoothing over local pockets of disorder is achieved by taking the average of θ_6 in each grid and the four nearest grid squares of the same *x* coordinate to represent the orientation of each grid square. The height h of the grain boundary is then the *y* coordinate of the grid square with θ_6 closest to the mean of the θ_6 values of the two grains, defined as the "edge point", and the GB is represented as a sequence of segments connecting "edge points"

The capillary fluctuation method (CFM) is applied here in the same way as in previous work to calculate GB stiffness.[144, 146] The GB positions along the *y* direction determined as described in previous section are treated as a function of position along the x direction and frame t: $h(x,t)$. The mean value of $h(x,t)$ at each t is subtracted off to yield the fluctuation at that frame: $\delta h(x,t) = h(x,t) - \langle h(t)\rangle_x$, which can be converted to $\delta h(k,t)$ by Fourier Transform (F.T.) with wave number k=$2\pi m/L$ ($m = 0, \pm1, \pm2, ...$) in Fourier Spectrum. The trajectory-averaged square of intensities $\langle|\delta h(k)|^2\rangle_t$ are related to the stiffness Γ according to the CFM as:[148]

$$\log(\langle|\delta h(k)|^2\rangle L) = -2\log(k) + \log\left(\frac{k_B T}{\Gamma}\right) \qquad (5.2.14)$$

In practice, a linear fit of Eq. (5.2.13) with a fixed slope –2 is used to find stiffness Γ from the *y*-intercept, excluding points with $|m|$ higher than 15, which the CFM as a continuum-based model is not expected to fit. In ordered systems with Pe=10 and below, convergence in GB fluctuation statistics was not reliable and so is not reported.

5.3 Results and Discussion

We will first show how the point of transition of the base layer from fluid to ordered phase depends on the degree of gravitational confinement as represented by Péclet number Pe. The second section will focus on interpreting these trends through consideration of the effect of overlayer particles on the ordering of the base layer, which can be studied more directly by examining the property of grain boundary stiffness at packings above the phase boundary. Finally, the evolution of the nature of the ordered phase near coexistence will be considered, including both lateral translational correlations and the degree to which the second and third layers order in concert with the base layer.

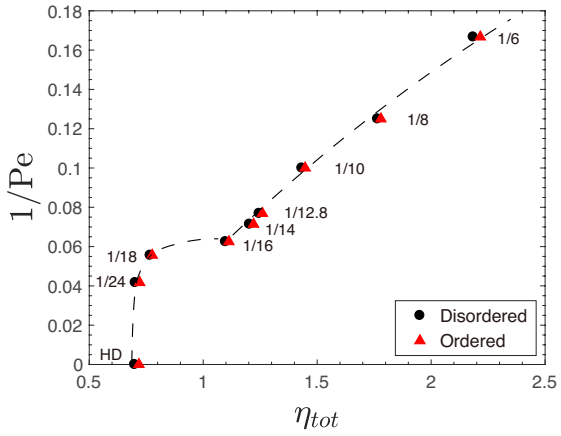

Fig. 5.1 Phase diagram of gravitationally confined HS systems with different Pe. The dash line is drawn only to guide the eyes to indicate the phase boundaries. The data of HD is obtained from previous work.[139]

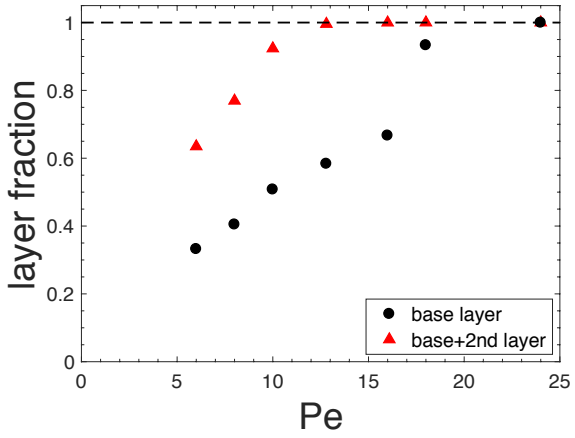

Fig. 5.2 Percentage of number of base layer particles at phase transition in ordered phase with different Pe.

5.3.1 Crossover from ordering before stacking to ordering with overlayer present

We first studied the phase transition points of gravitationally confined HS under different Pe. As predicted, we see a shift in behaviour from an ordering transition that precedes population of overlayer sites (at high Pe) to an ordering transition that occurs with significant overlayer population (at low Pe). The transition appears to take place in the range of Pe between 16 and 18,

close to our estimate of 15.6. As shown in Fig. 5.1, the ordering transition for sedimented HS with relatively high Pe (18 and 24) takes place at a total area fraction η_{tot} shifted only slightly from the

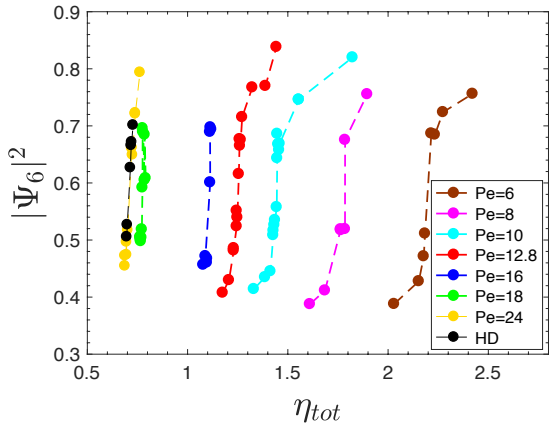

Fig. 5.3 Mean squared order parameters $\langle|\Psi_6|^2\rangle$ of base layer particles versus total area fraction η_{tot} near phase transitions at different Pe.

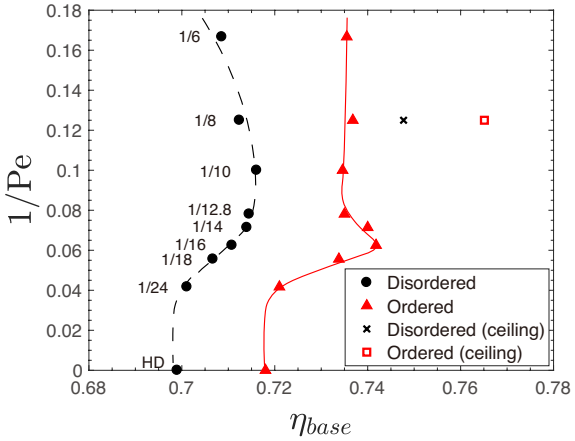

Fig. 5.4 Phase diagram of gravitationally confined HS systems with different Pe plotted again the base layer area fraction η_{base}. The lines are drawn only to guide the eyes to indicate the phase boundary in disordered phase (black dash line), and ordered phase (red solid line). The data of HD is obtained from previous work.[139]

HD system, since the occupancy of the overlayer is low, (see Fig. 5.2) and since the vertical fluctuations in the base layer are small. Upon decreasing the Pe from 18 to 16, η_{tot} at the transition is dramatically increased, reflecting the presence of a significant (~37%) overlayer. On further lowering of Pe from 16 to 6, η_{tot} at the transition gradually increases, reflecting the need for more and more particles in the upper layers to exert sufficient pressure on the base layer to drive the transition.

5.3.2 Overlayer effects on phase and interface stability

The base layer of HS in the sedimented system differs from the simple HD system in two potentially important ways: the presence of an overlayer and the fluctuations in height (position along z) that allow the spheres to approach each other with lateral distances less than their diameter. Over the range of Pe investigated, the boundaries of the ordering transition remain close to the HD limit, in terms of the shift in base layer hexagonal order parameter Ψ_6 (Fig. 5.3) as well as the nominal area fraction η_{base} of the base layer (Fig. 5.4). To distinguish effects of the overlayer from those of the fluctuations, we have simulated the Pe = 8 system under conditions where particles are restricted to a height z_{max} = 0.5σ (corresponding to a hard ceiling at a height 1.5 σ above the floor). This restriction prevents formation of an overlayer while allowing considerable thermal height fluctuations. The transition boundary is shifted to higher area fraction (cross and square marks in Fig. 5.4) relative to the HD limit, as expected given the effective softening[149] of the lateral excluded area restrictions due to fluctuations in z. This shift is qualitatively consistent with the shifts in phase boundaries observed for HS confined between parallel walls in the absence of a gravitational field.[99] In contrast, when the ceiling is not present, it is noteworthy that the area fraction of the ordered base monolayer at the phase boundary barely changes in the range from Pe=6 to Pe=12.8, remaining near η_{base} =0.735. (For comparison, the value of η_{base} for a monolayer formed by the (111) face of an FCC crystal at the bulk HS freezing point, with volume fraction from simulations[150] determined to equal 0.545, is η=0.739.) It appears that the doubling in the degree of direct gravitational confinement on the base layer particles and the decrease in the number of particles above the base layer are compensating for each other to produce a consistent packing density in the ordered monolayer at coexistence. This trend is consistent with previous

GCMC study that found of similar lattice parameters across ordered phases observed at the transition in the range Pe=1 to 4.[129]

A related form of compensation is evident in the height distribution of the base layer, shown in Fig. 5.5, for particles of different Pe under conditions with the same base area fraction (η_{base}≈0.755, well above the ordering transition). The height distribution broadens as expected when Pe is reduced from 100 to 50 to 24, as gravitational confinement is weakened, then remains approximately unchanged as Pe decreases by another factor of 2. Is this compensation to be expected? In a simplified scenario (neglecting any specific effects of overlayer particles on the base layer packing behaviour) the lateral pressure within the base layer could be assumed to depend solely on η_{base}. If enough particles are present in the overlayer so that lateral and vertical forces are coupled, this lateral pressure would be expected to be approximately equal to the pressure in the z direction. The pressure on the floor can be equated to k_BT times the number density at $z = 0$ (corresponding to particles whose center is 0.5σ above the hard surface).[129] Interestingly, even though the height distributions look remarkably similar over the range from Pe=12.8 to Pe=24, the pressure on the floor (as indicated by the density at $z = 0$) shows a spread of about 20%. This indicates that there are subtleties that modulate the dependence of lateral pressure on η_{base} and/or that the lateral pressure does not equal the normal pressure. (It would in fact be surprising if the lateral pressure were to equal the normal pressure exactly near a phase coexistence in a thin sedimented system: the lateral pressures of two coexisting phases must be equal to minimize the free energy of the two-phase system, and unless the two phases have the exact same η_{tot}, they will not have the same normal pressure.) Still, to a first approximation the combination of the direct effect of gravity on the base layer particles and the pressure due to the weight of the overlayers produces a similar height distribution at a given η_{base}, which in turn would be expected to produce

a similar effective 2-d equation of state for the base layer over different values of Pe – absent specific perturbations to the ordering process from overlayer particles. The non-specific effect of increasing overlayer coverage therefore should be expected to favour ordering through its effects on base layer pressure.

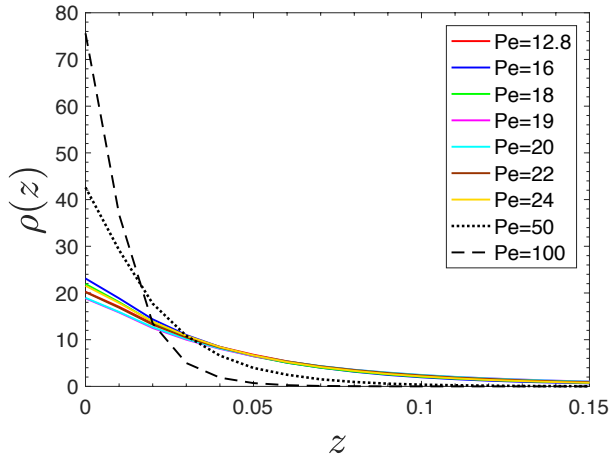

Fig. 5.5 Height distribution in base layer at common η_{base} (~0.755) in base layer with different Pe. z is divided to bins with step size 0.01σ. $\rho(z)$ is the number density per unit volume for spheres in each bin.

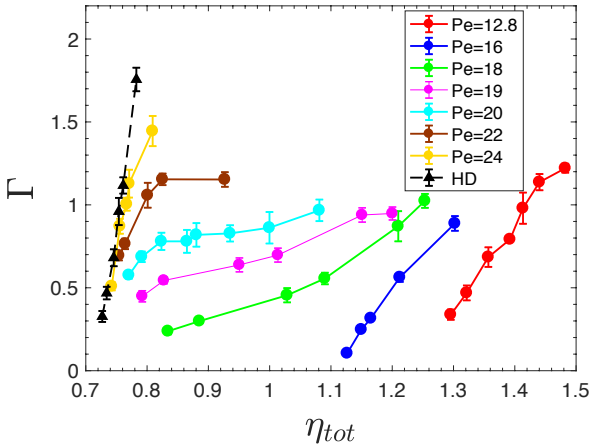

Fig. 5.6 Stiffness of grain boundaries (assessed using base layer only) with different Pe. The data for HD is obtained from previous work.[144]

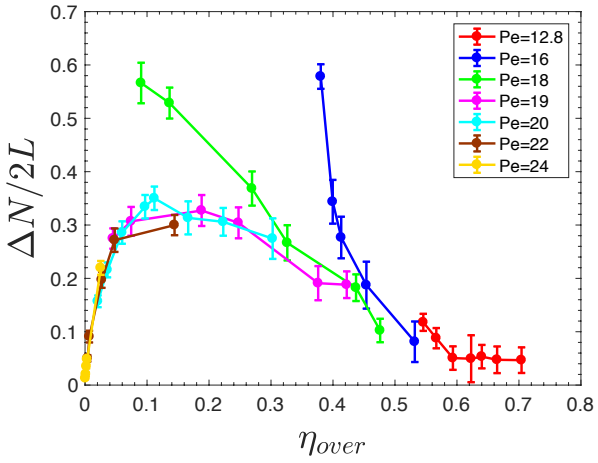

Fig. 5.7 Excess overlayer particles per unit length of GB at different Pe.

To better understand other effects of overlayer coverage on ordering, we turn to the behaviour of grain boundaries, locally disordered regions that separate ordered domains with differently oriented lattices in a polycrystalline system. The fluid phase at the phase transition in HD[118] and similar[151] 2-d systems has some resemblance to a polycrystalline mosaic of locally hexagonal grains with different orientation. In fact, the local hexagonal order is nearly as high as in the fully ordered phase (see Fig. 5.3) and the correlation length associated with this order is about 60 times the particle diameter for HD systems. Properties of GB might therefore be expected to reflect the factors that control where and how the transition takes place. (GB properties also influence the rate of grain coarsening,[40, 96, 144, 152] and are essential for understanding the dynamics of sedimented systems at packings above the ordering transition.) We have compared the (quasi-1d) GB stiffness, which is a measure of the free energy per unit length associated with the GB presence, at different Pe with the HD system (Fig. 5.6). In the HD limit of a fully 2-d system (Pe=∞), GB stiffness increases sharply with increasing area fraction above the transition.[144] This dependence is weaker over a range of Pe in the regime from η_{tot} =0.8 to η_{tot} = 1.1, reflecting the fact that most added particles join the overlayer and only indirectly influence the base layer packing. Moreover, since the local arrangement of the base layer deviates from close-packing at the GB and features larger

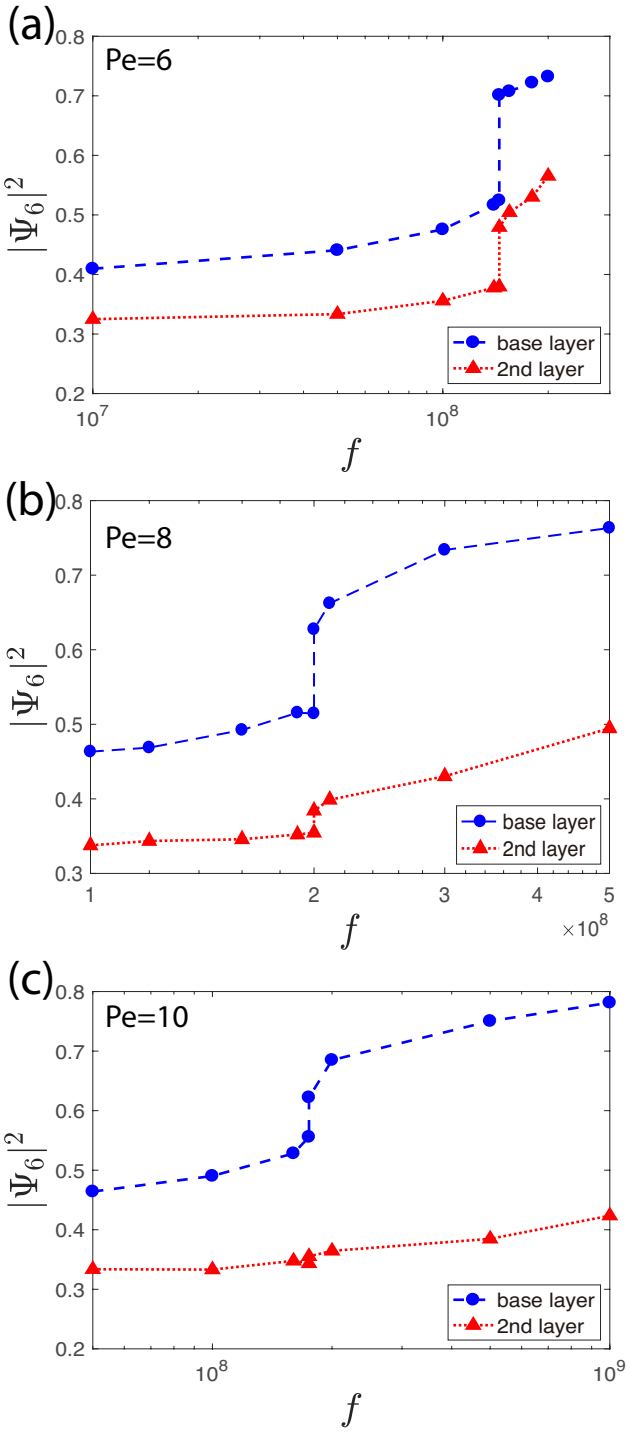

Fig. 5.8 The hexagonal bond order parameter of spheres in base layer (blue circle) and second layer (red triangle) with (a) Pe=6; (b) Pe=8; and (c) Pe=10.

cavities than are present in the bulk, overlayer particles that occupy sites atop these cavities will have lower *z* coordinates and therefore lower potential energy than those occupying sites above

the ordered regions. Counting all overlayer particles, we find a positive excess number of overlayer particles per unit length of the GB, confirming that overlayer particles tend to partition towards the GB and thereby stabilize it. In this way, they are analogous to impurities in mixed systems that similarly reduce GB stiffness.[40, 146] (A kinetic effect on the GB mobility due to overlayer particles, analogous to Zener pinning,[32, 43, 44] is also possible but was not explored in the present study.) Snapshots that visualize only those overlayer particles in the range $0.5\sigma < z < 0.8\sigma$, which is excluded to particles atop closely packed hexagonal regions of the base layer, highlights the enrichment of the GB in these particles. So, in addition to a collective pro-ordering effect of overlayer particles from their influence on the base layer's pressure, we see a pro-disordering effect from individual overlayer particles' affinity for defect sites.

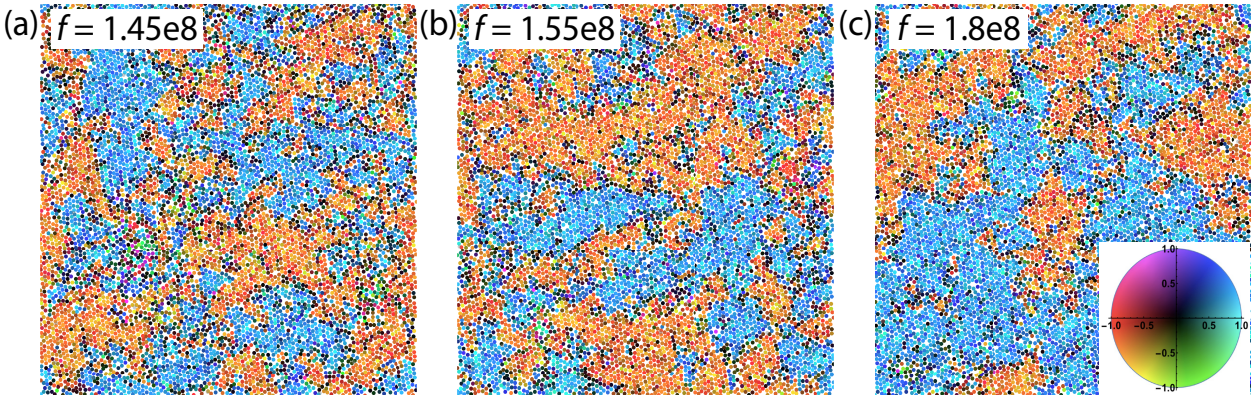

Fig. 5.9 Snapshot of spheres in the second layer in a system with Pe =6 at fugacity (a) 1.45×10^8; (b) 1.55×10^8; and (c) 1.8×10^8 which are in ordered phase near coexistence. The corresponding total area fractions η_{tot} are 2.216, 2.229 and 2.257 respectively. Spheres are colour-coded by order parameter Ψ_3 with respect to the spheres in the base layer, represented by the color map shown in the inset in (c); the x and y axes represent the real and imaginary part of Ψ_3, respectively.

Fig. 5.7 shows that (except for Pe=16 and Pe=18) this excess follows a regular trend with increasing coverage of the overlayer. The excess number $\Delta N/L$ increases with overlayer coverage at low η_{over} because more particles become available to occupy the GB sites. The excess reaches a plateau as these extra-stable sites presumably become saturated. The excess number then starts

to decrease as the overlayer approaches 40% monolayer coverage, as lateral packing pressure within the overlayer grows and tends to suppress local density fluctuations.

The anomalies in Fig. 5.7 at Pe=16 and Pe=18 can be attributed to the fact that in the regime η_{over} =0.1-0.4 that favors high excess numbers at the GB (for reasons described in the previous paragraph) these systems are still close to their order-disorder transitions. Close to the transition point, the free energy cost of local melting in the base layer is relatively low. Overlayer particles that migrate to GB sites and stabilize non-hexagonal arrangements in the base layer can contribute to pre-melting, increasing the number of advantageous sites. In contrast, the common behaviour at higher Pe suggests that the overlayer particles are simply occupying sites determined by the intrinsic structure of the GB; the pressure in the base layer is too high to allow a significant number of additional defects to be formed. Pre-melting at the GB and an expanded zone of enrichment of overlayer particles can be seen in snapshots with Pe=16 and 18, in contrast to the localized distribution of packing defects and of overlayer particles at Pe=20.

The tendency for a partial overlayer to stabilize disordered packing arrangements in the base layer is a reasonable explanation for why η_{tot} at the transition jumps from 0.75 at Pe=18 to over 1.1 at Pe=16 (Fig. 5.1). The same total pressure on the floor would be achieved with an increase only to η_{tot}=0.84. Such an increase would at the same time raise η_{over} to approximately 0.1, a condition that strongly stabilizes defects in the base layer (Fig. 5.7) and so would suppress ordering. The ordered phase does not become stable until η_{over}=0.38, and even in the ordered phase the GB stiffness is especially low at Pe=16 indicating a susceptibility to local disorder (Fig. 5.6).

5.3.3 Structure of ordered phase

The translational correlation function shows that the ordered phase at phase coexistence for Pe = 24 is almost the same as HD, with correlations decaying over a length scale of 10's of particle diameters as characteristic of the hexatic phase.[118] At Pe=16, even though the area packing fraction of the base layer of the ordered phase is much higher (>0.74) than for the HD system, decay of the translational order can still be observed, with a somewhat longer length scale. At Pe=6, the yet weaker decay in translational order correlation makes it difficult to identify whether the system is hexatic with a correlation length approaching the scale of the box size (350 particle diameters) or a 2-d solid with a power law correlation function. In either case, it is likely that the cooperative ordering of the second layer (see following section) contributes to the increased order in the base layer.

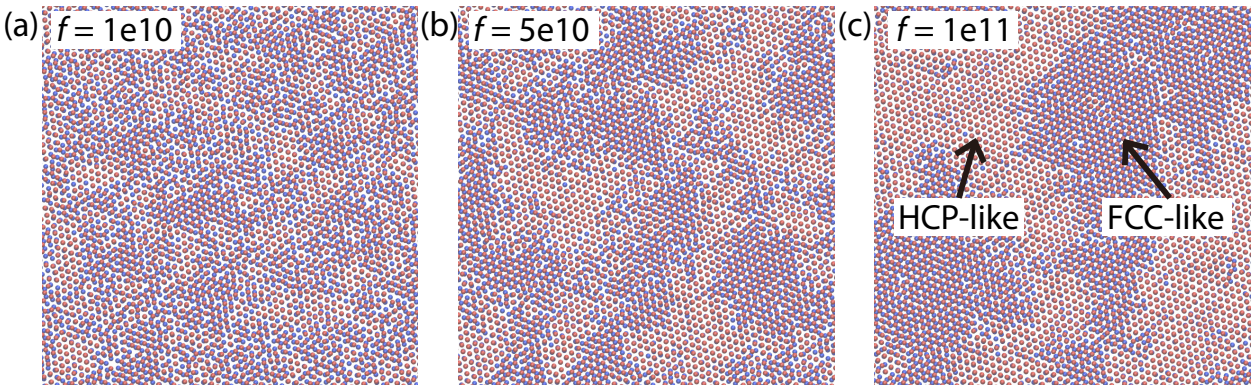

Fig. 5.10 Snapshot of spheres in base layer (blue) and third layer (red) in a system with Pe =6 at fugacity (a) 1×10^{10}; (b) 5×10^{10}; and (c) 1×10^{11}. The spheres in second and fourth layer are omitted for clarification. The corresponding total area fraction η_{tot} is 2.866, 3.113 and 3.232, respectively.

As the gravitational force is lowered, the density along the *z* axis becomes more uniform, so that one might anticipate the equilibrium ordering transition at the surface to evolve from a quasi-2d process to a collective 3-d freezing that extends farther from the wall. As Pe $\rightarrow 0$, one might envision that the loss of the density gradient along *z* would lead to continued expansion of this cooperativity, culminating in a bulk-like transition[150] between fluid at a volume fraction of 0.494 into a many-layered crystal at volume fractions 0.545. On the other hand, the presence of a wall

has been shown to induce ordering below the bulk freezing pressure (prefreezing) in HS systems even in the absence of gravity,[153, 154] suggesting that under reduced gravity the onset of ordering will always remain local to the surface. Marechal and Dijkstra have found that at Pe=10, the base layer freezes without collective ordering of the second layer,[129] and our results are consistent with that conclusion, showing no discontinuity in the second layer order parameter at the transition point for the base layer (Fig. 5.8(c)). At Pe=8 and Pe=6 we see signs of simultaneous discontinuity in the order parameter of the first two layers, suggesting collective freezing, similar to that seen in simulations at Pe=2, 3, and 4 by Marechal and Dijkstra[129] (who also detect simultaneous ordering in the third layer at Pe=1). Particles in the second layer can populate either of two equivalently oriented lattices of trigonal holes formed by the base layer. To distinguish between those lattices, we calculate the Ψ_3 order parameter using the *x*-*y* projection of vectors connecting second-layer particles with the nearest three base layer particles.

$$\Psi_3(\vec{r}_j) = \frac{1}{N_j}\sum_{k=1}^{N_j} e^{i3\theta_{jk}} \tag{5.3.1}$$

A colour map of the second layer for ordered Pe=6 systems at and above coexistence is shown in Fig. 5.9. These snapshots show that the second layer has only short-ranged translational order, with domains that grow gradually with increasing η_{tot} above the transition. Note that these domains behave as stable equilibrium structures, with individual regions growing, shrinking, and changing shape over the course of each trajectory without apparent growth in average domain size.

Finally we compare results with the experiments by Ramsteiner et al.[138] Experimental images of sedimented silica microspheres (Pe=7) taken after 6 hours of equilibration show less order than the simulation model with Pe =6 at the same overall particle loadings. Figure 2 from ref[[138]] shows grains of the order of 10s of particle diameters in dimension in the base layer at a loading of N/A=4.2 σ^{-2} (η_{tot}=3.3). Domains in the second layer are well correlated with those in the base

layer, without evidence of the competition between dual lattices highlighted here in Fig. 5.9. The third layer shows little hexagonal order until higher loadings of $N/A = 4.9\ \sigma^{-2}$ and $5.3\ \sigma^{-2}$. In the present simulations at Pe=6, at η_{tot}=3.23 the base layer (Fig. 5.10(c)) and second layer (data not shown) are monocrystalline while the third layer shows both HCP-like and FCC-like packing patterns,[155, 156] which are easily visualized in Fig. 5.10 by displaying only the first and third layers and noting where they coincide (ABA packing pattern characteristic of HCP) or are offset (ABC packing pattern characteristic of FCC). The boundaries between the domains in the third layer sometimes take the form of a double row of particles arranged as a row of squares; this feature be seen both in Fig. 5.10 in the present study and in Fig. 2 from ref[[138]] at a higher particle loading of $N/A = 5.3\ \sigma^{-2}$. Discrepancies between simulation and experiment could arise from kinetic trapping of defects, from polydispersity or anisotropy effects in the real particles, or from periodic boundary artifacts in the simulations. Further simulation studies incorporating more realistic dynamics along with equilibrium properties in direct comparison with experiment will be needed to clarify the origins of these discrepancies.

5.4 Conclusions

Grand canonical Monte Carlo simulations of hard spheres confined by gravity on a flat hard surface have been carried out over a range of conditions to characterize how the 2-d ordering transition evolves when height fluctuations and overlayer effects are introduced. We have demonstrated that between Pe=18 and Pe=16, the transition shifts rapidly from a slightly perturbed 2-d ordering with a sparsely populated overlayer to a transition with a nearly 50% occupied second layer. Effects from the overlayer are complex, in that it is both a source of pressure to the base layer, favouring ordered dense packing structure, and a source of stabilization for defect sites in

the base layer. The latter effect is clearly evident from the tendency of overlayer particles to segregate towards grain boundaries in a bicrystalline model system. As the second layer is even more fully formed at the transition for lower Pe, its influence reverts to more of a mean-field blanket from above, but then becomes again involved in simultaneous ordering with the base layer below Pe=10.

In principle, the large shift in behaviour between Pe=18 and Pe=16 could be controllable in experimental systems through modest variations in solvent density or centrifugal strength. On the other hand, polydispersity will mean that particles spanning a range of Péclet numbers are likely to be present; the difference in particle diameters between Pe=18 and Pe=16 is less than 3%. This polydispersity could blunt the impact of these sharp changes, but may also introduce other phenomena of interest, and will be a topic of interest for future studies using well-established Monte Carlo methods.[157, 158]

Chapter 6

Gibbs Ensemble Monte Carlo with Solvent Repacking: Phase Coexistence of Size-asymmetrical Binary Lennard-Jones Mixtures[4]

We describe a Monte Carlo method for simulation of vapor-liquid phase coexistence in size-asymmetrical Lennard-Jones (LJ) binary mixtures. The method incorporates the Solvent Repacking Monte Carlo (SRMC) approach, which offers efficient trial moves for the exchange of a large particle for several small particles, into the Gibbs Ensemble Monte Carlo (GEMC) method. SRMC yields a significant efficiency improvement in simulation of dilute large species mixtures at low temperature compared to the original Gibbs ensemble Monte Carlo method with identity exchange (IE) moves. Vapor-liquid phase diagrams are reported for LJ mixtures with a diameter ratio σ_{SS}:σ_{LL} of 1:2 with well-depth ratios ϵ_{SS}:ϵ_{LL} = 1.2, 1.5 and 2, producing spindle-type, azeotrope, and closed loop types of phase diagram, respectively.

6.1 Introduction

Phase diagrams of mixtures have intrigued the interest of scientific community for decades due to their importance in vapor-liquid distillation, supercritical extraction, and related industrial processes. Work on generating phase diagrams for mixtures of Lennard-Jones (LJ) fluids using various theoretical approaches has spanned several decades.[59-67] Size asymmetrical mixtures are studied by Gibbs Ensemble Monte Carlo (GEMC),[63, 68] Grand Canonical Ensemble Monte Carlo

4. Adapted from an article published by Taylor & Francis in *Molecular Simulation* on Sep 11 2017, available online https://www.tandfonline.com/doi/abs/10.1080/08927022.2017.1373192

(GCMC) method[69, 70] or other simulation strategies.[71-73] Complete phase diagrams of binary LJ mixtures were reported by Hall *et al*.[73, 75] through Monte Carlo (MC) simulation and the Gibbs-Duhem integration method[76]. The first-order phase transition for binary mixtures has been calculated by the semigrand canonical ensemble method as well.[77] Calculations using the Redlich-Kwong equation of state show the phase diagrams for molecules of unequal sizes are topologically different from similar size molecules.[78] However, most research focuses on the LJ mixtures that have different well depth ϵ but with size ratios close to 1.

The development of the GEMC method by Panagiotopoulos facilitated the study of phase coexistence of mixtures.[159] Given the proper initial set up, the system can tune itself to produce a phase coexistence point. Due to these attributes of GEMC, it has broad applications in molecular simulations of phase equilibria[160, 161] including simulations of vapor-liquid coexistence in size-asymmetrical mixtures.[63] For asymmetrical mixtures, a trial move that can exchange the identity of different species is included in addition to the displacement move, volume exchange, and small particle swap moves. In practice, however, this GEMC method with identity exchange (IE) suffers from the low acceptance probabilities in simulations of dense systems at low temperature, especially when we want to insert a large particle into the space occupied by a large number of small particles.

The success of modified Gibbs ensemble Monte Carlo with IE moves depends on the existence of small particles that occupy cavities spacious enough to fit a large particle. These environments become vanishingly rare with increasing size ratio or with increasing density of the small particle in the liquid phase. The case of large size ratios and low small-particle density has been explored using innovative methods. Phase diagrams of highly size-asymmetric mixtures (with a 10:1 diameter ratio) in which the small component is not strongly attractive and is present at low (5%)

volume fraction have been successfully studied[93, 162] through restricted GEMC simulation coupled with the highly efficient, rejection-free geometric cluster algorithm (GCA).[94] The effectiveness of the GCA algorithm is limited, however, to a maximum small-particle volume fractions of about 0.34.[95] A multicanonical staged insertion method has also been applied successfully to the same system;[69] it also becomes more expensive with increasing small-particle volume fraction, as it relies for its efficiency on rapid grand-canonical sampling of the small particles, and could face bottlenecks associated with cavity wetting/dewetting transitions of strongly attractive small particles as repulsions from the large particle are gradually turned off or on.

Here we will show that incorporation into GEMC of the Solvent Repacking Monte Carlo (SRMC) method,[8] which offers the possibility of exchanging a variable number of small particles for a single large particle, can facilitate simulations in which the large species is effectively dissolved in an excess of the small species. The SRMC method is based on the Configuration bias Monte Carlo (CBMC) algorithm,[2] which was originally developed to perform efficient trial moves for segmented chain structures in dense environments. The basic idea for CBMC is to generate multiple possible positions for each segment, and only one is chosen based on their Boltzmann weights, biasing the positions of early segments toward lower-energy positions. When the trial steps reach the end of the segmented chain, the entire new chain configuration is accepted or rejected based on an acceptance probability that accounts for the biasing. CBMC has been commonly used in conjunction with the Gibbs Ensemble to improve acceptance probabilities for exchange of single, multisite particles between boxes.[161]

In only a few cases has the CBMC approach been applied to generate configurations for multiple independent particles, because these cases can generally be treated efficiently using single-particle moves. In one case it was used to reposition small particles during large particle

displacements in a size-asymmetric mixture.[163] Exchange of one particle with multiple particles of a different type has also been used in CBMC/GEMC simulations of mixtures of hard spheres with infinitely thin needles.[164] In a study by Wijmans *et al*.,[165] polymer chains in solution could be exchanged very efficiently across GEMC boxes using a 1:1 exchange of polymer segments for solvent particles without changing the coordinates of either; CBMC sampling was used to select which solvent particles would be linked together into a chain. This relies on a similarity in interaction potentials between solvent and monomer particles. SRMC is distinguished by two innovations that are intended to address the challenge of generating a new arrangement of small particles to fill the cavity left by the large: the flexibility to exchange a variable number of small particles for a single large particle (depending on the microenvironment and the system state) and the use of an auxiliary potential to improve the chance of generating a well-packed solvent arrangement in the cavity. In the present system, we find that the auxiliary potential was not helpful, in contrast to its usefulness in a GCMC study of the fluid/ordered transition in bidisperse hard disk systems.[8]

In the present work, we implement SRMC on three-dimensional Gibbs ensemble systems with a continuous interaction potential and study the phase behaviors for several mixtures. In cases where large particle has a greater attractive energy than the small particle, then this would describe a dilute solution of a non-volatile solute, which is not very interesting. Here, we consider the opposite case, $\epsilon_{SS} > \epsilon_{LL}$, where the pairwise attraction energy between small particles, ϵ_{SS}, is greater than that between large particles, ϵ_{LL}. As far as we know, the phase behavior of these LJ systems have not been simulated before. After confirming that our SRMC can reproduce the gas/liquid coexistence boundaries of LJ fluid mixtures previously reported in literature, we apply it to study the phase diagrams of LJ binary mixtures that have a 2:1 size ratios under different

large/small particle ϵ ratios (1:1.2, 1:1.5 and 1:2) at a temperature of $0.75\epsilon_{SS}k_B$. The efficiency analysis shows that the SRMC method is a useful complement to the simple IE move, allowing for reasonable success rates under conditions when the IE move fails, specifically at low liquid phase fractions of the large species and at low temperature.

6.2 Methods

In this section, the acceptance probabilities of Gibbs ensemble SRMC moves will be derived. A similar method in grand canonical ensemble is described in the paper of SRMC on hard disk mixtures.[8]

6.2.1 Gibbs ensemble SRMC algorithm

In our new Gibbs ensemble Monte Carlo with solvent repacking, regular translation move and volume exchange move will be performed as well as the single particle swap for small species. To equilibrate the number of large particles across the two boxes, a large particle is exchanged for zero, one, or (usually) more small particles as shown schematically in Fig. 6.1.

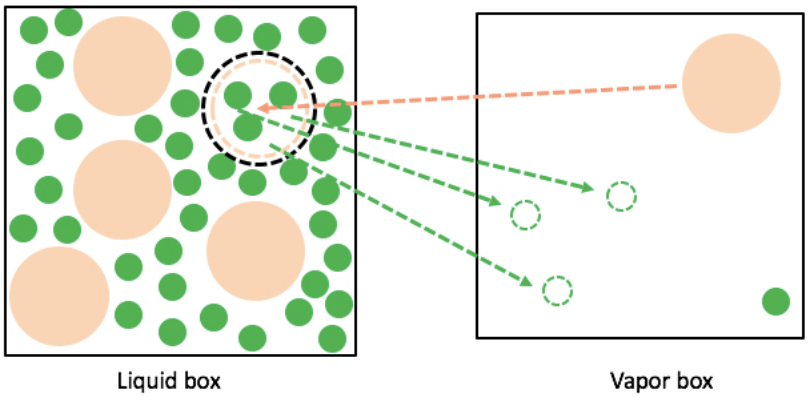

Fig. 6.1 Scheme of SRMC in Gibbs ensemble: Insertion of a large particle in liquid box by SRMC, while using simple insertions to add multiple small species in vapor box.

The scheme of original solvent repacking move in hard-disk system is shown in Fig. 1 of reference[8]. First, a box for the large species to be removed from, one of the large particles it contains, and its new trial position in the other box are selected at random. If the liquid ("f" is used as indicator of liquid box in equations) box (defined as the box with the greater density, which in the present simulations is always unambiguous) is chosen, then a cavity is defined as the spherical volume within a distance of $1.38\sigma_{SS}$, which is justified in section *6.3.1.2* below, from the position of the large particle. If any small particles are present within this cavity (very unlikely due to repulsion from the large particle) the move is rejected. Otherwise, over a series of cycles indexed by i, which is also the index of the particle to be inserted, a number k of random positions that uniformly sample the space of the "cavity" will be generated. For each position j out of these k positions, the potential energy $u_{i,j}$ is calculated as the sum of the interactions with particles outside the cavity and the particles inserted in previous cycles ($i' < i$). In each cycle, one of the k positions is selected as the ith particle for the new trial set based on the probability of choosing position j',

$$P_{i,j'} = \frac{\exp\left(-\beta u_{i,j'}\right)}{\sum_{j=1}^{k} \exp\left(-\beta u_{i,j}\right)} \tag{6.2.1}$$

After selecting one as the ith particle in the new configuration set, we can proceed to the next cycles, increasing i by one. (In a previous study for hard disk system, an auxiliary potential was used to improve the acceptance probabilities of SRMC. However, as discussed in section *6.3.1.3*, an auxiliary potential is not used here because it was not found to improve the acceptance probabilities.)

To determine how many small species are inserted into the cavity during repacking, we define a weight associated with each state that has i particles inserted:

$$\omega_i = \frac{v_{cav}^i}{i!k^i} W_i \frac{N_{sg}!}{(N_{sg}-i)!} \frac{1}{V_g^i} \tag{6.2.2}$$

where v_{cav} is the volume of the cavity, N_{sg} is the number of small species in vapor box, V_g is the volume of the vapor box. W is the Rosenbluth weight, which can be defined as

$$W_i = \prod_{i'=1}^{i} \sum_{j=1}^{k} \exp\left(-\beta u_{i',j}\right) \tag{6.2.3}$$

Cycles generating new particle positions are continued until W_i falls below a predetermined value (here set equal to 100). The maximum number that will then be considered, n_{max}, is set to be 1 fewer. The weight ω_i is used to select which value of $i' \in [0, n_{max}]$ will represent the number of particles to be actually inserted into the cavity. The i' small particles to be removed from the vapor box are selected at random. For reverse move that goes from a new configuration to an old one, if the sum of the Boltzmann weights is smaller than $W_{cut} = 100$ but we still have particles from the old configuration that need to be inserted, this entire SRMC move will be terminated immediately to preserve detailed balance.

The probabilities of generating a specific trial move to remove a large species from liquid box(f) to insert it into vapor box(g) is:

$$\alpha_{f\to g} = \frac{1}{N_{Lf}} \frac{\omega_{new}}{\sum_{i'=0}^{n_{max}} \omega_{new,i'}} \frac{n_{cav}!}{v_{cav}^{n_{cav}}} \left(\prod_{i=1}^{n_{cav}} k_i P_{i,j',new}\right) \frac{1}{V_g} \frac{(N_{sg}-n_{cav})!}{N_{sg}!} n_{cav}! \tag{6.2.4}$$

For its reversal, to transfer that large species from vapor box to liquid box is:

$$\alpha_{g\to f} = \frac{1}{V_f}\frac{1}{N_{Lg}+1}\frac{n_{cav}!}{V_g^{n_{cav}}} \tag{6.2.5}$$

where N_{Lf} is the number of large species in liquid box, N_{Lg} is the number of large species in vapor box, V_f is the volume of the the liquid box.

An acceptance probability satisfying detailed balance can be derived as:

$$acc = \frac{\alpha_{g\to f}}{\alpha_{f\to g}}\exp\left[-\beta\left(U_{f,new} - U_{f,old} + U_{g,new} - U_{g,old}\right)\right]$$

$$= \frac{V_g N_{Lf}\sum_{i'=0}^{n_{max}}\omega_{new,i'}}{V_f(N_{Lg}+1)}\frac{\exp\left(-\beta U_{Lg,new}\right)}{\exp\left(-\beta U_{Lf,old}\right)\exp\left(-\beta U_{Sg,old}\right)} \tag{6.2.6}$$

where U is the potential energy of liquid box or vapor box in new configuration (after transferring a large species from liquid box to vapor box) or old configuration.

If the vapor box is selected for removal of large species, a random position for the cavity will be generated to insert the large species in the liquid box. Meanwhile, a number i' of small species in that cavity region will be moved to randomly selected positions in the vapor box. The probability of the reverse move, which is the move to insert i' small species back to the cavity in the liquid box by SRMC, will be calculated by sampling of "dummy" positions to calculate the appropriate Rosenbluth weights W_i. The acceptance rule can be derived using the same method as removing a large species from the vapor box:

$$acc = \frac{\alpha_{f\to g}}{\alpha_{g\to f}}\exp\left[-\beta\left(U_{f,new} - U_{f,old} + U_{g,new} - U_{g,old}\right)\right]$$

$$= \frac{V_f N_{Lg}}{V_g(N_{Lf}+1)\sum_{i'=0}^{n_{max}}\omega_{old,i'}}\frac{\exp\left(-\beta U_{Lf,new}\right)\exp\left(-\beta U_{Sg,new}\right)}{\exp\left(-\beta U_{Lg,old}\right)} \tag{6.2.7}$$

6.2.2 Implementation details

Pairs of particles interact via the Lennard-Jones potential:

$$\Phi_{ij}(r) = 4\epsilon_{ij}[\left(\frac{\sigma_{ij}}{r}\right)^{12} - \left(\frac{\sigma_{ij}}{r}\right)^{6}] \quad (6.2.8)$$

The following mixing rule is applied when calculate the cross term of potential energy: $\sigma_{SL} = (\sigma_{SS} + \sigma_{LL})/2$, $\epsilon_{SL} = \sqrt{\epsilon_{SS}\epsilon_{LL}}$. The shifted potential Φ is used in all simulations:

$$\Phi_{\alpha}(r) = \frac{1}{r^{\alpha}} - \frac{A}{3}\left(r - r_{shift}\right)^{3} - \frac{B}{4}\left(r - r_{shift}\right)^{4} - C; (r_{shift} \le r \le r_{cut}) \quad (6.2.9)$$

$$\Phi_{\alpha}(r) = \frac{1}{r^{\alpha}} - C; (r \le r_{shift}) \quad (6.2.10)$$

where the parameters A, B and C can be calculated as:

$$A = \frac{\alpha[(\alpha+1)r_{shift} - (\alpha+4)r_{cut}]}{r_{cut}^{(\alpha+2)}\left(r_{cut} - r_{shift}\right)^{2}} \quad (6.2.11)$$

$$B = \frac{\alpha[(\alpha+1)r_{shift} - (\alpha+3)r_{cut}]}{r_{cut}^{(\alpha+2)}\left(r_{cut} - r_{shift}\right)^{3}} \quad (6.2.12)$$

$$C = \frac{1}{r_{cut}^{\alpha}} - \frac{A}{3}\left(r_{cut} - r_{shift}\right)^{3} - \frac{B}{4}\left(r_{cut} - r_{shift}\right)^{4} \quad (6.2.13)$$

where α represents the power of the respective LJ terms (6 or 12). Shifted potentials enable the potential and force to continuously and smoothly decay to zero between $r_{shift} = 3\sigma$ and the cut-off distance $r_{cut} = 4\sigma$, and were useful for cross-checking our Monte Carlo codes with results from molecular dynamics simulations (not shown). In our study, different r_{shift} and r_{cut} are used for three interactions (two interactions among small and large, one cross term of interaction).

We employed periodic boundary conditions with long-range corrections to approximate infinite thermodynamic properties of systems with finite size systems, which will give us the phase diagrams and thermodynamics properties reflecting a true LJ fluid. The following functions for pressure and potential energy are added to the mean values used or extracted from simulations as mean-field corrections for the long-ranged contributions of the LJ potential that are neglected in simulations due to truncation[166]:

$$p_{lrc} = \frac{32}{9}\pi\rho_S^2\left(r_{cut}(SS)^{-9} - \frac{3}{2}r_{cut}(SS)^{-3}\right) + \frac{32}{9}\pi\rho_L^2\left(r_{cut}(LL)^{-9} - \frac{3}{2}r_{cut}(LL)^{-3}\right) + \frac{64}{9}\pi\rho_S\rho_L\left(r_{cut}(SL)^{-9} - \frac{3}{2}r_{cut}(SL)^{-3}\right) \quad (6.2.14)$$

$$u_{lrc} = \frac{8}{9}\pi N_S\rho_S\left(r_{cut}(SS)^{-9} - 3r_{cut}(SS)^{-3}\right) + \frac{8}{9}\pi N_L\rho_L\left(r_{cut}(LL)^{-9} - 3r_{cut}(LL)^{-3}\right) + \frac{16}{9}\pi N_S\rho_L\left(r_{cut}(SL)^{-9} - 3r_{cut}(SL)^{-3}\right) \quad (6.2.15)$$

The equilibration and production periods each consisted of at least 2×10^5 MC moves. In our SRMC Gibbs ensemble simulations, the type of MC move was selected randomly according to the following ratios: 1(consisted of 1000 single particle swap cycles):5(SRMC):1(volume exchange). In Gibbs ensemble simulations with IE used to make the performance comparison, the type of MC moves has a ratio: 1(consisted of 1000 single particle swap cycles):5(consisted of 600 IE moves):1(volume exchange). In both cases, each move was followed by 100 translation moves for small and large species, respectively. The only difference is we replaced 1 SRMC move with 600 IE moves, because we found the CPU time for one SRMC is approximately equal to 600 IE moves. The diameters of the cavities are fixed at $2.76\sigma_{SS}$. Multiple insertions ($k = 500$) are used in SRMC moves. The maximum distance for translation move is set to $0.05\sigma_{SS}$ and $0.01\sigma_{SS}$ for small and large species, respectively. The maximum volume change is set to $0.1\sigma_{SS}^3$. Error bars in the following phase diagrams are generated by block averaging.

6.3 Results and Discussion

In this section, we first present the different strategies used to optimize our new SRMC method. Then, the vapor-liquid phase transition of LJ fluid mixtures is demonstrated and compared with literature results to validate our SRMC method. The applications to binary mixtures under different ratios of ϵ at a low temperature is described and performance analysis is reported to show capability and efficiency enhancement of SRMC in simulations of dilute large species fluids.

6.3.1 Optimization of SRMC

In order to get the best performance, we optimized our SRMC from the following approaches: the number of random trial position k, cavity size, and use of auxiliary bias potential function.

6.3.1.1 Optimization of k

The number of random trial positions k affects both acceptance probability and performance of the SRMC method. A low k will save computational effort but decrease the acceptance rate. Therefore the objective is to find a balance between these two that gives the best performance. To quantify the performance, we define a parameter Suf/hr to characterize the successful large particle swap moves per CPU hour. Fig. 6.2 shows the acceptance probabilities and Suf/hr at different k. The best performance can be obtained in the range $10 < k < 25$. In this work we used a higher value, $k = 500$, which we anticipate would be more appropriate for replacement of even larger particles.

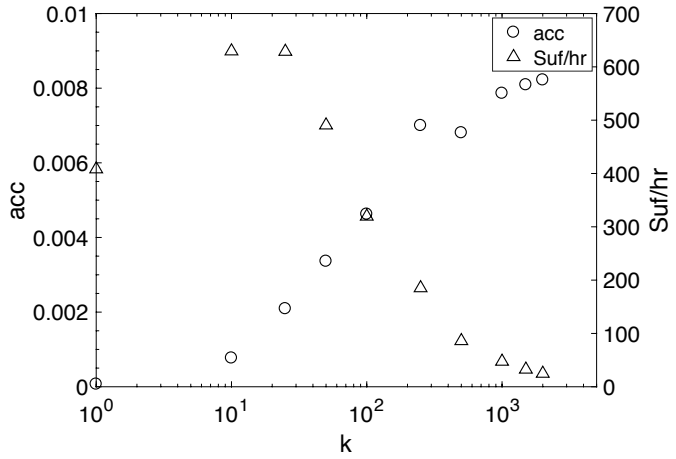

Fig. 6.2 Acceptance probability(*acc*) and performance(*Suf/hr*) of SRMC method at different numbers of random trial positions *k*.

6.3.1.2 Optimization of cavity size

Fig. 6.3 shows the effect of cavity size on acceptance probabilities and performance. Best values can be obtained at cavity radius equal to $1.38\sigma_{SS}$. Due to the 2:1 size ratio, σ_{SL} equals $1.5\sigma_{SS}$. The best cavity radius is therefore slightly smaller than σ_{SL}, so small particle trial positions will lie inside the solvent shell of the large particles.

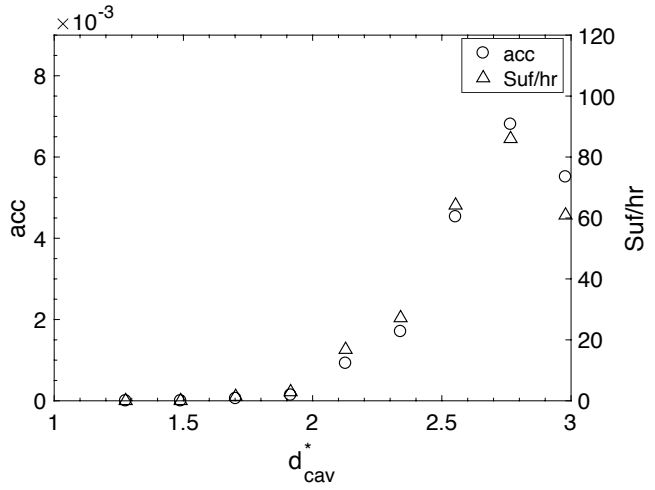

Fig. 6.3 Acceptance probability(*acc*) and performance(*Suf/hr*) of SRMC method at different cavity diameter d_{cav}^{*} (reduced unit is used here: $d_{cav}^{*} = d_{cav}/\sigma_{SS}$).

6.3.1.3 Use of auxiliary bias potential function

Auxiliary bias potential function can be used to improve acceptance probabilities by incorporating many-body effects into the selection of particle positions, accounting in a mean field way for the influence of particles not yet inserted into the cavity. In previous work using the SRMC method, use of the radial distribution function (RDF) as an auxiliary potential ($u_{bias} = \ln g(r)/\beta$) increased the acceptance rate significantly for large size ratio hard disk mixtures.[8] For the 3D LJ mixtures we generated a fit to the difference between LJ potential with RDF using a sum of Gaussian functions (Fig. 6.4). To then determine whether an auxiliary potential improved the acceptance probability of the SRMC method, we introduced a bias potential function $\exp(-\beta u_{bias}) = \exp(-\beta u_{bare}) + \lambda(g(r) - \exp(-\beta u_{bare}))$, where the contribution from the RDF bias potential can be scaled by a parameter λ. By tuning λ from 0 to 1, we can gradually switch our bias potential from full bare potential to full RDF. However, in contrast to 2D hard disk system, using the RDF to bias selection of particle positions does not increase the acceptance probability (Fig. 6.5). It is possible that the RDF does not give a good representation of interparticle distances in the environment of the average cavity left by a large particle, or that the cavities are

too small for incorporation of these effects to be helpful. We tried auxiliary bias potential function at a larger size ratio system (σ_{LL}:σ_{SS} = 2.5:1), but similarly found no increase in acceptance probability.

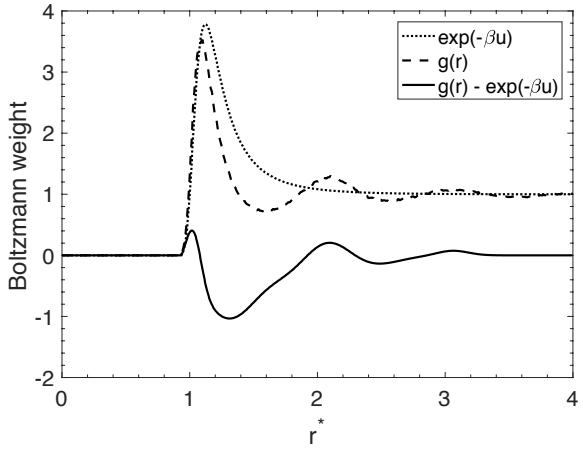

Fig. 6.4 RDF of small species, Boltzmann weight of LJ potential, and difference (fitted by sum of Gaussian).

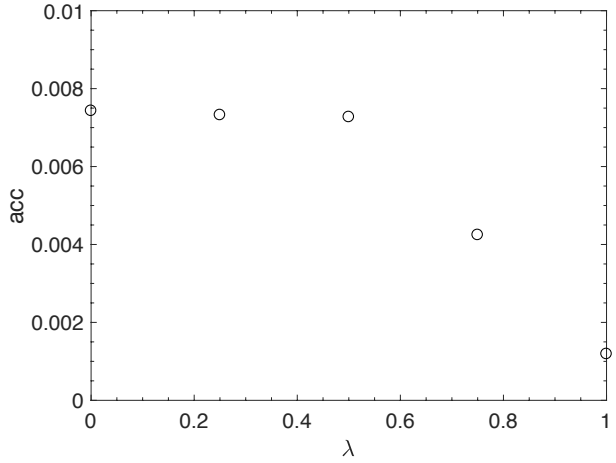

Fig. 6.5 Acceptance probability(*acc*) of SRMC method incorporating auxiliary bias potential scaled by factor λ.

6.3.2 Phase diagram of binary mixtures

The SRMC is applied to studying the phase behavior of LJ binary mixtures with diameter ratios σ_{LL}:σ_{SS} = 2:1. To validate the SRMC-GEMC method, we first applied it to a system with ϵ ratios: ϵ_{LL}: ϵ_{SS}=4:1 at $T^* = 1.0\epsilon_{SS}k_B$. Fig. 6.6 shows the comparison between our SRMC and original

GEMC with IE. Our simulated data has a good agreement with the GEMC data reported in literature [68], which validates our method in the simulation of LJ mixtures. Next, the phase diagrams of 3 LJ systems with size ratio 2:1 at $T^* = 0.75\epsilon_{SS}k_B$ are shown in Fig. 6.7, Fig. 6.8 and Fig. 6.9. $x(L)$, $y(L)$ denotes the the mole fraction of large species in liquid phase and vapor phase, respectively. As ϵ_{LL} is decreased, there is a shift in vapor phase enrichment from small species to large species across different systems, listed in Table 6.1.[74] It can be explained by the balance between ϵ and number of neighbors for certain particle. When the attractive energies of both species are similar (as in 1:1.2 ratio, Fig. 6.7), large particles are preferentially retained in the liquid phase they have more neighbors to attract them, even if the average energy of attraction is slightly lower. After decreasing the ϵ_{LL} (Fig. 6.8, and Fig. 6.9), the stronger attractions of small species become more important than their smaller number of neighbors, which make large species more likely to escape to the vapor phase. The phase diagram of ϵ ratio 1:1.5 (Fig. 6.8) shows an azeotrope point at large species fraction near 0.75. When large species fraction is smaller than 0.75, large particles are over-represented in the vapor phase, while in high large species concentration mixtures($x(L) > 0.75$), the small species is a little bit enriched in vapor phase. Trends in coordination numbers of large and small species (Table 6.1) might shed light on this behavior. The crossover seems to coincide with the transition from small particles having mostly small neighbors, allowing for the strongest neighbor bonding in the system, to having mostly large neighbors, where the number of large neighbors surrounding a small particle is limited by steric factors. For the ϵ ratio 1:2, the phase diagrams demonstrate a closed circle because the temperature is higher than the critical point of the large species.

Table 6.1 Number of neighbors at different large species fractions for system σ_{LL}:σ_{SS} = 2:1, ϵ_{LL}: ϵ_{SS}=1:1.5, T^*= 0.75.

$x(L)$	nLL^a	nSS	nLS	nSL
0		12.78		
0.0135	0.95	12.05	24.05	0.33
0.0576	3.14	10.47	18.62	1.14
0.3167	7.47	5.06	8.15	3.77
0.5779	10.70	3.10	4.38	6.01
0.7489	10.67	1.62	2.30	6.82
0.8321	10.64	0.78	1.35	6.70
0.9161	10.51	0.24	0.62	6.75
1	10.36			

[a]The first letter denotes the center particle while the second letter denotes its neighbors. The cut-off for a neighbor is defined at 1:5σ_{SS} for *nSS*, 3:1σ_{SS} for *nLL*, 2:1σ_{SS} for *nLS* and *nSL*, respectively.

Fig. 6.10 shows a partial phase diagram for size ratio σ_{LL}:σ_{SS} =2.5:1 with ϵ_{LL}: ϵ_{SS}=1:1.5, which demonstrate the applicability of SRMC to a larger size ratio. However, increasing the size ratio to 3:1 resulted in a too low acceptance probability that prevented us from achieving equilibrium in a reasonable simulation time.

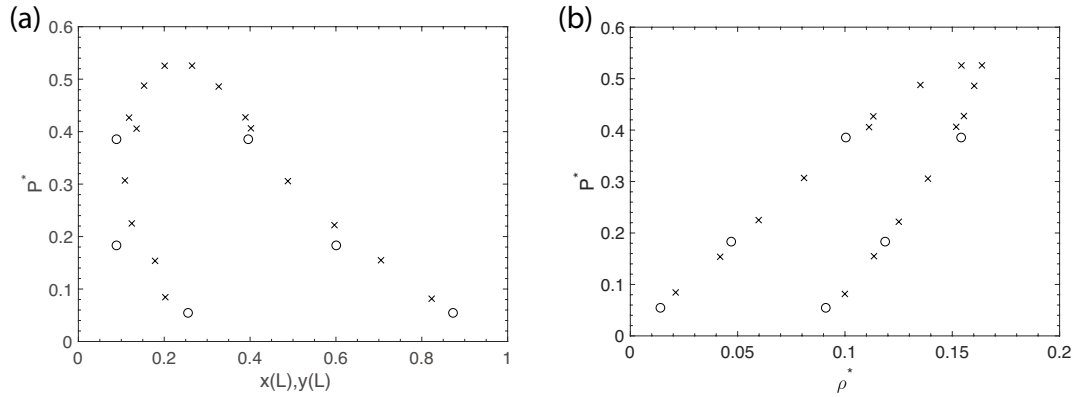

Fig. 6.6 Reduced pressure vs. mole fraction (a) and reduced density (b) for system (σ_{LL}:σ_{SS} = 2:1, ϵ_{LL}: ϵ_{SS}=4:1, T^*= 1.0): SRMC results (circle); literature data [68] (cross).

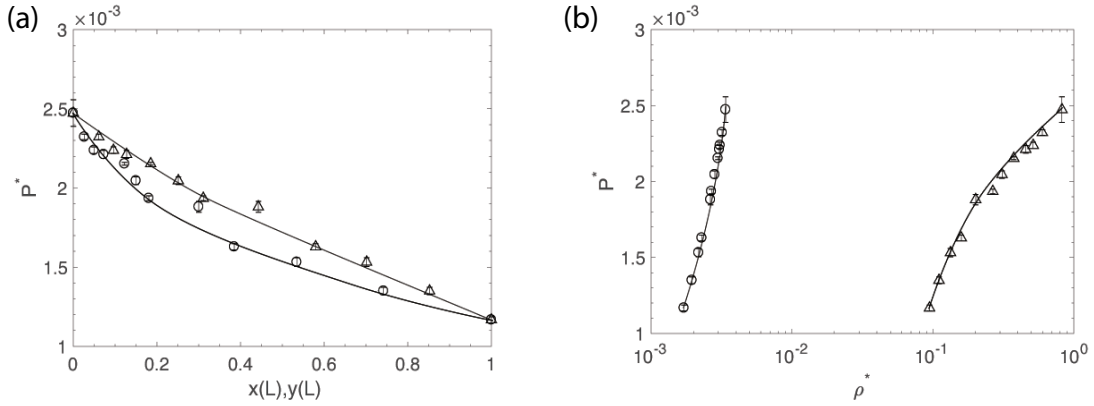

Fig. 6.7 Reduced pressure vs. mole fraction (a) and reduced density (b) for system (σ_{LL}:σ_{SS} = 2:1, ϵ_{LL}: ϵ_{SS}=1:1.2, T^*= 0.75). Lines on the phase boundaries are drawn only as a guide to the eye. Triangle indicates the liquid phase boundary, and circle indicates the vapor phase boundary.

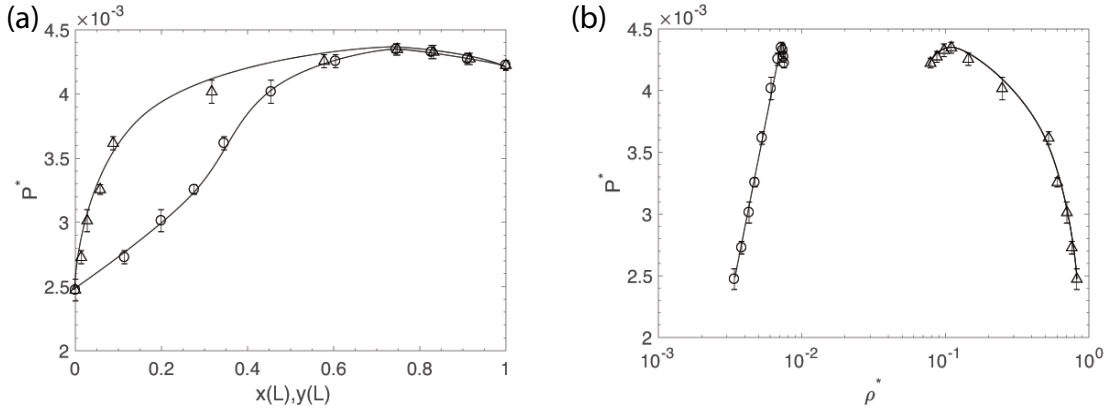

Fig. 6.8 Reduced pressure vs. mole fraction (a) and reduced density (b) for system (σ_{LL}:σ_{SS} = 2:1, ϵ_{LL}: ϵ_{SS}=1:1.5, T^*= 0.75). Lines on the phase boundaries are drawn only as a guide to the eye. Triangle indicates the liquid phase boundary, and circle indicates the vapor phase boundary.

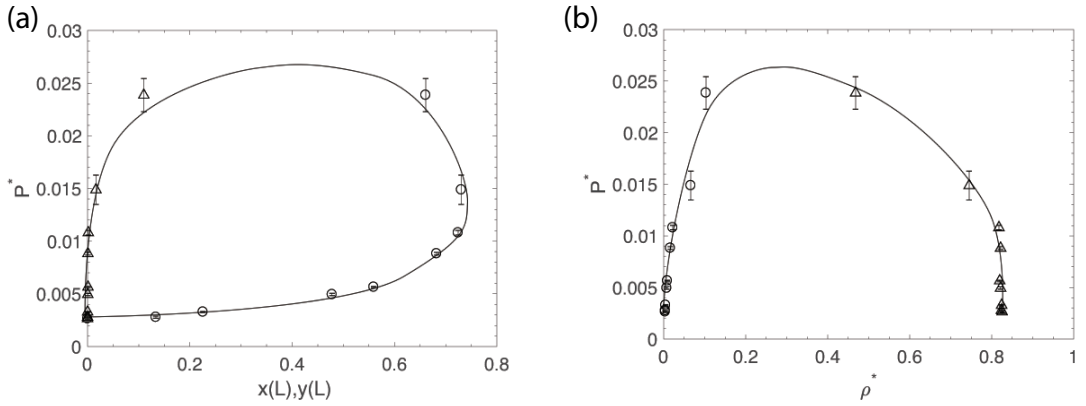

Fig. 6.9 Reduced pressure vs. mole fraction (a) and reduced density (b) for system (σ_{LL}:σ_{SS} = 2:1, ϵ_{LL}: ϵ_{SS}=1:2, T^*= 0.75). Lines on the phase boundaries are drawn only as a guide to the eye. Triangle indicates the liquid phase boundary, and circle indicates the vapor phase boundary.

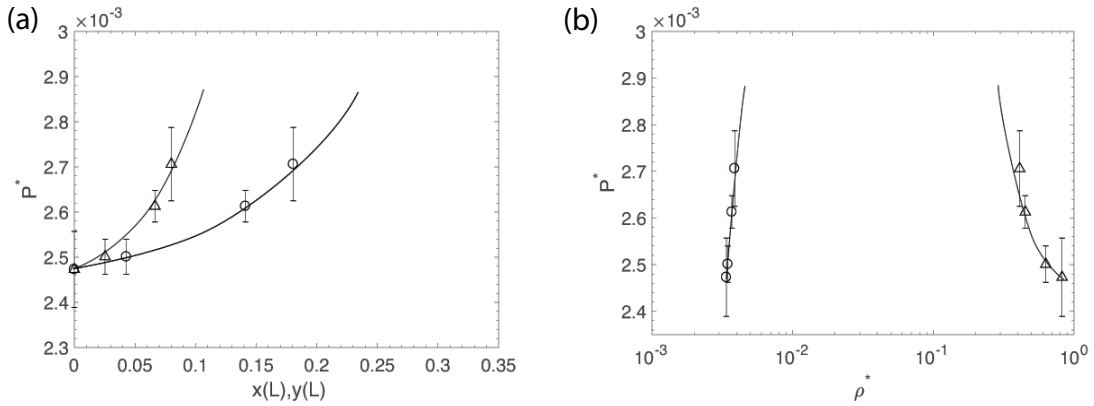

Fig. 6.10 Reduced pressure vs. mole fraction (a) and reduced density (b) for system (σ_{LL}:σ_{SS} = 2.5:1, ϵ_{LL}: ϵ_{SS}=1:1.5, T^*= 0.75). Lines on the phase boundaries are drawn only as a guide to the eye. Triangle indicates the liquid phase boundary, and circle indicates the vapor phase boundary. Only dilute large species part is shown in this diagram.

6.3.3 Performance Comparison between SRMC with identity exchange swap method

Table 6.2 compares the performances (Suf/hr), measured in successful large particle swaps per hour, of SRMC and the IE method in Gibbs ensemble at different large species mole fractions($x(L)$) in the liquid phase. We tracked the number fluctuations of large particles achieved using different methods versus CPU time. Clearly, SRMC can swap the large species more frequently than simple IE move (as shown in Fig. 6.11), which allows few or no successful swaps in a dilute large species environment. The reason why the original IE method failed in this regime is due to the increasing difficulty finding the free volume to fit a large particle size increase in IE

in a very dense phase consisting of a large amount of small species. In contrast, SRMC can swap large species into dense environment in exchange for multiple small particles, allowing access the phase properties of dilute large species mixtures. We note that the IE method is more efficient when the large species is not dilute. We plot Suf/hr versus the large species fraction in liquid phase to compare the performances of the two methods (Fig. 6.12, Fig. 6.13, and Fig. 6.14), and see a crossover from conditions where SRMC is more efficient to where single IE is preferable as the mole fraction of large particles increases. The crossover takes place near a mole fraction $x(L)$ of 50% at ϵ ratios 1:1.2 and 1:1.5, but at much lower fraction for the ϵ ratio 1:2 case. In that case, the increase in large particle content brings the coexisting phases near a critical point, with the density of the liquid phase falling while the density of the gas phase rises. The decrease in density of the liquid phase helps the simple IE move while the increase in density of the gas phase hurts the SRMC move, which in the present implementation involves multiple unbiased insertions of the small particles into this dense gas. Incorporating multiple trial positions for insertion into the gas phase could improve performance under these circumstances.

The performance measures are low in absolute terms for a combination of reasons. Our code will achieve 203,000 successful simple small particle swaps per hour on an Intel Xeon E5-2680v3 processor core of the Comet cluster at the San Diego Supercomputer center at $T^* = 1.0$. This rate decreases to 10,800 at $T^* = 0.75$ due to the increased density and decreased temperature. These values reflect the availability of voids, thermally generated within the liquid phase, whose volume is sufficient to insert a small particle. As evident from the values shown in Fig. 6.12, Fig. 6.13 and Fig. 6.14, IE moves in a mixture with a diameter ratio of 2:1 are further suppressed by one or more orders of magnitude (depending on mixture composition) because they require a free volume of approximately the difference between the large and small particle volumes (i.e. seven times the

small particle volume). The solvent repacking approach can avoid this problem by exchanging a large particle for a cluster of solvent with equal volume. The trade-off in computational expense, however, is the challenge of finding a compact, low-energy packing arrangement for multiple solvent particles in the large particle's vacated cavity, requiring many trial positions to be generated per move.

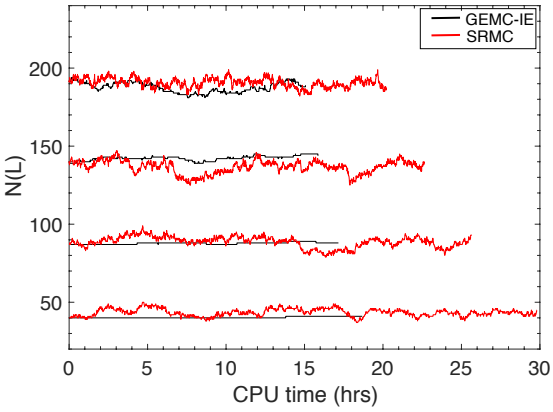

Fig. 6.11 Number of large species in liquid phase simulated by GEMC-IE and SRMC for system (σ_{LL}:σ_{SS} = 2:1, ϵ_{LL}: ϵ_{SS}=1:1.5, T^*= 0.75) at four total system compositions.

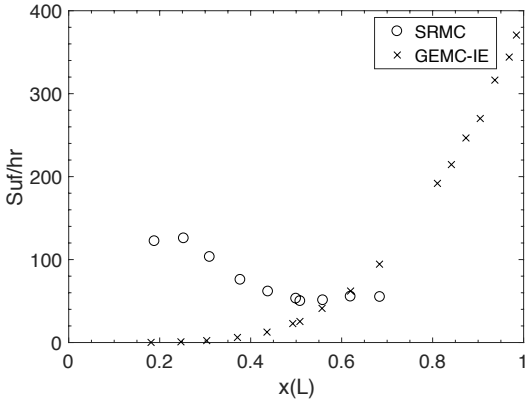

Fig. 6.12 Performance of GEMC-IE and SRMC at different large species fractions (liquid phase) for system (σ_{LL}:σ_{SS} = 2:1, ϵ_{LL}: ϵ_{SS}=1:1.2, T^*=0:75).

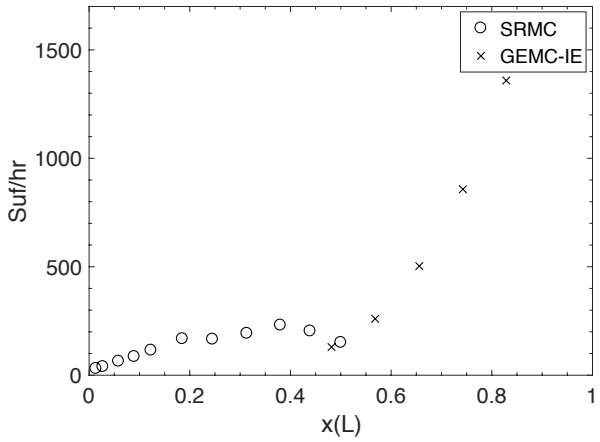

Fig. 6.13 Performance of GEMC-IE and SRMC at different large species fractions (liquid phase) for system (σ_{LL}:σ_{SS} = 2:1, ϵ_{LL}: ϵ_{SS}=1:1.5, T^*=0.75).

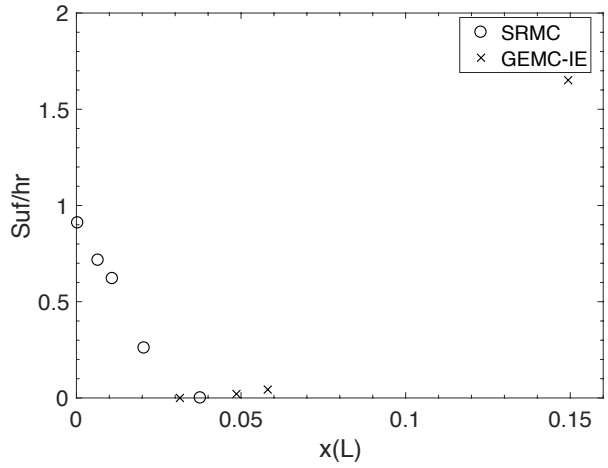

Fig. 6.14 Performance of GEMC-IE and SRMC at different large species fractions (liquid phase) for system (σ_{LL}:σ_{SS} = 2:1, ϵ_{LL}: ϵ_{SS}=1:2, $T^* = 0.75$).

Table 6.2 Performance comparison (as rate of successful large-particle exchanges per CPU-hour, *Suf/hr*) of GEMC-IE and SRMC in dilute large species mixtures.

σ_{LL}: σ_{SS}	ϵ_{LL}: ϵ_{SS}	$x(L)$	*Suf/hr*(GEMC-IE)	*Suf/hr*(SRMC)
2:1	1:1.2	0.0301	0	35.04
2:1	1:1.2	0.0617	0.07	54.87
2:1	1:1.2	0.0970	0.63	80.30

2:1	1:1.2	0.1277	2.22	82.70
2:1	1:1.5	0.0282	0.05	38.01
2:1	1:1.5	0.0576	0.41	63.11
2:1	1:1.5	0.0888	3.78	89.39
2:1	1:1.5	0.1233	16.66	128.27
2:1	1:2	0.0004	0	0.90
2:1	1:2	0.0066	0	0.71
2:1	1:2	0.0109	0	0.62
2:1	1:2	0.0205	0	0.26

6.4 Conclusions

In summary, we implemented the SRMC method for the study of vapor-liquid coexistence of size-asymmetrical binary LJ mixtures. The SRMC can overcome the low acceptance probabilities in traditional GEMC simulations of dilute solute mixtures at low temperature, which offer the exchange of one large particle for several small particles. We have applied our SRMC to phase transition studies of three binary size-asymmetric LJ mixtures with different ϵ ratios, and seen a range of vapor-liquid phase transition behaviors. Further refinements of the SRMC method may enable its application to thermodynamic and phase behavior of more complex fluid systems, including aqueous solutions.

Chapter 7

Size-asymmetrical Lennard-Jones solid solutions: Interstitials and substitutions[5]

We present simulation studies of solid solutions formed upon compression of mixtures of Lennard-Jones (LJ) particles with diameter ratios 2:1 and 3:1. Grand canonical Monte Carlo (GCMC) and Gibbs-Duhem integration were used to determine the compositions of coexisting solid and liquid phases at several pressures and fixed temperature. Concentrations of small particles dissolved in interstitial sites of the large-particle lattice, under liquid-solid coexistence conditions, were determined directly from GCMC simulations. Indirect methods were used to calculate levels of small particles dissolved substitutionally, either singly or in plural, with the average number of small solutes occupying a lattice site vacated by a large particle increasing with higher pressure. In the cases studied, the fraction of small solutes occupying these substitutional sites was found to be small (2% or lower, depending on the mixture and conditions), but to stay roughly constant with increasing pressure. Structural and dynamic characteristics of the solid solutions are described and compared with reported characteristics of the related interstitial solid solution formed by hard spheres.

5. Adapted with permission from Guo, Z. and Kindt, J. T., ***J. Chem. Phys.*** 148, 164504 (2018) with the permission of AIP Publishing.

7.1 Introduction

Solid solutions or alloys, mixtures in which one component is distributed in a disordered arrangement throughout an otherwise regular crystal structure, have been widely studied due to their applications in photonics, optics, semiconductors and structure design[79-83]. In a substitutional solid solution (SSS), impurity particles occupy some fraction of lattice sites in place of the majority component particles; the prototypical example is bronze, which contains tin substituted within a copper lattice. In an interstitial solid solution (ISS) the impurity component occupies some fraction of the interstitial positions of the crystalline lattice of the first species; the prototypical example is steel, with carbon atoms occupying interstitial sites in an iron lattice[84]. The presence of the impurities may have important effects on the mechanical behaviors, phase diagrams, and electrical properties of the solids, and the ability to tune the properties by adjusting the amount and nature of the minority components have made solid solutions tremendously important in technology.

One obvious distinction between substitutional and interstitial localization of impurities is that the former is more likely for impurities that are similar in size to the primary component, while the latter is more likely for impurities that are significantly smaller. It is natural to speculate, then, about whether a dimer or cluster of small impurities can play the role of a large impurity and form plural substitutional defects within a primarily interstitial crystal. Colloidal crystals have been predicted and synthesized in which icosahedral clusters of 13 small "B" spheres occupy sites similar (though not identical) to large "A" spheres[167], although this is a compound with a fixed stoichiometry of AB_{13} and not an alloy. Density functional theory (DFT) calculations suggest that vacancy sites within carbon steel will be occupied by a carbon dimer[168]. Vacancy occupation by one or more impurity particles present interstitially and the equilibrium thermodynamics of vacancy levels has been addressed in the recent metallurgical literature[85], and appears to have

implications for design of advance materials with many thermodynamic and kinetic properties like High Entropy Alloys (HEAs) with much better resistance to radiation damages.

To gain some general perspective on whether interstitial and plural substitutional impurities might appear in the same phase we have investigated size-asymmetrical binary Lennard-Jones (LJ) solid solutions, with the smaller particle the minority component, at coexistence with the binary liquid mixture. The composition at the coexistence point is of interest as represents the highest impurity content that the solid can absorb at a given pressure and temperature without becoming unstable with respect to phase separation.

Binary mixtures of LJ solids have been studied for decades[169-175]. However, only few studies focus on the ISS phase of LJ solids, which treat the species in interstitial places as impurity[176, 177]. There are multiple approaches to study the solid-liquid phase coexistence for LJ systems. Ferreira *et al.* obtained the solid-liquid coexistence by absolute free energy calculations[79]. Gibbs ensemble simulation has been extended to simulate the solid-liquid phase equilibrium by Quirke *et al*[178]. Escobedo *et al.* applied virtual Gibbs ensemble to directly simulate the solid-liquid phase coexistence[179]. A phase-switch Monte Carlo was developed by Errington to investigate the coexistence[180]. Cottin *et al.* studied the phase equilibrium of binary LJ mixtures from a cell theory approach[181]. MD simulation is also used to study the crystal growth in binary LJ mixtures at liquid-solid interfaces[182]. A widely used current method to study the solid-liquid phase equilibrium is Gibbs-Duhem integration developed by Kofke[76, 183]. With the prior knowledge of one coexistence point, one can integrate starting from the existing point using the Clapeyron formula to find the coexistence point at new temperature. Hall *et al.* reported the solid-liquid phase diagram of the binary LJ mixtures in the temperature-composition plane at fixed pressure by Gibbs-Duhem integration with MC simulation[73, 184].

Here, we employ a variation of Gibbs-Duhem integration to track the coexistence points at different pressures with fixed temperature. We start from the coexistence point for a pure large species LJ system whose phase coexistence data is available from the literature[79], then used Gibbs-Duhem integration to get the new coexistence point at higher pressure with some small species present using grand canonical Monte Carlo simulation (GCMC). The solid phases would actually describe an ISS phase in which the large species forms a face centered-cubic (fcc) lattice while the small impurity species primarily occupy the interstices, but may also occupy the main lattice positions either singly or in clusters. Three systems were studied in this work. The mixtures in two cases have the same ϵ but different sizes, with σ ratios 1:2 and 1:3. (system S2 and S3 as shown in Table 7.1). In the third case (system E2 as shown in Table 7.1) the large particles are more strongly attractive than the small component (σ ratio 1:2, ϵ ratio 1:1.5), mirroring the typical trend in experimental systems like neopentane/methane[185]. For all systems, we studied the coexistence points under three pressures (6.0, 8.0 and 10.0 $k_B T/{\sigma_{LL}}^3$) and performed structural analysis on the liquid phase and solid phase. To investigate the substitution behavior by the small components, we created a vacancy in the large-particle lattice manually, and observed the occupation of the vacancy by small particles at the chemical potential determined for the system at coexistence. Using standard approaches to estimate the free energy of vacancy formation[186, 187], we then used the occupation statistics to estimate the concentration of all vacancies (substituted or empty) for each system.

7.2 Methods

7.2.1 Determination of solid-liquid coexistence points

The Gibbs-Duhem integration method is commonly applied to track how the pressure at coexistence between two phases varies with temperature[76], and has also been applied to find the variation of coexisting compositions with changing T (at fixed pressure) in a binary mixture[73]. Here we consider the application of the same strategy while fixing T and varying pressure.

The solid-liquid phase coexistence point of LJ system can be accessed via various methods[79]. With the densities of solid and liquid phases at coexistence at a specified temperature and pressure P_0 obtained from the literature, Grand Canonical Monte Carlo (GCMC) can be used to determine the chemical potential of the liquid state (and by extension, the solid).

Given the Gibbs-Duhem equation:

$$\sum_{i=1}^{I} N_i d\mu_i = -SdT + VdP \tag{7.2.1}$$

variations in pressure and composition in a binary mixture at constant T are related by:

$$dP = \rho_S d\mu_S + \rho_L d\mu_L \tag{7.2.2}$$

where the subscripts designate small (S) and large (L) particles. If we make the approximation that in the solid phase ρ_L is a constant and small particles partition strongly to the liquid phase $\rho_S(solid) \ll \rho_S(liquid)$, the large component's chemical potential at higher pressure $P > P_0$ can be obtained without further information about the small component's behavior:

$$P - P_0 = \rho_L \Delta\mu_L \tag{7.2.3}$$

Substituting the chemical potential as fugacity $f = \exp(\beta\mu)$, with the de Broglie thermal wavelength set to 1, we have:

$$P - P_0 = \rho_L ln \frac{f_L}{f_L^0} \tag{7.2.4}$$

Since the approximations that produce Eq. (7.2.3) and Eq. (7.2.4) are not ultimately satisfied, we rely on these equations for a first approximation only. For each pressure P of interest, the liquid phase is first simulated using GCMC with fixed f_L obtained from Eq. (7.2.4) and varying f_S

to find the value that produces a pressure P in the mixture (Fig. 7.1). In principle, simulation of the solid phase at constant f_S, f_L, and V would produce an equilibrated state whose pressure could be compared with P to test the assumptions made above. However, the rigidity of the lattice structure and the need for the lattice spaces to be commensurate with the periodicity imposed by the simulation box make this unreliable. Instead, the solid phase is simulated by GCMC, either at constant P, N_L, and f_S, or at constant P, f_L and f_S, in which case the kinetic barrier to changing the lattice structure imposes an effective fourth constraint on number of cells in the system. Through the simulations at constant P, f_L and f_S, we saw it is a rare event for solid phase having a vacancy, therefore, for efficiency concern, we manually create a vacancy in crystal structure (remove a large particle in simulation box) and run simulations at constant P, N_L, and f_S to find the small species partition in solid phase (Table 7.1). The manually created vacancy is implemented in all the following results except the discussions on phase diagrams, small species absorption and radial distribution function (RDF). In any case, we cannot rely on particle exchange moves to ensure that the fugacity of large particles in the solid phase is in fact equal to the f_L of Eq. (7.2.4), so we rely again on the Gibbs-Duhem equation.

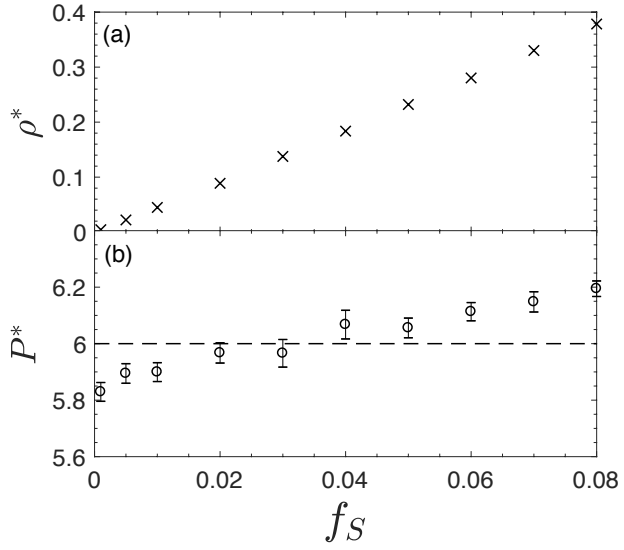

Fig. 7.1 (a) Number density of small species in system S2 (liquid phase) at different small species fugacity f_S (error bar is smaller than the size of the data points); (b) Pressure of system S2 at different small species fugacity f_S at fixed large species fugacity $f_L = 20.9$, showing method of initial approximation of f_S at coexistence.

At fixed pressure, Gibbs-Duhem equation gives:

$$d\mu_L = -\frac{\rho_S}{\rho_L} d\mu_S \tag{7.2.5}$$

Therefore, in order to calculate the $\Delta\mu_L$ to make the correction at μ_L, we need to rewrite $d\mu_S$ first.

We find empirically that ρ_S (in the solid phase, at fixed pressure and N_L) can be related to f_S by the function:

$$\rho_S = \frac{Af_S}{1+Bf_S} = \frac{A\exp(\beta\mu_S)}{1+B\exp(\beta\mu_S)} \tag{7.2.6}$$

in which A and B are two constants.

Differentiating Eq. (7.2.6):

$$\frac{\partial\rho_S}{\partial\mu_S} = \frac{A\beta\exp(\beta\mu_S)}{[1+B\exp(\beta\mu_S)]^2} \tag{7.2.7}$$

So $d\mu_L$ can be rewritten as:

$$d\mu_L = -\frac{\rho_S}{\rho_L} d\mu_S = -\frac{1+B\exp(\beta\mu_S)}{\beta\rho_L} \partial\rho_S \tag{7.2.8}$$

From Eq. (7.2.6), we have:

$$f_S = \exp(\beta\mu_S) = \frac{\rho_S}{A-B\rho_S} \tag{7.2.9}$$

Rewriting Eq. (7.2.8) with Eq. (7.2.9):

$$d\mu_L = -\frac{1+B\frac{\rho_S}{A-B\rho_S}}{\beta\rho_L} \partial\rho_S \tag{7.2.10}$$

Integrating Eq. (7.2.10) yields:

$$\Delta\mu_L = \frac{A}{\beta B\rho_L}[\ln\left(1-\frac{B}{A}\rho_S\right)] \tag{7.2.11}$$

The new corrected (lower) μ_L calculated from Eq. (7.2.11) can then be used in the first step, simulation of the liquid. An increase in the small-particle content of the liquid will then be needed to bring the liquid pressure up to *P*, and the small-particle fugacity in the solid will also increase. This process is repeated until self-consistency is reached.

7.2.2 Implementation details

Pairs of particles interact via the Lennard-Jones potential:

$$\Phi_{ij}(r) = 4\epsilon_{ij}[\left(\frac{\sigma_{ij}}{r}\right)^{12} - \left(\frac{\sigma_{ij}}{r}\right)^{6}] \tag{7.2.12}$$

The following mixing rule is applied when calculating the cross term of potential energy: $\sigma_{SL} = (\sigma_{SS} + \sigma_{LL})/2$, $\epsilon_{SL} = \sqrt{\epsilon_{SS}\epsilon_{LL}}$. The potential is simply truncated at the cutoff distance $r_{cut} = 4\sigma$. Different r_{cut} are used for three interactions (two interactions among small and large, one cross term of interaction). Periodic boundary conditions with long-range corrections are applied.

In the liquid phase, the equilibration and production periods each consisted of at least 10^6 MC cycles for liquid phase. Each MC cycle contains 50 insertion or removal trials for small species and 150 insertion or removal trials for large species. For solid phase, the equilibration and production periods each consisted of at least 5×10^7 single insertion and removal moves. In both phases, each move was followed by 100 translation moves attempts for small and large species, respectively. The initial solid phase is constructed by 864 LJ particles formed into a fcc lattice. The maximum distance for translation move is set to 0.05 σ_{LL} and 0.01 σ_{LL} for small and large species, respectively. The maximum volume change is set to 0.1 σ_{LL}^3 in constant pressure solid phase simulations. Reduced units, scaled to the large species σ_{LL} and ϵ_{LL}, are used in all the data reported in this work, and all simulations are performed at $k_BT = \epsilon_{LL}$=1. VMD was used for molecular graphics[188].

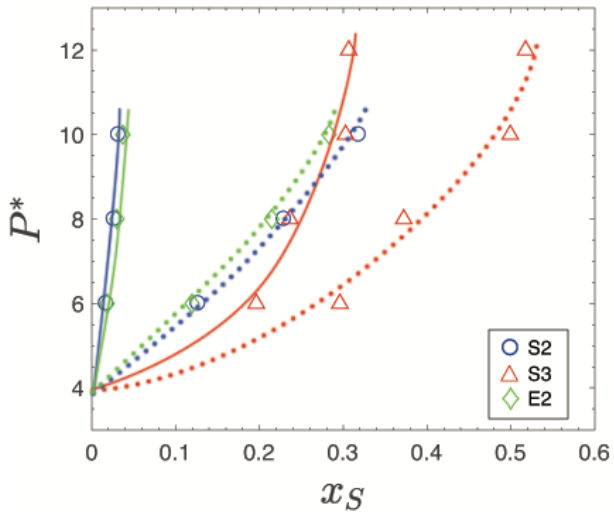

Fig. 7.2 Solid-liquid phase diagram for three systems at mole fraction (small species)- pressure plane. Curves on the phase boundaries are drawn only as guide to the eye. Solid curves represent the solid boundaries (without the vacancy in solid phase), while dotted lines represent the liquid boundaries. Errors are smaller than the scale of data points.

7.3 Results and Discussion

7.3.1 Solid-liquid phase coexistence and interstitial absorption

Compositions of liquid and solid solutions of small particles at coexistence (Fig. 7.2) have been determined for three systems S2, S3 and E2 (Table 7.1) at three pressures using the Gibbs-Duhem integration method described above. The most pronounced difference is that in system S3 (σ ratio 1:3) the solubility of small particles in the solid phase is much greater than in systems S2 or E2 (σ ratio 1:2). The mole fraction of small species in solid phase in system S3 are even comparable to the fractions in liquid phases at coexistence in system S2 and E2. It is interesting to compare this system with the interstitial solid solution of hard spheres (HS) of diameter ratio 0.3:1 studied by Filion and Dijkstra[83]. As in the HS mixture, the small LJ particles primarily occupy octahedral sites in the fcc lattice of the larger particles. Insight into the thermodynamics of absorption into the solid phase can be derived from the variation of fugacity with composition. If the interstitial sites behave as independent single-occupancy sites (as in the Langmuir adsorption isotherm, although this case involves absorption and not adsorption), then the fugacity would increase non-linearly as these sites fill:

$$f = C\,\Theta/(1-\Theta) = C\,x_S/(1-2x_S) \tag{7.3.1}$$

Fig. 7.3 shows that in the case of system S3, the absorption of small particles within the solid follows a more nearly ideal dependence than predicted from the single-occupancy model. In fact, the radial distribution function (Fig. 7.4) for the solid phase mixture of system S3 (and system S2) contains a peak in $g(SS)$ at distances nearer than the nearest small-large neighbor peak, indicating that impurities do in fact pair up within the interstitial sites. This contrasts with the HS case, where the interstitial solid solution was seen to reach a maximum of number ratio of small to large particles of 1:1. (Higher loading of small particles into the HS solid occurred via a first-order

transition to the LS_6 structure where 6 small particles can be found in interstitial sites of a bcc lattice.) The possibility of multiple occupancy in interstitial sites is presumably facilitated by the softer nature of the potential and the attractions between small particles, since reduction in that attraction (system E2) appears to suppress it. We have not accessed high enough pressures to determine whether the interstitial solid solution remains stable up to (or beyond) a mole fraction x_S = 0.5 as was seen in the hard-sphere system[83]; an additional data point at P^*=12 generated for system S3 alone yielded x_S of 0.306 in the solid phase at coexistence (Fig. 7.2).

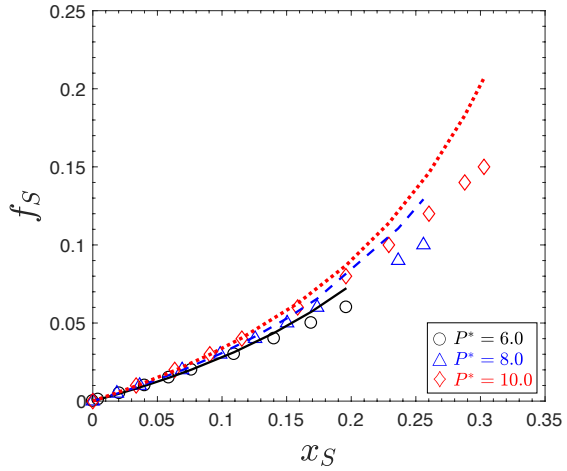

Fig. 7.3 Fugacity of small species at different mole fraction x_S in system S3 (without the vacancy in solid phase) at different pressures. The fugacity of large species is fixed at 16.99, 99.05 and 527.13, for pressure 6.0, 8.0 and 10.0,

respectively. Fitting of data by Langmuir adsorption isotherm are shown in solid, dash, dot lines for pressure 6.0, 8.0 and 10.0, respectively.

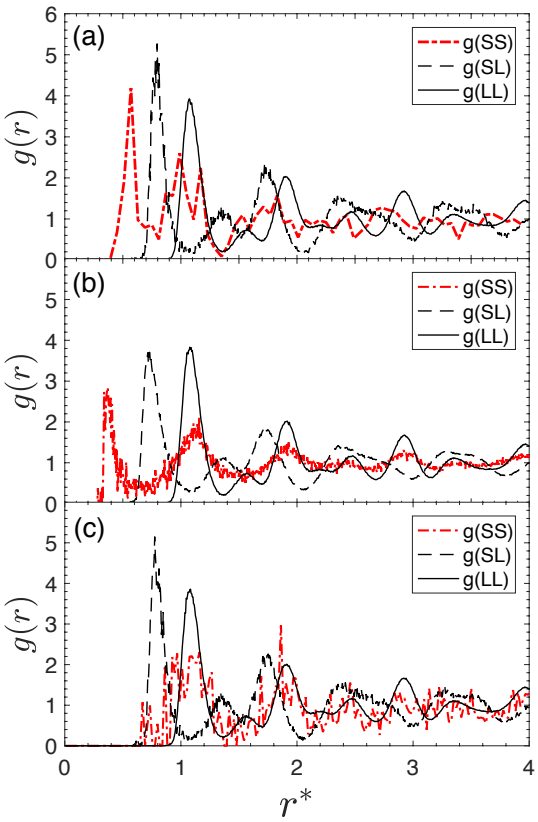

Fig. 7.4 Radial Distribution Function (RDF) in solid phase without the vacancy for system (a) S2, (b) S3 and (c) E2 at pressure 6.0.

The presence of the small particles expands the lattice spacing of the large particles slightly (Table 7.2). Since the lattice spacing change is very small (<1%), it is still reasonable to approximately estimate the vacancy concentration through the method discussed in *7.3.2*. Higher pressure will suppress the lattice spacing in both pure large systems and mixtures (d in Table 7.2); the lattice spacing difference between the mixture and pure large system is bigger at higher pressure (Δd in Table 7.2) due to the presence of more small species in solid solutions.

Table 7.1 Compositions of solid phases under solid-liquid coexistence conditions for different systems with 863 large particles and 1 vacancy. N_S^{sub} is the average number of small particles per vacancy, N_S^{inter} is the average number of small particles per interstitial site.

system	σ_{LL}: σ_{SS}	ϵ_{LL}: ϵ_{SS}	P^*	ρ_S	N_S^{sub}	N_S^{inter}
	2:1	1:1	6.0	0.018	1.58	0.016
S2	2:1	1:1	8.0	0.029	2.65	0.024
	2:1	1:1	10.0	0.036	3.30	0.029
	3:1	1:1	6.0	0.255	1.30	0.246
S3	3:1	1:1	8.0	0.331	2.53	0.310
	3:1	1:1	10.0	0.479	5.04	0.440
	2:1	1.5:1	6.0	0.019	1.40	0.017
E2	2:1	1.5:1	8.0	0.033	2.30	0.028
	2:1	1.5:1	10.0	0.042	2.89	0.035

Table 7.2 Lattice spacing d (defined as the edge length of one fcc unit cell; reduced unit σ_{LL} is used) in different systems; and the expansion Δd observed between the mixtures and pure systems.

P^*	$d_{Pure\ Large}$	d_{S2}	Δd_{S2}	d_{S3}	Δd_{S3}	d_{E2}	Δd_{E2}
6.0	1.5618	1.5643	0.0025	1.5717	0.0099	1.5642	0.0024
8.0	1.5467	1.5505	0.0038	1.5572	0.0105	1.5506	0.0039
10.0	1.5346	1.5388	0.0042	1.5492	0.0146	1.5392	0.0046

7.3.2 Substitutional absorption

Although the small particles appear to favor interstitial sites, we sought to characterize and quantify the substitutional absorption in this system, particularly the possibility of plural substitution, with more than one of the small species occupying a lattice position vacated by a large particle (Fig. 7.5). In simulations initiated with a large particle vacancy defect, the average number of dopants occupying the vacancy at coexistence with the mixed liquid is on average greater than one (Table 7.1). The distribution of occupancy numbers is shown in Fig. 7.6. We can clearly see the trend that the vacancy tends to have greater occupancy at increasing system pressure. It is somewhat surprising that reducing the dopant diameter from 1/2 to 1/3 of the larger component does not increase the average number of dopants occupying the vacancy at low pressure (although it does increase the occupancy at P^*=10.0). These very small dopants are easily accommodated in the interstitial spaces, where they interact with 6 large particle neighbors without causing steric strain. A single S3 system dopant in the vacancy can only be near to ~3-4 large neighbors simultaneously, and the second or third dopants to occupy a single vacancy are not optimally positioned to interact both with the lattice and with each other (so adsorption to the vacancy is not cooperative). In contrast, the dopants in systems S2 and E2 can fit more easily into the vacancy than into interstitial sites, and successive occupying dopants will be in position to attract each other and the large particles simultaneously.

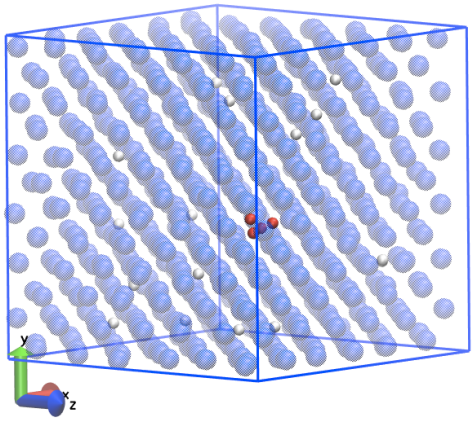

Fig. 7.5 A snapshot from our simulation for system S2 at pressure 10.0. Large species are shown in transparent blue, small species in interstices are shown in white, and particles in substitution position are shown red.

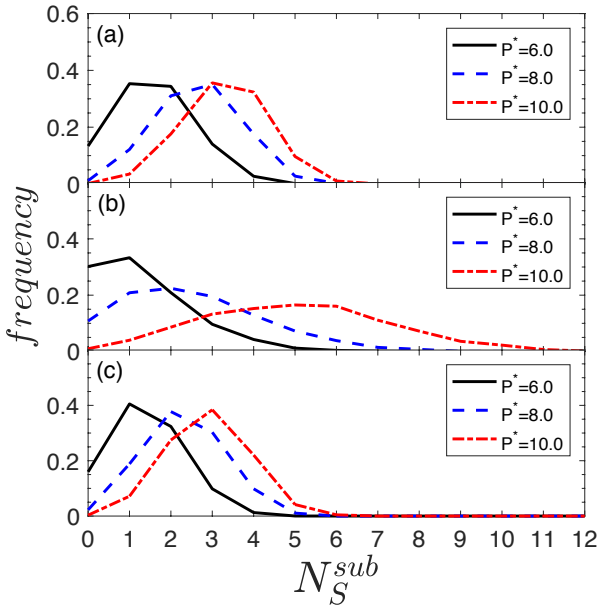

Fig. 7.6 Distribution of small species substitution in the defect site for system (a) S2, (b) S3 and (c) E2.

We sought then to determine the absolute levels of substitutional absorbates in these systems at coexistence. In principle, we could find vacancy concentrations in the doped solids directly from

GCMC, using large particle exchange moves at the fugacities f_L and f_S determined in section *3.1*. We found that conventional single-particle insertion and removal moves were more efficient for this purpose in these systems than the solvent-repacking Monte Carlo algorithm[8, 189], but that the overall levels of substitutional defects were too low to obtain good statistics during reasonable simulation times. Instead we used our knowledge of the equilibrium between empty vacancies and singly- or multiply-substituted vacancies under coexistence conditions, along with estimates of the un-substituted vacancy levels in the pure solid obtained by standard methods[186, 187]. Specifically, after defining a spherical subvolume v with a diameter of $1.06\sigma_{LL}$, which is centered at the empty lattice site in a crystal, trial insertion and removal are performed in this subvolume with acceptance probability $P_{add}(v)$ and $P_{rem}(v)$, respectively. The expression for free energy of vacancy formation is then

$$F = -k_B T ln(vP_{add}(v)/P_{rem}(v)\,\Lambda^d) \tag{7.3.2}$$

in which Λ is de Broglie wavelength and d is system dimension. The vacancy concentrations can thus be calculated from free energy F, and the vacancy concentrations for pure large species are listed in the first row of Table 7.3. These are very small and decrease exponentially with increasing pressure.

The possibility of substitution shifts the total equilibrium vacancy concentration (including vacancies occupied by one or more dopant) to higher values compared to the pure solid; a dopant residing in a vacancy will prevent it from being filled by a large particle[190]. The total vacancy concentration (including substituted vacancies) in the doped systems then is the concentration of unoccupied vacancies divided by the equilibrium fraction of vacancies that are unoccupied in the doped system, x_{empty} for a given dopant type and system pressure (Fig. 7.7). To check the reliability of this method, we compared its predictions with the results of direct GCMC simulation

incorporating large-particle insertion/removal moves for one test case (system S2 at pressure 6.0) and found an average vacancy concentration of 1.46×10^{-4}, in satisfactory agreement with the value of 1.75×10^{-4} found through the indirect method. The agreement suggests that the free energy of forming an unoccupied vacancy is the same, to a fair approximation, in the doped solids as is calculated for the pure solid.

The combined concentration of empty and substituted large-particle vacancies, shown in Table 7.3, stays approximately constant in all systems with increasing pressure. Keeping in mind that the values reflect the solid-liquid coexistence condition and that increasing pressure favors configurations of high packing efficiency, this result suggests that the space-filling efficiency of the small particles occupying the vacancy sites is similar to their packing efficiency in the coexisting liquid in systems.

The total concentration of substitutional dopants is then the product of the total combined vacancy concentration and the average vacancy occupation, which is shown in Fig. 7.8 along with the total concentration of interstitial dopants. Although the probability of occupation of interstitial sites is not as large as for vacancies, the much larger number of these sites makes interstitials the majority dopant type. At most, the fraction of dopants in substitutional sites reaches 1-2% of the interstitial dopant concentration; their levels are thus not significant for determination of the phase diagram, but could conceivably be detectable with an appropriate experiment.

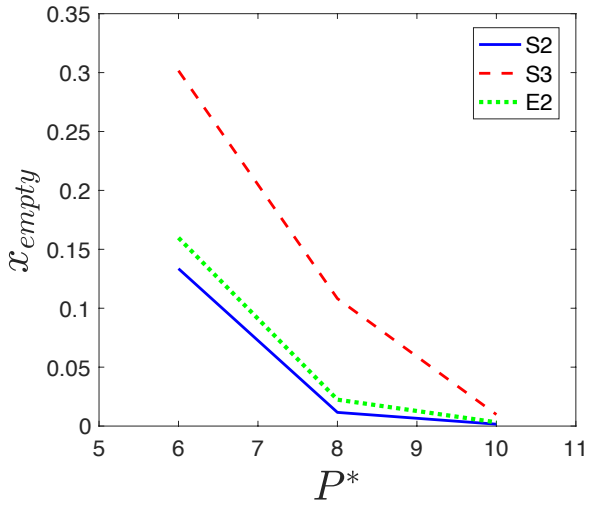

Fig. 7.7 Unoccupied vacancy fractions (x_{empty}) for different systems at different pressures.

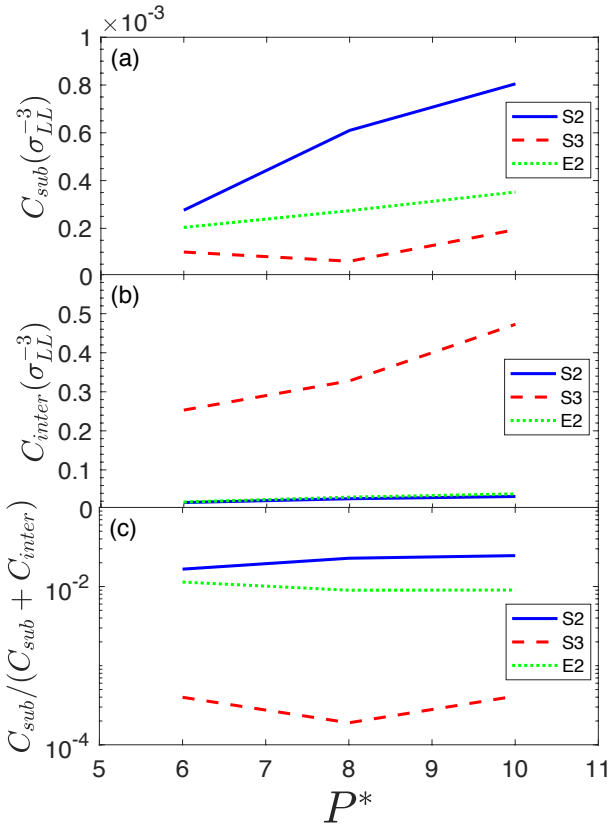

Fig. 7.8 (a) Concentration of substitutional particles at different pressures; (b) Concentration of interstitial particles at different pressures; (c) fraction of substitutional particles ($C_{sub}/(C_{sub}+C_{inter})$) at different pressures.

Table 7.3 Total of unoccupied, singly, and multiply substituted large particle vacancies in solid phase at liquid-solid coexistence for different mixtures and pressures. Levels for pure systems are calculated by free energy of vacancy formation. Mixtures (S2, S3 and E2) are calculated by the vacancy concentration in pure system divided by x_{empty}, as discussed in section *7.3.2*.

system	$C_{vacancy}\ (\sigma_{LL}^{-3})$		
	$P^* = 6.0$	$P^* = 8.0$	$P^* = 10.0$
Pure Large	2.34×10^{-5}	2.66×10^{-6}	3.78×10^{-7}
S2	1.75×10^{-4}	2.30×10^{-4}	2.36×10^{-4}
S3	7.76×10^{-5}	2.46×10^{-5}	3.86×10^{-5}
E2	1.46×10^{-4}	1.19×10^{-4}	1.18×10^{-4}

7.3.3 Dynamical and structural analysis of solutes in solid solution

We took some configurations of our GCMC simulations and run only the regular translation MC moves on these configurations for system S2 at different pressures to investigate the dynamics of small-particle diffusion. Small particles in interstice have some mobility (green trajectories in Fig. 7.9; particles migrate between neighboring interstitial sites, similar to the behavior found in hard sphere ISS system[83]. We also observed a decrease in this mobility upon increasing the pressure, which leads to a more compact octahedron and tetrahedron hole in interstice. These trajectories were initiated with 4 small particles in a substitutional site. Small particles occupying vacancies explore the volume vacated by the large particle as well as the six neighboring octahedral holes, creating a 4-pointed star when projected on the x-y plane (red trajectories in Fig. 7.9. Few transitions from the vacancy zone into neighboring octahedral holes were observed, all of which returned to the vacancy during the period of observation, and (like transitions between interstitial sites) all passing through the tetrahedral sites. In some cases (like Fig. 7.9(b)), the interstitial

particle enters into the vacancy and remains there. In additional tests (not shown) we have found that interstitial particles will enter a vacancy, or leave a vacancy that is occupied by an excessive number of particles, at comparable rates to the migration between interstitial sites. So, the vacancy site appears to act as a stable trap for small particles without a particularly high barrier to enter.

Fig. 7.10 shows a close look at the probability distribution of small species in the defect site of system S2 at P^*=10.0. The probability distribution for the small species confined by the vacancy has an octahedral shape, even when there is only one small particle present (Fig. 7.10(a)). However, when there are more particles presented (Fig. 7.10(b)), the density distribution splits into some high probability regions and low probability regions, which indicates some structure in the arrangements of multiple small species in the defect site. The distribution of angles in the 3-fold occupied system shows most of time they formed a triangle with a maximum angle smaller than 90° (Fig. 7.11). When moving up to the case that 4 particles occupying the vacancy, a highly symmetrical tetrahedral structure would be optimal in terms of attractions between the small particles. Therefore, the orientational tetrahedral order parameter q is employed to analyze the configurations[191, 192]:

$$q = 1 - \frac{3}{8}\sum_{j=1}^{3}\sum_{k=j+1}^{4}\left(cos\theta_{jk} + \frac{1}{3}\right)^2 \tag{7.3.3}$$

in which θ_{jk} is the angle formed by the lines joining the average position of four particles in consideration and the small particles j and k. For a regular tetrahedron, q will equal 1. Fig. 7.12 shows the major configuration is a tetrahedron as we predicted. Interestingly, there is also a second probable configuration (the second peak in Fig. 7.12(a)), associated with a planar structure Fig. 7.12(b) shows the distribution of distances between the particles in the tetramer and their center of mass, whose peak is slightly above the distance (0.343 σ_{LL}) for a perfect tetrahedron with edge lengths at the potential minimum of 1.12 σ_{SS}.

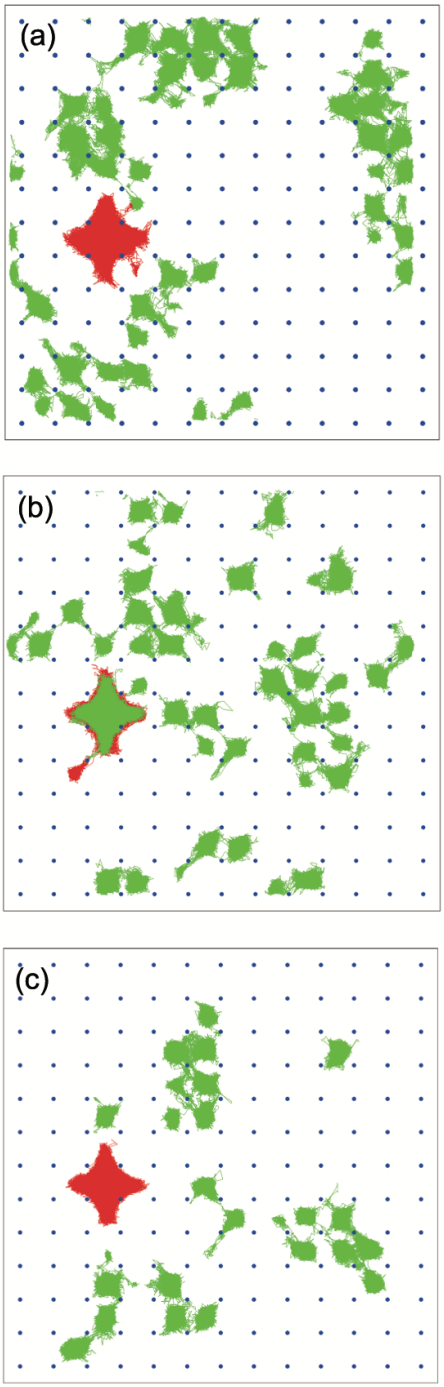

Fig. 7.9 The projection of a System S2 trajectory on x-y plane for small particles with initial position in vacancy (red) and interstice (green) at pressure (a) 6.0, (b) 8.0 and (c) 10.0; The blue lattice points denote the tetrahedral holes in solid.

A widely used order parameter Q_l developed by Steinhardt *et al.*[193] is employed to identify the cluster structure of 6-fold occupied system. Q_l is defined as:

$$Q_l = \left[\frac{4\pi}{2(l+1)}\sum_{m=-l}^{l}\left|\frac{1}{N}\sum_{j=1}^{N}Y_l^m(\theta_j,\phi_j)\right|^2\right]^{1/2} \quad (7.3.4)$$

where N is the number of lines joining the six particles in vacancy and their average position, $Y_l^m(\theta_j,\phi_j)$ is a spherical harmonic, and θ_j and ϕ_j are the angular coordinates of the jth particle with respect to some reference frame. Fig. 7.13 shows the Q_4 and Q_8 in our system deviates from the values in regular octahedron, although the Q_6 and Q_{10} fit the regular value quite well. We therefore cannot conclude the most probable structure in vacancy is octahedral. From visualization of the clusters in vacancy, we do see many distorted structures; only a few can be identified as the configuration close to the regular octahedron. We did not analyze the case more than 6-fold occupied system, due to the complexity of the cluster analysis when there are more particles, and the fact that it is a rare case to have an occupation larger than 6 for system S2 (Fig. 7.6(a)).

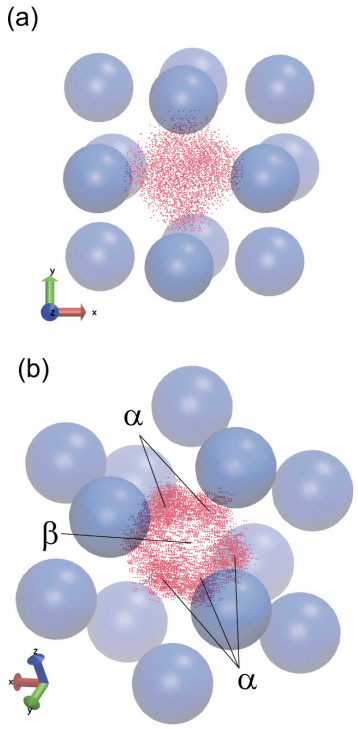

Fig. 7.10 Small species probability distribution plots (Red) in large species defect site for system S2 at P^*=10.0 (nearest 12 neighbors of large species are shown in transparent blue to indicate the defect site "cavity") are shown

with (a) only one particle in the defect site; (b) three particles present in the defect site. α indicates the high probability region small particles presented, while β indicates the low probability region.

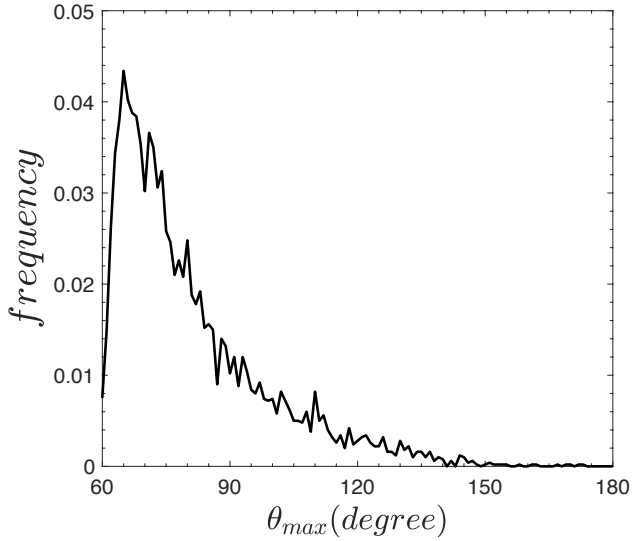

Fig. 7.11 The distribution of maximum angle θ_{max} in the triangle formed by the three small substitutional particles in vacancy for system S2 at P^*=10.0.

7.4 Conclusions

While interstitial and 1:1 substitution are well-studied modes of solution for small particles in the solid crystal formed by a larger particle type, we have quantified and characterized the degree of plural substitution in Lennard-Jones solid solutions at coexistence with fluid mixtures. The number of smaller solutes or dopants that occupy insterstitial sites was significantly greater than the number absorbed substitutionally for the three cases studied, with diameter ratios 1:2 or 1:3. Nonetheless, the phenomenon of plural substitution had a significant effect on the total number of large-particle lattice vacancies, keeping their level approximately constant as the pressure increased, in contrast to a lattice formed purely of large particles. Dynamical and structural analysis show similarities between the 1:3 LJ mixture and a similar hard-sphere interstitial solid solution, but that the Lennard-Jones particles tend toward multiple occupancy of interstitial sites as well.

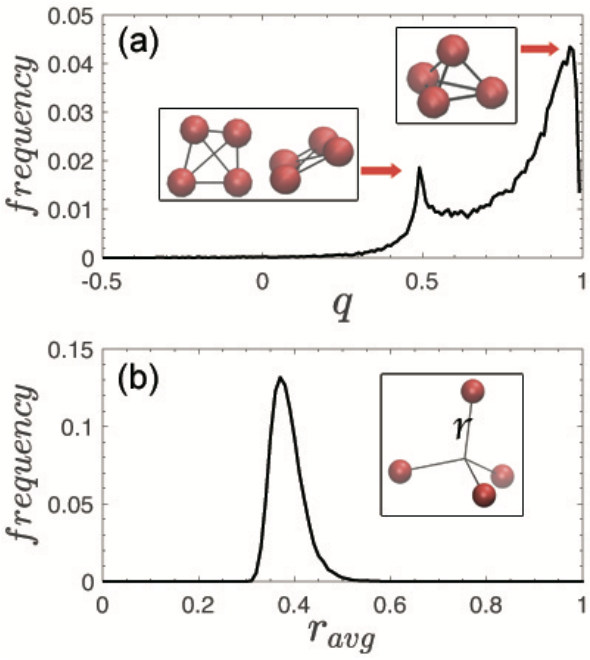

Fig. 7.12 Distribution of (a) orientational tetrahedral order parameter q, and (b) distance from particles to their average for four particles occupying vacancy in system S2 at P^*=10.0.

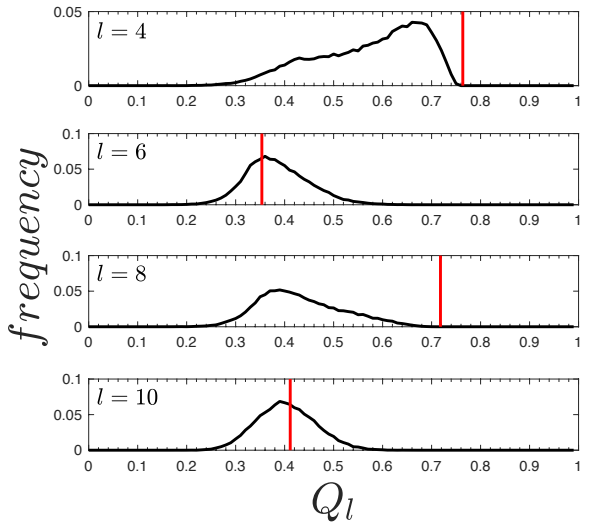

Fig. 7.13 Distribution of order parameter Q_l for six particles occupying vacancy in system S2 at P^*=10.0. Red vertical lines denote the Q_l for regular octahedron in corresponding l.

Conclusion

This dissertation describes the development of Solvent Repacking Monte Carlo (SRMC) and its applications on various systems including 2D Hard Sphere, quasi-2D Hard Sphere under gravity, and 3D Lennard-Jones particles. The SRMC and its variations are particular important for simulating the dense systems like particles in solid phase, or mixtures with size-asymmetrical impurity. Our ultimate goal is to develop a grand canonical method that can exchange a solute molecule with a number of solvent molecules. In studies not described here, we have tested the performance of our SRMC on explicit TIP3P water model and a united-atom acetonitrile model, which indicates the SRMC algorithm still needs to be improved in order to efficiently simulate the 3D system with soft potential for anisotropic molecules. One future direction is developed some other advanced algorithm to achieve the solvent repacking in 3D for soft potential molecules. This could be achieved by designing a new bias potential function, or developing other particle insertion strategy rather than the simple stepwise insertion.

Back to colloidal hard sphere system, there are still many explorations could be made through SRMC simulation. First, we can introduce another variable, curvature of surface, to discover the packing pattern/defect sites arrangement of hard sphere on a curved surface.[194] Also, in our study of colloidal hard sphere under gravity (*Chapter 5*),[195] the presence of overlayer yields many different behaviors compared to the single layer in 2D. Therefore, we can further explore the behaviors of multilayers by studying the hard sphere packing on a surface with curvature under gravity. The second direction is to study the grain boundary properties in 3D, where more complex structures/behaviors could be observed. With these current and future researches, we can gain more insights of the phase transition, grain boundary, impurity partitioning, which are very import either in fundamental chemical physics or material science.

References:

[1] D. Frenkel, and B. Smit, *Understanding Molecular Simulation: From Algorithms to Applications* (Elsevier, 2001), Vol. 1,
[2] J. I. Siepmann, and D. Frenkel, "Configurational Bias Monte Carlo: A New Sampling Scheme for Flexible Chains" Molecular Physics **75**, 59 (1992).
[3] V. Prasad, D. Semwogerere, and E. R. Weeks, "Confocal Microscopy of Colloids" Journal of Physics: Condensed Matter **19**, 113102 (2007).
[4] P. Schall, "Laser Diffraction Microscopy" Reports on Progress in Physics **72**, 076601 (2009).
[5] E. P. Bernard, and W. Krauth, "Two-Step Melting in Two Dimensions: First-Order Liquid-Hexatic Transition" Physical review letters **107**, 155704 (2011).
[6] M. Engel, J. A. Anderson, S. C. Glotzer, M. Isobe, E. P. Bernard, and W. Krauth, "Hard-Disk Equation of State: First-Order Liquid-Hexatic Transition in Two Dimensions with Three Simulation Methods" Physical Review E **87**, 042134 (2013).
[7] A. L. Thorneywork, J. L. Abbott, D. G. Aarts, and R. P. Dullens, "Two-Dimensional Melting of Colloidal Hard Spheres" Physical review letters **118**, 158001 (2017).
[8] J. T. Kindt, "Grand Canonical Monte Carlo Using Solvent Repacking: Application to Phase Behavior of Hard Disk Mixtures" The Journal of chemical physics **143**, 124109 (2015).
[9] J. Russo, and N. B. Wilding, "Disappearance of the Hexatic Phase in a Binary Mixture of Hard Disks" Physical review letters **119**, 115702 (2017).
[10] C. Herring, (McGraw-Hill Book Co., New York, 1951).
[11] J. Howe, (New York: Wiley, 1997).
[12] A. Rollett, F. Humphreys, G. S. Rohrer, and M. Hatherly, *Recrystallization and Related Annealing Phenomena* (Elsevier, 2004),
[13] M. A. Meyers, A. Mishra, and D. J. Benson, "Mechanical Properties of Nanocrystalline Materials" Progress in materials science **51**, 427 (2006).
[14] K. Kreuer, "Proton-Conducting Oxides" Annual Review of Materials Research **33**, 333 (2003).
[15] C. S. Ruiz-Vargas, H. L. Zhuang, P. Y. Huang, A. M. Van Der Zande, S. Garg, P. L. McEuen, D. A. Muller, R. G. Hennig, and J. Park, "Softened Elastic Response and Unzipping in Chemical Vapor Deposition Graphene Membranes" Nano letters **11**, 2259 (2011).
[16] H. Van Swygenhoven, "Grain Boundaries and Dislocations" Science **296**, 66 (2002).
[17] T. Zykova-Timan, R. E. Rozas, J. Horbach, and K. Binder, "Computer Simulation Studies of Finite-Size Broadening of Solid–Liquid Interfaces: From Hard Spheres to Nickel" Journal of Physics: Condensed Matter **21**, 464102 (2009).
[18] V. Randle, "Grain Boundary Engineering: An Overview after 25 Years" Materials science and technology **26**, 253 (2010).
[19] A. M. Van Der Zande, P. Y. Huang, D. A. Chenet, T. C. Berkelbach, Y. You, G.-H. Lee, T. F. Heinz, D. R. Reichman, D. A. Muller, and J. C. Hone, "Grains and Grain Boundaries in Highly Crystalline Monolayer Molybdenum Disulphide" Nature materials **12**, 554 (2013).
[20] H. Gleiter, "The Structure and Properties of High-Angle Grain Boundaries in Metals" Physica status solidi (b) **45**, 9 (1971).
[21] T. O. Skinner, D. G. Aarts, and R. P. Dullens, "Grain-Boundary Fluctuations in Two-Dimensional Colloidal Crystals" Physical review letters **105**, 168301 (2010).
[22] N. Eustathopoulos, "Energetics of Solid/Liquid Interfaces of Metals and Alloys" International metals reviews **28**, 189 (1983).

[23] Y. Huang, and F. Humphreys, "Measurements of Grain Boundary Mobility During Recrystallization of a Single-Phase Aluminium Alloy" Acta Materialia **47**, 2259 (1999).
[24] F. A. Lavergne, D. G. Aarts, and R. P. Dullens, "Anomalous Grain Growth in a Polycrystalline Monolayer of Colloidal Hard Spheres" Physical Review X **7**, 041064 (2017).
[25] M. Asta, C. Beckermann, A. Karma, W. Kurz, R. Napolitano, M. Plapp, G. Purdy, M. Rappaz, and R. Trivedi, "Solidification Microstructures and Solid-State Parallels: Recent Developments, Future Directions" Acta Materialia **57**, 941 (2009).
[26] S. M. Foiles, and J. Hoyt, "Computation of Grain Boundary Stiffness and Mobility from Boundary Fluctuations" Acta Materialia **54**, 3351 (2006).
[27] Z. T. Trautt, M. Upmanyu, and A. Karma, "Interface Mobility from Interface Random Walk" Science **314**, 632 (2006).
[28] J. Hoyt, Z. Trautt, and M. Upmanyu, "Fluctuations in Molecular Dynamics Simulations" Mathematics and Computers in Simulation **80**, 1382 (2010).
[29] Y. Jiang, and J. T. Kindt, "Simulations of Edge Behavior in a Mixed-Lipid Bilayer: Fluctuation Analysis" The Journal of chemical physics **126**, 01B624 (2007).
[30] S. Katira, K. K. Mandadapu, S. Vaikuntanathan, B. Smit, and D. Chandler, "Pre-Transition Effects Mediate Forces of Assembly between Transmembrane Proteins" Elife **5**, (2016).
[31] S. A. Safran, *Statistical Thermodynamics of Surfaces, Interfaces, and Membranes* (Perseus Books, 1994), Vol. 90,
[32] G. Gottstein, and L. S. Shvindlerman, *Grain Boundary Migration in Metals: Thermodynamics, Kinetics, Applications* (CRC press, 2009),
[33] A. P. Sutton, "Interfaces in Crystalline Materials" Monographs on the Physice and Chemistry of Materials, 414 (1995).
[34] A. J. Detor, and C. A. Schuh, "Grain Boundary Segregation, Chemical Ordering and Stability of Nanocrystalline Alloys: Atomistic Computer Simulations in the Ni–W System" Acta Materialia **55**, 4221 (2007).
[35] M. Seah, and E. Hondros, "Grain Boundary Segregation" Proc. R. Soc. Lond. A **335**, 191 (1973).
[36] M. Seah, "Grain Boundary Segregation" Journal of Physics F: Metal Physics **10**, 1043 (1980).
[37] E. Hondros, and M. Seah, "The Theory of Grain Boundary Segregation in Terms of Surface Adsorption Analogues" Metallurgical Transactions A **8**, 1363 (1977).
[38] P. Lejček, and S. Hofmann, "Thermodynamics and Structural Aspects of Grain Boundary Segregation" Critical Reviews in Solid State and Material Sciences **20**, 1 (1995).
[39] J. R. Trelewicz, and C. A. Schuh, "Grain Boundary Segregation and Thermodynamically Stable Binary Nanocrystalline Alloys" Physical Review B **79**, 094112 (2009).
[40] F. o. A. Lavergne, S. Diana, D. G. Aarts, and R. P. Dullens, "Equilibrium Grain Boundary Segregation and Clustering of Impurities in Colloidal Polycrystalline Monolayers" Langmuir **32**, 12716 (2016).
[41] F. J. Humphreys, and M. Hatherly, *Recrystallization and Related Annealing Phenomena* (Elsevier, 2012),
[42] J. W. Cahn, "The Impurity-Drag Effect in Grain Boundary Motion" Acta metallurgica **10**, 789 (1962).
[43] C. Zener, "Grains, Phases and Interfaces: An Interpretation of Microstructure" Trans. AIME **175**, 15 (1948).
[44] E. Nes, N. Ryum, and O. Hunderi, "On the Zener Drag" Acta Metallurgica **33**, 11 (1985).
[45] D. J. Srolovitz, and G. S. Grest, "Impurity Effects on Domain-Growth Kinetics. Ii. Potts Model" Physical Review B **32**, 3021 (1985).

[46] G. N. Hassold, E. A. Holm, and D. J. Srolovitz, "Effects of Particle Size on Inhibited Grain Growth" Scripta Metallurgica et Materialia **24**, 101 (1990).
[47] H. Hu, "Recovery and Recrystallization of Metals" Interscience **311**, (1963).
[48] K. Yoshizawa, T. Okuzono, T. Koga, T. Taniji, and J. Yamanaka, "Exclusion of Impurity Particles During Grain Growth in Charged Colloidal Crystals" Langmuir **27**, 13420 (2011).
[49] S. Gokhale, K. H. Nagamanasa, V. Santhosh, A. Sood, and R. Ganapathy, "Directional Grain Growth from Anisotropic Kinetic Roughening of Grain Boundaries in Sheared Colloidal Crystals" Proceedings of the National Academy of Sciences **109**, 20314 (2012).
[50] S. Ji, C.-C. Liu, W. Liao, A. L. Fenske, G. S. Craig, and P. F. Nealey, "Domain Orientation and Grain Coarsening in Cylinder-Forming Poly (Styrene-B-Methyl Methacrylate) Films" Macromolecules **44**, 4291 (2011).
[51] M. Cross, and H. Greenside, *Pattern Formation and Dynamics in Nonequilibrium Systems* (Cambridge University Press, 2009),
[52] E. A. Holm, and S. M. Foiles, "How Grain Growth Stops: A Mechanism for Grain-Growth Stagnation in Pure Materials" Science **328**, 1138 (2010).
[53] A. Adland, Y. Xu, and A. Karma, "Unified Theoretical Framework for Polycrystalline Pattern Evolution" Physical review letters **110**, 265504 (2013).
[54] F. A. Lavergne, A. Curran, D. G. Aarts, and R. P. Dullens, "Dislocation-Controlled Formation and Kinetics of Grain Boundary Loops in Two-Dimensional Crystals" Proceedings of the National Academy of Sciences, 201804352 (2018).
[55] Z. Trautt, and Y. Mishin, "Grain Boundary Migration and Grain Rotation Studied by Molecular Dynamics" Acta Materialia **60**, 2407 (2012).
[56] M. Upmanyu, D. J. Srolovitz, A. Lobkovsky, J. A. Warren, and W. Carter, "Simultaneous Grain Boundary Migration and Grain Rotation" Acta Materialia **54**, 1707 (2006).
[57] E. Sanz, and D. Marenduzzo, "Dynamic Monte Carlo Versus Brownian Dynamics: A Comparison for Self-Diffusion and Crystallization in Colloidal Fluids" The Journal of chemical physics **132**, 194102 (2010).
[58] B. Smit, "Phase Diagrams of Lennard-Jones Fluids" The Journal of Chemical Physics **96**, 8639 (1992).
[59] J. Nicolas, K. Gubbins, W. Streett, and D. Tildesley, "Equation of State for the Lennard-Jones Fluid" Molecular Physics **37**, 1429 (1979).
[60] J. S. Rowlinson, and F. Swinton, *Liquids and Liquid Mixtures: Butterworths Monographs in Chemistry* (Butterworth-Heinemann, 2013),
[61] V. Mazur, L. Boshkov, and V. Murakhovsky, "Global Phase Behaviour of Binary Mixtures of Lennard-Jones Molecules" Physics Letters A **104**, 415 (1984).
[62] J. K. Johnson, J. A. Zollweg, and K. E. Gubbins, "The Lennard-Jones Equation of State Revisited" Molecular Physics **78**, 591 (1993).
[63] A. M. Georgoulaki, D. P. Tassios, and A. Z. Panagiotopoulos, "Phase Equilibria of Binary Lennard-Jones Mixtures: Simulation and Van Der Waals L-Fluid Theory" Fluid Phase Equilibria **100**, 153 (1994).
[64] M. Mecke, A. Müller, J. Winkelmann, J. Vrabec, J. Fischer, R. Span, and W. Wagner, "An Accurate Van Der Waals-Type Equation of State for the Lennard-Jones Fluid" International journal of thermophysics **17**, 391 (1996).
[65] S.-T. Lin, M. Blanco, and W. A. Goddard III, "The Two-Phase Model for Calculating Thermodynamic Properties of Liquids from Molecular Dynamics: Validation for the Phase Diagram of Lennard-Jones Fluids" The Journal of chemical physics **119**, 11792 (2003).

[66] G. Pastore, R. Santin, S. Taraphder, and F. Colonna, (AIP, 2005).
[67] P. Stringari, and M. Campestrini, "Application of the Slv-Eos for Representing Phase Equilibria of Binary Lennard–Jones Mixtures Including Solid Phases" Fluid Phase Equilibria **358**, 68 (2013).
[68] J. J. Potoff, and A. Z. Panagiotopoulos, "Critical Point and Phase Behavior of the Pure Fluid and a Lennard-Jones Mixture" The Journal of chemical physics **109**, 10914 (1998).
[69] D. J. Ashton, and N. B. Wilding, "Grand Canonical Simulation of Phase Behaviour in Highly Size-Asymmetrical Binary Fluids" Molecular Physics **109**, 999 (2011).
[70] V. Kumar, and J. R. Errington, "Monte Carlo Simulation Strategies to Compute Interfacial and Bulk Properties of Binary Fluid Mixtures" The Journal of chemical physics **138**, 174112 (2013).
[71] D. Fincham, N. Quirke, and D. Tildesley, "Computer Simulation of Molecular Liquid Mixtures. I. A Diatomic Lennard-Jones Model Mixture for Co2/C2h6" The Journal of chemical physics **84**, 4535 (1986).
[72] M. H. Lamm, and C. K. Hall, "Molecular Simulation of Complete Phase Diagrams for Binary Mixtures" AIChE journal **47**, 1664 (2001).
[73] M. H. Lamm, and C. K. Hall, "Equilibria between Solid, Liquid, and Vapor Phases in Binary Lennard–Jones Mixtures" Fluid phase equilibria **194**, 197 (2002).
[74] H. Watanabe, N. Ito, and C.-K. Hu, "Phase Diagram and Universality of the Lennard-Jones Gas-Liquid System" The Journal of chemical physics **136**, 204102 (2012).
[75] A. L. Galbraith, and C. Hall, "Vapor–Liquid Phase Equilibria for Mixtures Containing Diatomic Lennard–Jones Molecules" Fluid phase equilibria **241**, 175 (2006).
[76] D. A. Kofke, "Gibbs-Duhem Integration: A New Method for Direct Evaluation of Phase Coexistence by Molecular Simulation" Molecular Physics **78**, 1331 (1993).
[77] Y. Tang, "A New Method of Semigrand Canonical Ensemble to Calculate First-Order Phase Transitions for Binary Mixtures" The Journal of chemical physics **136**, 034505 (2012).
[78] U. K. Deiters, and I. L. Pegg, "Systematic Investigation of the Phase Behavior in Binary Fluid Mixtures. I. Calculations Based on the Redlich–Kwong Equation of State" The Journal of Chemical Physics **90**, 6632 (1989).
[79] M. Barroso, and A. Ferreira, "Solid–Fluid Coexistence of the Lennard-Jones System from Absolute Free Energy Calculations" The Journal of chemical physics **116**, 7145 (2002).
[80] B. E. TRIZAC, M. E. MADDEN, and PA, "Stability of the Ab Crystal for Asymmetric Binary Hard Sphere Mixtures" Molecular Physics **90**, 675 (1997).
[81] N. Hunt, R. Jardine, and P. Bartlett, "Superlattice Formation in Mixtures of Hard-Sphere Colloids" Physical Review E **62**, 900 (2000).
[82] E. Vermolen, A. Kuijk, L. Filion, M. Hermes, J. Thijssen, M. Dijkstra, and A. Van Blaaderen, "Fabrication of Large Binary Colloidal Crystals with a Nacl Structure" Proceedings of the National Academy of Sciences **106**, 16063 (2009).
[83] L. Filion, M. Hermes, R. Ni, E. Vermolen, A. Kuijk, C. Christova, J. Stiefelhagen, T. Vissers, A. van Blaaderen, and M. Dijkstra, "Self-Assembly of a Colloidal Interstitial Solid with Tunable Sublattice Doping" Physical review letters **107**, 168302 (2011).
[84] J. D. Verhoeven, *Steel Metallurgy for the Non-Metallurgist* (ASM International, 2007),
[85] Z. Wang, C. Liu, and P. Dou, "Thermodynamics of Vacancies and Clusters in High-Entropy Alloys" Physical Review Materials **1**, 043601 (2017).
[86] N. Metropolis, A. W. Rosenbluth, M. N. Rosenbluth, A. H. Teller, and E. Teller, "Equation of State Calculations by Fast Computing Machines" The journal of chemical physics **21**, 1087 (1953).
[87] J. Harris, and S. A. Rice, "A Lattice Model of a Supported Monolayer of Amphiphile Molecules: Monte Carlo Simulations" The Journal of chemical physics **88**, 1298 (1988).

[88] D. Frenkel, G. Mooij, and B. Smit, "Novel Scheme to Study Structural and Thermal Properties of Continuously Deformable Molecules" Journal of Physics: Condensed Matter **4**, 3053 (1992).
[89] J. J. de Pablo, M. Laso, and U. W. Suter, "Simulation of Polyethylene above and Below the Melting Point" The Journal of chemical physics **96**, 2395 (1992).
[90] K. Kremer, and K. Binder, "Monte Carlo Simulation of Lattice Models for Macromolecules" Computer Physics Reports **7**, 259 (1988).
[91] M. N. Rosenbluth, and A. W. Rosenbluth, "Monte Carlo Calculation of the Average Extension of Molecular Chains" The Journal of Chemical Physics **23**, 356 (1955).
[92] A. Z. Panagiotopoulos, "Direct Determination of Phase Coexistence Properties of Fluids by Monte Carlo Simulation in a New Ensemble" Molecular Physics **61**, 813 (1987).
[93] D. J. Ashton, J. Liu, E. Luijten, and N. B. Wilding, "Monte Carlo Cluster Algorithm for Fluid Phase Transitions in Highly Size-Asymmetrical Binary Mixtures" The Journal of chemical physics **133**, 194102 (2010).
[94] J. Liu, and E. Luijten, "Rejection-Free Geometric Cluster Algorithm for Complex Fluids" Physical review letters **92**, 035504 (2004).
[95] J. Liu, and E. Luijten, "Generalized Geometric Cluster Algorithm for Fluid Simulation" Physical Review E **71**, 066701 (2005).
[96] S. Gokhale, K. H. Nagamanasa, R. Ganapathy, and A. Sood, "Grain Growth and Grain Boundary Dynamics in Colloidal Polycrystals" Soft Matter **9**, 6634 (2013).
[97] P. Dillmann, G. Maret, and P. Keim, "Polycrystalline Solidification in a Quenched 2d Colloidal System" Journal of Physics: Condensed Matter **20**, 404216 (2008).
[98] C. E. Cash, J. Wang, M. M. Martirossyan, B. K. Ludlow, A. E. Baptista, N. M. Brown, E. J. Weissler, J. Abacousnac, and S. J. Gerbode, "Local Melting Attracts Grain Boundaries in Colloidal Polycrystals" Physical Review Letters **120**, 018002 (2018).
[99] W. Qi, A. P. Gantapara, and M. Dijkstra, "Two-Stage Melting Induced by Dislocations and Grain Boundaries in Monolayers of Hard Spheres" Soft Matter **10**, 5449 (2014).
[100] D. R. Nelson, *Defects and Geometry in Condensed Matter Physics* (Cambridge University Press, 2002),
[101] D. G. Chae, F. H. Ree, and T. Ree, "Radial Distribution Functions and Equation of State of the Hard-Disk Fluid" The Journal of Chemical Physics **50**, 1581 (1969).
[102] J. Broughton, and G. Gilmer, "Thermodynamic Criteria for Grain-Boundary Melting: A Molecular-Dynamics Study" Physical review letters **56**, 2692 (1986).
[103] A. M. Alsayed, M. F. Islam, J. Zhang, P. J. Collings, and A. G. Yodh, "Premelting at Defects within Bulk Colloidal Crystals" Science **309**, 1207 (2005).
[104] P. Williams, and Y. Mishin, "Thermodynamics of Grain Boundary Premelting in Alloys. Ii. Atomistic Simulation" Acta Materialia **57**, 3786 (2009).
[105] S. Deutschländer, C. Boitard, G. Maret, and P. Keim, "Grain-Boundary-Induced Melting in Quenched Polycrystalline Monolayers" Physical Review E **92**, 060302 (2015).
[106] S. G. Kim, D. I. Kim, W. T. Kim, and Y. B. Park, "Computer Simulations of Two-Dimensional and Three-Dimensional Ideal Grain Growth" Physical Review E **74**, 061605 (2006).
[107] J. Gruber, H. Miller, T. Hoffmann, G. Rohrer, and A. Rollett, "Misorientation Texture Development During Grain Growth. Part I: Simulation and Experiment" Acta Materialia **57**, 6102 (2009).
[108] L. Zhang, J. Han, Y. Xiang, and D. J. Srolovitz, "Equation of Motion for a Grain Boundary" Physical review letters **119**, 246101 (2017).

[109] J. M. Howe, *Interfaces in Materials: Atomic Structure, Thermodynamics and Kinetics of Solid-Vapor, Solid-Liquid and Solid-Solid Interfaces* (Wiley-Interscience, 1997),
[110] V. W. de Villeneuve, L. Derendorp, D. Verboekend, E. C. Vermolen, W. K. Kegel, H. N. Lekkerkerker, and R. P. Dullens, "Grain Boundary Pinning in Doped Hard Sphere Crystals" Soft Matter **5**, 2448 (2009).
[111] N. Ghofraniha, E. Tamborini, J. Oberdisse, L. Cipelletti, and L. Ramos, "Grain Refinement and Partitioning of Impurities in the Grain Boundaries of a Colloidal Polycrystal" Soft Matter **8**, 6214 (2012).
[112] Z. Guo, and J. T. Kindt, "Simulations of Grain Boundaries between Ordered Hard Sphere Monolayer Domains: Orientation-Dependent Stiffness and Its Correlation with Grain Coarsening Dynamics" The Journal of Chemical Physics **149**, 044503 (2018).
[113] H. Gleiter, "The Structure and Properties of High-Angle Grain Boundaries in Metals" Physica Status Solidi (b) **45**, 9 (1971).
[114] W. T. Read, and W. Shockley, "Dislocation Models of Crystal Grain Boundaries" Physical Review **78**, 275 (1950).
[115] E. Cockayne, G. M. Rutter, N. P. Guisinger, J. N. Crain, P. N. First, and J. A. Stroscio, "Grain Boundary Loops in Graphene" Physical Review B **83**, 195425 (2011).
[116] J. W. Cahn, and J. E. Taylor, "A Unified Approach to Motion of Grain Boundaries, Relative Tangential Translation Along Grain Boundaries, and Grain Rotation" Acta Materialia **52**, 4887 (2004).
[117] B. Alder, and T. Wainwright, "Phase Transition in Elastic Disks" Phys. Rev. **127**, 359 (1962).
[118] E. P. Bernard, and W. Krauth, "Two-Step Melting in Two Dimensions: First-Order Liquid-Hexatic Transition" Phys. Rev. Lett. **107**, 155704 (2011).
[119] A. L. Thorneywork, J. L. Abbott, D. G. Aarts, and R. P. Dullens, "Two-Dimensional Melting of Colloidal Hard Spheres" Phys. Rev. Lett. **118**, 158001 (2017).
[120] N. Vogel, M. Retsch, C.-A. Fustin, A. del Campo, and U. Jonas, "Advances in Colloidal Assembly: The Design of Structure and Hierarchy in Two and Three Dimensions" Chem. Rev. **115**, 6265 (2015).
[121] J. Tang, P. J. Quinlan, and K. C. Tam, "Stimuli-Responsive Pickering Emulsions: Recent Advances and Potential Applications" Soft Matter **11**, 3512 (2015).
[122] J. Wu, and G. H. Ma, "Recent Studies of Pickering Emulsions: Particles Make the Difference" Small **12**, 4633 (2016).
[123] B. P. Binks, "Colloidal Particles at a Range of Fluid–Fluid Interfaces" Langmuir **33**, 6947 (2017).
[124] T. Biben, R. Ohnesorge, and H. Löwen, "Crystallization in Sedimentation Profiles of Hard Spheres" Europhys. Lett. **28**, 665 (1994).
[125] M. Marechal, M. Hermes, and M. Dijkstra, "Stacking in Sediments of Colloidal Hard Spheres" J. Chem. Phys. **135**, 034510 (2011).
[126] S. Dorosz, and T. Schilling, "On the Influence of a Patterned Substrate on Crystallization in Suspensions of Hard Spheres" J. Chem. Phys. **136**, 044702 (2012).
[127] J. Hilhorst, D. M. de Winter, J. R. Wolters, J. A. Post, and A. V. Petukhov, "Defect Engineering in Sedimentary Colloidal Photonic Crystals" Langmuir **29**, 10011 (2013).
[128] T. Palberg, "Crystallization Kinetics of Colloidal Model Suspensions: Recent Achievements and New Perspectives" J. Phys.: Cond. Matt. **26**, 333101 (2014).
[129] M. Marechal, and M. Dijkstra, "Crystallization of Colloidal Hard Spheres under Gravity" Phys. Rev. E **75**, 061404 (2007).

[130] J. Russo, A. C. Maggs, D. Bonn, and H. Tanaka, "The Interplay of Sedimentation and Crystallization in Hard-Sphere Suspensions" Soft Matter **9**, 7369 (2013).
[131] J. P. Hoogenboom, D. Derks, P. Vergeer, and A. van Blaaderen, "Stacking Faults in Colloidal Crystals Grown by Sedimentation" J. Chem. Phys. **117**, 11320 (2002).
[132] J. P. Hoogenboom, P. Vergeer, and A. van Blaaderen, "A Real-Space Analysis of Colloidal Crystallization in a Gravitational Field at a Flat Bottom Wall" J. Chem. Phys. **119**, 3371 (2003).
[133] P. Pieranski, L. Strzelecki, and B. Pansu, "Thin Colloidal Crystals" Phys. Rev. Lett. **50**, 900 (1983).
[134] A. Fortini, and M. Dijkstra, "Phase Behaviour of Hard Spheres Confined between Parallel Hard Plates: Manipulation of Colloidal Crystal Structures by Confinement" J. Phys.: Cond. Matt. **18**, L371 (2006).
[135] W. Qi, Y. Peng, Y. Han, R. K. Bowles, and M. Dijkstra, "Nonclassical Nucleation in a Solid-Solid Transition of Confined Hard Spheres" Phys. Rev. Lett. **115**, 185701 (2015).
[136] A. Sonn-Segev, J. Bławzdziewicz, E. Wajnryb, M. L. Ekiel-Jeżewska, H. Diamant, and Y. Roichman, "Structure and Dynamics of a Layer of Sedimented Particles" J. Chem. Phys. **143**, 074704 (2015).
[137] H. Choi, J. Talbot, G. Tarjus, and P. Viot, "First-Layer Formation in Ballistic Deposition of Spherical Particles: Kinetics and Structure" J. Chem. Phys. **99**, 9296 (1993).
[138] I. B. Ramsteiner, K. E. Jensen, D. A. Weitz, and F. Spaepen, "Experimental Observation of the Crystallization of Hard-Sphere Colloidal Particles by Sedimentation onto Flat and Patterned Surfaces" Phys. Rev. E **79**, 011403 (2009).
[139] J. T. Kindt, "Grand Canonical Monte Carlo Using Solvent Repacking: Application to Phase Behavior of Hard Disk Mixtures" J. Chem. Phys. **143**, 124109 (2015).
[140] M. Schmidt, and H. Löwen, "Phase Diagram of Hard Spheres Confined between Two Parallel Plates" Phys. Rev. E **55**, 7228 (1997).
[141] F. Ana Barreira, S. Hans Joachim, K. Hans, P. Thomas, M. René, and L. Hartmut, "A Comparative Study on the Phase Behaviour of Highly Charged Colloidal Spheres in a Confining Wedge Geometry" J. Phys.: Cond. Matt. **17**, S2779 (2005).
[142] S. Neser, C. Bechinger, P. Leiderer, and T. Palberg, "Finite-Size Effects on the Closest Packing of Hard Spheres" Phys. Rev. Lett. **79**, 2348 (1997).
[143] T. Curk, A. de Hoogh, F. J. Martinez-Veracoechea, E. Eiser, D. Frenkel, J. Dobnikar, and M. E. Leunissen, "Layering, Freezing, and Re-Entrant Melting of Hard Spheres in Soft Confinement" Phys. Rev. E **85**, 021502 (2012).
[144] Z. Guo, and J. T. Kindt, "Simulations of Grain Boundaries between Ordered Hard Sphere Monolayer Domains: Orientation-Dependent Stiffness and Its Correlation with Grain Coarsening Dynamics" J. Chem. Phys. **149**, 044503 (2018).
[145] J. I. Siepmann, and D. Frenkel, "Configurational Bias Monte Carlo: A New Sampling Scheme for Flexible Chains" Mol. Phys. **75**, 59 (1992).
[146] Z. Guo, and J. T. Kindt, "Partitioning of Size-Mismatched Impurities to Grain Boundaries in 2d Solid Hard-Sphere Monolayers" Langmuir **in press**, (2018).
[147] W. Humphrey, A. Dalke, and K. Schulten, "Vmd - Visual Molecular Dynamics" J. Mol. Graph. **14**, 33 (1996).
[148] V. Prasad, D. Semwogerere, and E. R. Weeks, "Confocal Microscopy of Colloids" J. Phys.: Cond. Matt. **19**, 113102 (2007).
[149] T. Franosch, S. Lang, and R. Schilling, "Fluids in Extreme Confinement" Phys. Rev. Lett. **109**, 240601 (2012).

[150] W. G. Hoover, and F. H. Ree, "Melting Transition and Communal Entropy for Hard Spheres" J. Chem. Phys. **49**, 3609 (1968).
[151] A. Z. Patashinski, R. Orlik, A. C. Mitus, M. A. Ratner, and B. A. Grzybowski, "Microphase Separation as the Cause of Structural Complexity in 2d Liquids" Soft Matter **9**, 10042 (2013).
[152] F. A. Lavergne, D. G. A. L. Aarts, and R. P. A. Dullens, "Anomalous Grain Growth in a Polycrystalline Monolayer of Colloidal Hard Spheres" Phys. Rev. X **7**, 041064 (2017).
[153] M. Dijkstra, "Capillary Freezing or Complete Wetting of Hard Spheres in a Planar Hard Slit?" Phys. Rev. Lett. **93**, 108303 (2004).
[154] B. B. Laird, and R. L. Davidchack, "Wall-Induced Prefreezing in Hard Spheres: A Thermodynamic Perspective" Journal of Physical Chemistry C **111**, 15952 (2007).
[155] V. Martelozzo, A. Schofield, W. Poon, and P. Pusey, "Structural Aging of Crystals of Hard-Sphere Colloids" Phys. Rev. E **66**, 021408 (2002).
[156] M. P. Howard, W. F. Reinhart, T. Sanyal, M. S. Shell, A. Nikoubashman, and A. Z. Panagiotopoulos, "Evaporation-Induced Assembly of Colloidal Crystals" J. Chem. Phys. **149**, 094901 (2018).
[157] S. Pronk, and D. Frenkel, "Melting of Polydisperse Hard Disks" Phys. Rev. E **69**, 066123 (2004).
[158] N. B. Wilding, and P. Sollich, "Grand Canonical Ensemble Simulation Studies of Polydisperse Fluids" J. Chem. Phys. **116**, 7116 (2002).
[159] A. Panagiotopoulos, "Exact Calculations of Fluid-Phase Equilibria by Monte Carlo Simulation in a New Statistical Ensemble" International Journal of Thermophysics **10**, 447 (1989).
[160] B. Chen, J. I. Siepmann, and M. L. Klein, "Direct Gibbs Ensemble Monte Carlo Simulations for Solid− Vapor Phase Equilibria: Applications to Lennard− Jonesium and Carbon Dioxide" The Journal of Physical Chemistry B **105**, 9840 (2001).
[161] P. Bai, and J. I. Siepmann, "Assessment and Optimization of Configurational-Bias Monte Carlo Particle Swap Strategies for Simulations of Water in the Gibbs Ensemble" Journal of chemical theory and computation **13**, 431 (2017).
[162] J. Liu, N. B. Wilding, and E. Luijten, "Simulation of Phase Transitions in Highly Asymmetric Fluid Mixtures" Physical review letters **97**, 115705 (2006).
[163] T. Biben, P. Bladon, and D. Frenkel, "Depletion Effects in Binary Hard-Sphere Fluids" Journal of Physics: Condensed Matter **8**, 10799 (1996).
[164] P. Bolhuis, and D. Frenkel, "Numerical Study of the Phase Diagram of a Mixture of Spherical and Rodlike Colloids" The Journal of chemical physics **101**, 9869 (1994).
[165] C. Wijmans, B. Smit, and R. Groot, "Phase Behavior of Monomeric Mixtures and Polymer Solutions with Soft Interaction Potentials" The Journal of Chemical Physics **114**, 7644 (2001).
[166] M. P. Allen, and D. J. Tildesley, *Computer Simulation of Liquids* (Oxford university press, 2017),
[167] A. Schofield, P. Pusey, and P. Radcliffe, "Stability of the Binary Colloidal Crystals a B 2 and a B 13" Physical Review E **72**, 031407 (2005).
[168] A. Paxton, and C. Elsässer, "Analysis of a Carbon Dimer Bound to a Vacancy in Iron Using Density Functional Theory and a Tight Binding Model" Physical Review B **87**, 224110 (2013).
[169] J. R. Fernández, and P. Harrowell, "Crystal Phases of a Glass-Forming Lennard-Jones Mixture" Physical Review E **67**, 011403 (2003).
[170] T. F. Middleton, J. Hernández-Rojas, P. N. Mortenson, and D. J. Wales, "Crystals of Binary Lennard-Jones Solids" Physical Review B **64**, 184201 (2001).

[171] A. A. Gusev, and S. A. Lurie, "Strain-Gradient Elasticity for Bridging Continuum and Atomistic Estimates of Stiffness of Binary Lennard-Jones Crystals" Advanced Engineering Materials **12**, 529 (2010).
[172] C. L. Phillips, and P. S. Crozier, "An Energy-Conserving Two-Temperature Model of Radiation Damage in Single-Component and Binary Lennard-Jones Crystals" The Journal of chemical physics **131**, 074701 (2009).
[173] S. Jungblut, and C. Dellago, "Crystallization of a Binary Lennard-Jones Mixture" The Journal of chemical physics **134**, 104501 (2011).
[174] J. R. Fernández, and P. Harrowell, "Ordered Binary Crystal Phases of Lennard-Jones Mixtures" The Journal of chemical physics **120**, 9222 (2004).
[175] M. J. Vlot, H. E. Huitema, A. de Vooys, and J. P. van der Eerden, "Crystal Structures of Symmetric Lennard-Jones Mixtures" The Journal of chemical physics **107**, 4345 (1997).
[176] S. J. Cook, and P. Clancy, "Impurity Segregation in Lennard-Jones a/Ab Heterostructures. I. The Effect of Lattice Strain" The Journal of chemical physics **99**, 2175 (1993).
[177] S. J. Cook, and P. Clancy, "Impurity Segregation in Lennard-Jones a/Ab Heterostructures. Ii. The Effect of Impurity Size" The Journal of chemical physics **99**, 2192 (1993).
[178] M. Sweatman, and N. Quirke, "Simulating Fluid–Solid Equilibrium with the Gibbs Ensemble" Molecular Simulation **30**, 23 (2004).
[179] R. Shetty, and F. A. Escobedo, "On the Application of Virtual Gibbs Ensembles to the Direct Simulation of Fluid–Fluid and Solid–Fluid Phase Coexistence" The Journal of chemical physics **116**, 7957 (2002).
[180] J. R. Errington, "Solid–Liquid Phase Coexistence of the Lennard-Jones System through Phase-Switch Monte Carlo Simulation" The Journal of chemical physics **120**, 3130 (2004).
[181] X. Cottin, and P. Monson, "Solid–Fluid Phase Equilibrium for Single Component and Binary Lennard-Jones Systems: A Cell Theory Approach" The Journal of chemical physics **105**, 10022 (1996).
[182] M. Radu, and K. Kremer, "Enhanced Crystal Growth in Binary Lennard-Jones Mixtures" Physical Review Letters **118**, 055702 (2017).
[183] D. A. Kofke, "Direct Evaluation of Phase Coexistence by Molecular Simulation Via Integration Along the Saturation Line" The Journal of chemical physics **98**, 4149 (1993).
[184] M. R. Hitchcock, and C. K. Hall, "Solid–Liquid Phase Equilibrium for Binary Lennard-Jones Mixtures" The Journal of chemical physics **110**, 11433 (1999).
[185] A. Sherwood, and J. Prausnitz, "Intermolecular Potential Functions and the Second and Third Virial Coefficients" The Journal of Chemical Physics **41**, 429 (1964).
[186] C. Bennett, and B. Alder, "Studies in Molecular Dynamics. Ix. Vacancies in Hard Sphere Crystals" The Journal of Chemical Physics **54**, 4796 (1971).
[187] R. K. Bowles, and R. J. Speedy, "Cavities in the Hard Sphere Crystal and Fluid" Molecular Physics **83**, 113 (1994).
[188] W. Humphrey, A. Dalke, and K. Schulten, "Vmd: Visual Molecular Dynamics" Journal of molecular graphics **14**, 33 (1996).
[189] Z. Guo, and J. T. Kindt, "Gibbs Ensemble Monte Carlo with Solvent Repacking: Phase Coexistence of Size–Asymmetrical Binary Lennard-Jones Mixtures" Molecular Simulation, 1 (2017).
[190] T. Schuler, C. Barouh, M. Nastar, and C.-C. Fu, "Equilibrium Vacancy Concentration Driven by Undetectable Impurities" Physical review letters **115**, 015501 (2015).

[191] P.-L. Chau, and A. Hardwick, "A New Order Parameter for Tetrahedral Configurations" Molecular Physics **93**, 511 (1998).
[192] E. Duboué-Dijon, and D. Laage, "Characterization of the Local Structure in Liquid Water by Various Order Parameters" The Journal of Physical Chemistry B **119**, 8406 (2015).
[193] P. J. Steinhardt, D. R. Nelson, and M. Ronchetti, "Bond-Orientational Order in Liquids and Glasses" Physical Review B **28**, 784 (1983).
[194] R. E. Guerra, C. P. Kelleher, A. D. Hollingsworth, and P. M. Chaikin, "Freezing on a Sphere" Nature **554**, 346 (2018).
[195] Z. Guo, P. Wu, and J. T. Kindt, "Ordering of Colloidal Hard Spheres under Gravity: From Monolayer to Multilayer" Soft matter **15**, 1027 (2019).